

THE HALO NUCLEI  $^{11}\text{Be}$  AND  $^8\text{B}$  STUDIED BY  
FRAGMENTATION REACTIONS

by

JOHN HENRY KELLEY

A DISSERTATION

Submitted to  
Michigan State University  
in partial fulfillment of the requirements  
for the Degree of

DOCTOR OF PHILOSOPHY

Department of Physics and Astronomy

1995



## ABSTRACT

### THE HALO NUCLEI $^{11}\text{Be}$ AND $^8\text{B}$ STUDIED BY FRAGMENTATION REACTIONS

By

John Henry Kelley

The discovery of anomalously large matter radii in some weakly bound nuclei on the neutron dripline has led to measurements of breakup fragment momentum distributions aimed at obtaining a qualitative understanding of these nuclei. The valence nucleons in halo nuclei penetrate the low barrier of the core potential, and form a diffuse layer around a normal sized core. Momentum distributions of core fragments following a direct breakup are related to the spatial distribution of the halo nucleon, via Fourier Transform, and offer a straightforward method to study halo nuclei. The momentum distribution in the direction parallel with the beam direction ( $p_{\parallel}$ ) is less affected by reaction mechanism effects than the distribution perpendicular to the beam direction ( $p_{\perp}$ ), and is expected to most accurately reflect the halo neutron momentum wavefunction.

The nucleus,  $^{11}\text{Be}$ , has a one-neutron halo and core fragment momentum distributions should permit a simple determination of halo characteristics. We measured the  $p_{\parallel}$  distribution of  $^{10}\text{Be}$  core fragments in Be, Nb, Ta and U targets and found that the  $p_{\parallel}$  distributions on all targets are in excellent agreement with a projection (onto the  $p_{\parallel}$  axis) of the momentum wavefunction of a  $2s_{1/2}$  neutron bound by 500 keV in a Woods-Saxon potential. This is taken to indicate that reaction mechanism effects do

not significantly influence the  $^{10}\text{Be}$  core fragment  $p_{\parallel}$  distributions. The corresponding root-mean-square radius of the halo neutron is 6.5 fm.

Finally, there is a controversy concerning the existence of a proton halo in  $^8\text{B}$ . We approached the issue assuming that the  $p_{\parallel}$  distributions of  $^7\text{Be}$  breakup fragments would reflect the spatial distribution of the valence proton, as we had shown for  $^{11}\text{Be}$ . Both  $p_{\parallel}$  and  $p_{\perp}$  were measured. The  $p_{\parallel}$  distributions are narrow, but are only about half of the width of a prediction for a proton bound by 140 keV in a Woods-Saxon potential with a rms radius of 4.24 fm. In this case, it appears that for the smaller halo of the p-orbital proton the breakup momenta are influenced by both the nuclear and Coulomb reaction mechanism effects. When these effects are included, the predictions agree with the data.

To mom and dad

## ACKNOWLEDGEMENTS

I must begin by thanking Sam Austin for his guidance during the past few years. He has encouraged me to develop my skills as a researcher at all levels, including writing proposals, planning experiments, data analysis, and peer reviewed publication.

I am also grateful to Michael Thoennessen, Alex Brown, Horace Smith, and Subendra Mahanti for their participation on my guidance committee.

During my stay at the NSCL I have had the opportunity to work with a number of collaborators to whom I must express my gratitude. Thank you John Winfield, Nigel Orr, Dave Morrissey, Brad Sherrill, Walter Benenson, Daniel Bazin, Jeff Winger, Toshiyuki Kubo, Bob Warner, Dave Mercer, Stephan Hirzebruch, Tiina Suomijarvi, Bob Kryger, Maggie Hellstrom, and Jim Brown. I have also had the privilege of working closely with Easwar Ramakrishnan, Brian Young, Raman Pfaff, Mathias Steiner, Michael Fauerbach, Shigeru Yokoyama, Afshin Azhari, Thomas Bauman, Ken Lamkin, and many others.

On a more personal note, thank you Easwar for putting up with me; thank you Mike for having an open door (and a clean window); thank you Dave for showing up in the Data-U at 7:30 AM on most mornings; and thank you Tiina for a chance to continue my research career.

# Contents

<b>LIST OF TABLES</b>	<b>ix</b>
<b>LIST OF FIGURES</b>	<b>xi</b>
<b>1 Introduction</b>	<b>1</b>
<b>2 Projectile-like Fragment Momentum Distributions</b>	<b>7</b>
2.1 Momentum Distributions . . . . .	7
2.2 Fragment Transverse Momentum Distributions from $^{11}\text{Li}$ Breakup . .	8
2.2.1 $^9\text{Li}$ Core $P_{\perp}$ Distributions . . . . .	8
2.2.2 Neutron Angular Distributions . . . . .	10
2.3 Breakup Reaction Mechanisms . . . . .	10
2.3.1 Stripping . . . . .	12
2.3.2 Diffraction Dissociation . . . . .	12
2.3.3 Coulomb Dissociation . . . . .	14
2.3.4 Reaction Mechanism Effects on Momentum Distributions . . .	15
2.4 The $P_{\parallel}$ Distribution of $^9\text{Li}$ Fragments from $^{11}\text{Li}$ Breakup . . . . .	16
2.4.1 Problems with the $^9\text{Li}$ $P_{\parallel}$ Distributions . . . . .	17
2.5 Need to Study a Simpler System . . . . .	18
<b>3 The Neutron Halo of <math>^{11}\text{Be}</math></b>	<b>21</b>
3.1 The $P_{\parallel}$ Distribution of $^{10}\text{Be}$ Fragments from $^{11}\text{Be}$ breakup . . . . .	22
3.1.1 The A1200 Fragment Separator . . . . .	23
3.1.2 Analysis of $^{10}\text{Be}$ Fragment Momentum Distributions . . . . .	29
3.1.3 Discussion of the $^{10}\text{Be}$ $P_{\parallel}$ Distributions . . . . .	38
3.2 Comparison with the Transverse Momentum Distributions of Fragments from $^{11}\text{Be}$ Breakup . . . . .	46
3.2.1 $P_{\perp}$ Distribution of Core Fragments . . . . .	46
3.2.2 Angular Distribution of Neutrons . . . . .	47

3.3	Neutron Halo Radius . . . . .	49
<b>4</b>	<b>Search for a Proton Halo in <math>^8\text{B}</math></b>	<b>51</b>
4.1	Experimental Measurements of the Nuclear Size of $^8\text{B}$ . . . . .	51
4.2	The $P_{\parallel}$ and $P_{\perp}$ Momentum Distributions of $^7\text{Be}$ Fragments Following the Breakup of $^8\text{B}$ . . . . .	54
4.2.1	Experimental Details . . . . .	55
4.3	Analysis of the Data . . . . .	57
4.3.1	The $P_x$ Distributions . . . . .	59
4.3.2	The $P_{\parallel}$ Distributions . . . . .	61
4.4	Results . . . . .	63
4.4.1	The $P_{\parallel}$ Distribution from Nuclear Breakup Processes . . . . .	64
4.4.2	The $P_{\parallel}$ Distribution From Coulomb Breakup Processes . . . . .	66
4.4.3	Angular Dependence of the Width of the $P_{\parallel}$ Distribution . . . . .	68
4.5	Valence Proton Radius . . . . .	69
<b>5</b>	<b>Summary and Outlook</b>	<b>71</b>
<b>A</b>	<b>Theoretical Discussion of Halo Nuclei</b>	<b>75</b>
A.1	Importance of the Binding Energy . . . . .	75
A.2	Importance of the Coulomb Potential Barrier . . . . .	77
<b>B</b>	<b>Experimental Evidence for Halo Nuclei</b>	<b>79</b>
B.1	Enhanced E1 Transition Strength . . . . .	79
B.2	Measurements of Reaction Cross Sections . . . . .	79
B.3	Energy Dependence of the $^{11}\text{Be}$ Reaction Cross Section . . . . .	81
B.4	Large Electromagnetic Dissociation Cross Section . . . . .	83
B.5	The $^{11}\text{Li}$ Dipole Excitation Strength Function . . . . .	84
B.6	The $^{11}\text{Be}$ Dipole Excitation Strength Function . . . . .	86
<b>C</b>	<b>Models for Fragment Momentum Distributions</b>	<b>89</b>
C.1	The Goldhaber Model . . . . .	89
C.2	The Serber Model . . . . .	90
C.3	The Friedman Model . . . . .	90
C.4	The Extended Serber Model . . . . .	91
<b>D</b>	<b>Coulomb Dissociation</b>	<b>93</b>

<b>E</b>	<b>The Influence of a Limited Acceptance on <math>P_{\parallel}</math> Distributions</b>	<b>95</b>
E.1	Nature of the Problem . . . . .	95
E.2	Results . . . . .	97
E.2.1	Lorentzian Distribution . . . . .	98
E.2.2	Dependence of Width on Angle . . . . .	99
E.2.3	Complex Momentum Distributions . . . . .	101
E.3	Summary . . . . .	106
<b>F</b>	<b>Coulomb Reacceleration on a Heavy Target</b>	<b>107</b>
F.1	Coulomb Reacceleration in $^{11}\text{Li}$ Breakup Fragments . . . . .	107
<b>G</b>	<b>Data Tables for <math>^{10}\text{Be}</math> Fragment Momentum Distributions</b>	<b>109</b>
<b>H</b>	<b>Data Tables for <math>^7\text{Be}</math> Fragment Momentum Distributions</b>	<b>115</b>
	<b>LIST OF REFERENCES</b>	<b>125</b>



# List of Tables

1.1	The rms radius of valence nucleons compared with their binding energy	4
3.1	The nuclei that comprised the RNB in the $^{11}\text{Be}$ breakup experiment.	25
3.2	Target thicknesses and momentum resolutions measured for targets in the $^{11}\text{Be}$ experiment . . . . .	37
3.3	Widths of parallel momentum distributions of $^{10}\text{Be}$ fragments following the breakup of $^{11}\text{Be}$ on various targets . . . . .	38
3.4	The expected mean momentum and widths of $^{10}\text{Be}$ fragment momentum distributions from fragmentation of contaminant nuclei in the RNB	40
4.1	Description of detectors that comprise the two telescopes in the $^8\text{B}$ breakup experiment. . . . .	56
4.2	Target thicknesses in the $^8\text{B}$ breakup experiment. . . . .	57
4.3	Widths of the $p_x$ distributions of $^7\text{Be}$ fragments following the breakup of $^8\text{B}$ . . . . .	61
4.4	Widths of the $p_{\parallel}$ distributions of $^7\text{Be}$ fragments following the breakup of $^8\text{B}$ . . . . .	63
E.1	Widths of the $p_{\parallel}$ distribution from a Lorentzian momentum distribution that passes through various aperture sizes . . . . .	99
G.1	The data for the $^{10}\text{Be}$ fragment $p_{\parallel}$ distribution on the Be target. . . .	112
G.2	The data for the $^{10}\text{Be}$ fragment $p_{\parallel}$ distribution on the Nb target. . . .	113
G.3	The data for the $^{10}\text{Be}$ fragment $p_{\parallel}$ distribution on the Ta target. . . .	114
G.4	The data for the $^{10}\text{Be}$ fragment $p_{\parallel}$ distribution on the U target. . . .	116
H.1	The data for the $^7\text{Be}$ fragment momentum distribution on the Be target measured in Telescope 1. . . . .	118
H.2	The data for the $^7\text{Be}$ fragment momentum distribution on the Be target measured in Telescope 2. . . . .	119

H.3	The data for the ${}^7\text{Be}$ $p_x$ fragment momentum distribution on the Be target. . . . .	120
H.4	The data for the ${}^7\text{Be}$ fragment momentum distribution on the Nb target measured in Telescope 1. . . . .	121
H.5	The data for the ${}^7\text{Be}$ fragment momentum distribution on the Nb target measured in Telescope 2. . . . .	122
H.6	The data for the ${}^7\text{Be}$ $p_x$ fragment momentum distribution on the Nb target. . . . .	123
H.7	The data for the ${}^7\text{Be}$ fragment momentum distribution on the Au target measured in Telescope 1. . . . .	124
H.8	The data for the ${}^7\text{Be}$ fragment momentum distribution on the Au target measured in Telescope 2. . . . .	125
H.9	The data for the ${}^7\text{Be}$ $p_x$ fragment momentum distribution on the Au target. . . . .	126

# List of Figures

1.1	The rms radii of light neutron rich isotopes . . . . .	2
1.2	A Woods-Saxon calculation of the proton and neutron density distributions in $^{11}\text{Li}$ . . . . .	3
2.1	The transverse momentum distribution of core fragments following the breakup of $^8\text{He}$ and $^{11}\text{Li}$ . . . . .	9
2.2	The angular distribution of neutrons following the breakup of $^{11}\text{Li}$ . . .	11
2.3	Schematic illustrating the Coulomb excitation process . . . . .	13
2.4	The $p_{\parallel}$ distribution of $^9\text{Li}$ fragments following the breakup of $^{11}\text{Li}$ . .	16
2.5	The $p_{\parallel}$ distribution widths of $^9\text{Li}$ fragments from $^{11}\text{Li}$ breakup . . . .	17
3.1	The nucleus $^{11}\text{Be}$ is comprised of a normal sized $^{10}\text{Be}$ core (2.30 fm) immersed in a neutron halo that has a rms radius of 6.5 fm. . . . .	21
3.2	The A1200 fragment separator and beam analysing device . . . . .	23
3.3	$\Delta E$ vs. ToF identifying $^{11}\text{Be}$ nuclei . . . . .	24
3.4	The principle of a dispersion matched energy loss spectrometer . . . .	27
3.5	Reaction products that reach the focal plane of the A1200 when the Be target is inserted at the Image 2 target position . . . . .	30
3.6	Conditions that are applied to the position histograms . . . . .	31
3.7	Condition that is applied to the total energy vs. ToF histogram . . .	32
3.8	The condition that is applied to the Time of Flight vs. X focal plane position histogram . . . . .	32
3.9	The momentum calibration of the A1200 focal plane . . . . .	34
3.10	The transmission efficiency of the second half of the A1200 vs. position at the focal plane . . . . .	35
3.11	The $p_{\parallel}$ distributions of $^{10}\text{Be}$ fragments following the breakup of $^{11}\text{Be}$ .	36
3.12	The $p_{\parallel}$ distribution of $^{10}\text{Be}$ fragments following breakup in the Ta target	39
3.13	The widths of the $^{10}\text{Be}$ fragment momentum distributions . . . . .	41

3.14	The $p_{\parallel}$ distributions of $^{10}\text{Be}$ fragments compared with the a projection of the wavefunction of a $2s_{1/2}$ neutron . . . . .	43
3.15	Comparison of the width of the $p_{\parallel}$ distribution of the $2s_{1/2}$ neutron with the $p_{\parallel}$ distribution expected from dipole excitation of $^{11}\text{Be}$ . . .	44
3.16	The $2s_{1/2}$ intruder state dominates the valence neutron wavefunction.	45
3.17	The transverse momentum distribution of $^{10}\text{Be}$ cores following the breakup of $^{11}\text{Be}$ . . . . .	46
3.18	The angular distribution of neutrons following the beakup of $^{11}\text{Be}$ . . .	47
3.19	The probability distribution of nucleons in $^{11}\text{Be}$ . . . . .	49
4.1	The difference between the rms radii of the proton and neutron density distributions in the boron isotopes. . . . .	52
4.2	The breakup cross section of $^8\text{B}$ . . . . .	53
4.3	A schematic illustration showing the overall layout of experimental apparatus used in the $^8\text{B}$ breakup experiment. . . . .	56
4.4	$\Delta E$ vs $E$ showing the particle identification of $^7\text{Be}$ fragments from $^8\text{B}$ .	58
4.5	The $p_x$ distributions of $^7\text{Be}$ fragments following the breakup of $^8\text{B}$ . . .	60
4.6	The $p_{\parallel}$ distributions of $^7\text{Be}$ fragments following $^8\text{B}$ breakup. . . . .	62
4.7	Data from $^8\text{B}$ breakup in the Be target compared with the predicted $p_{\parallel}$ distribution of a p-orbital proton bound by 137 keV in a Woods-Saxon potential. . . . .	64
4.8	The $p_{\parallel}$ distribution of $^7\text{Be}$ fragments following breakup in the Be target predicted by a model that considers the $m_{\ell}$ sub-states of the p-orbital proton in $^8\text{B}$ . . . . .	65
4.9	The predicted shapes of the momentum distributions from E1, E2 and E1+E2 Coulomb breakup of $^8\text{B}$ . . . . .	67
4.10	The $\chi^2$ minimization to obtain the E2 strength that best reproduces the observed $^7\text{Be}$ $p_{\parallel}$ distribution from $^8\text{B}$ breakup on the Au target.	67
4.11	The $^7\text{Be}$ fragment $p_{\parallel}$ data compared with the predicted Coulomb breakup distribution obtained when $\chi^2$ is minimized. . . . .	68
4.12	The probability distribution of nucleons in $^8\text{B}$ . . . . .	70
A.1	The dependence of the rms radius of valence neutrons on binding energy. . . . .	76
A.2	The dependence of the rms radius of a valence proton on binding energy for a nucleus that has four protons in the core, for example $^8\text{B}$ . . . . .	78
B.1	The difference between the proton and neutron density rms radii in light neutron rich nuclei . . . . .	81

B.2	The energy dependence of the $^{11}\text{Be}$ reaction cross section. . . . .	82
B.3	The decay energy spectrum of $^{11}\text{Li}$ from Coulomb Excitation . . . . .	85
B.4	Coulomb reacceleration observed in $^{11}\text{Be}$ breakup on a heavy target . . . . .	87
E.1	The expected $p_{\parallel}$ distributions from a Lorentzian for various transverse acceptance limitations . . . . .	100
E.2	The expected $p_{\parallel}$ distribution from Lorentzian and Gaussian distributions compared with data from the breakup of $^{11}\text{Li}$ in the S320. . . . .	102
E.3	The transmission of the A1200 spectrograph for a Gaussian distribution as a function of its standard deviation. . . . .	104
E.4	The three component Gaussian fit to a Lorentzian distribution . . . . .	105
E.5	The unfiltered and acceptance filtered $p_{\parallel}$ distribution for a $1s_{1/2}$ orbital neutron bound by 500 keV in a Woods-Saxon potential. . . . .	106
F.1	A schematic representation of the Coulomb breakup of $^{11}\text{Li}$ . . . . .	110



# Chapter 1

## Introduction

Until recently, experience with stable nuclei was the only way of predicting the neutron and proton driplines and the nuclear properties of heavy elements that can exist only in stellar interiors. However, beams of short lived nuclei at radioactive isotope facilities have recently permitted experiments that probe the structure of dripline nuclei. These studies permit a determination of the characteristics of these nuclei that will refine the structure models and improve their ability to predict properties of heavier nuclei that are and will remain out of reach, even using state-of-the-art methods for producing unstable nuclei.

Recently, these studies have uncovered a new class of nuclei, halo nuclei. Using reaction cross sections the nuclear size of light neutron-rich isotopes was determined [Tan85a, Tan85b, Tan88] using a Glauber model approach,

$$\sigma_I = \pi[R_I(\textit{target}) + R_I(\textit{projectile})]^2. \quad (1.1)$$

The neutron-rich nuclei  ${}^6\text{He}$ ,  ${}^8\text{He}$ ,  ${}^{11}\text{Be}$ ,  ${}^{14}\text{Be}$ , and  ${}^{11}\text{Li}$  exhibited anomalously large matter radii, Figure 1.1, that do not follow the simple  $r = r_0 A^{1/3}$  rule. These results have subsequently been explained assuming that the valence neutrons form a diffuse halo that surrounds a normal sized core.

The explanation for the two-neutron halo of  ${}^{11}\text{Li}$ , given by Hansen and Jonson

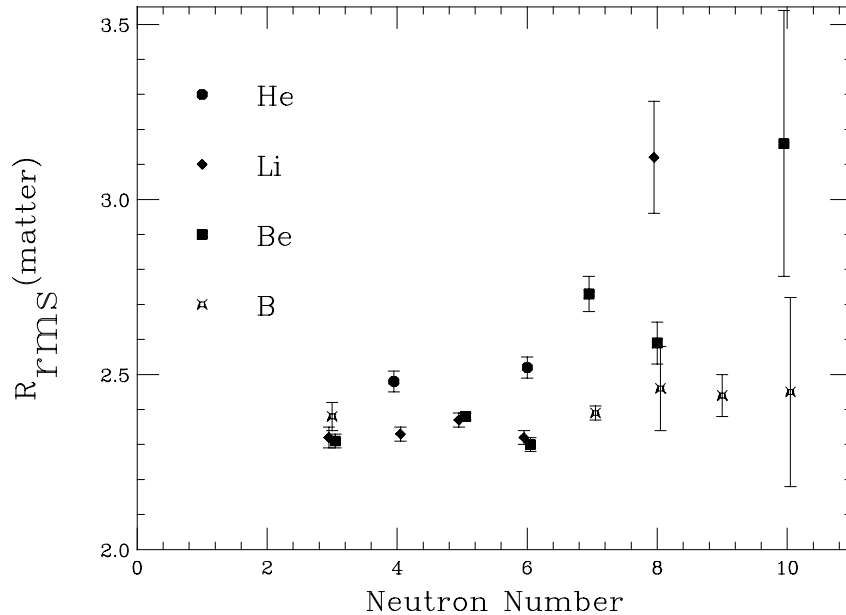


Figure 1.1: The rms radii obtained from the 790A MeV cross section measurements. The nuclei  ${}^6\text{He}$ ,  ${}^8\text{He}$ ,  ${}^{11}\text{Be}$ ,  ${}^{14}\text{Be}$  and  ${}^{11}\text{Li}$  are noticeably larger than other nuclei in this region. Data from [Tan88].

[Han87], was based on a simple assumption that the  ${}^9\text{Li}$  core provides a square-well potential that binds a di-neutron (two neutrons that are strongly correlated). In this model a very low binding energy ( $295 \pm 26$  keV [You93]) permits the two weakly-bound valence nucleons to quantum-tunnel through the wall of the core potential barrier. Assuming no angular momentum barrier the wavefunction outside the core is a Yukawa,

$$\psi(\mathbf{r}) \propto \sqrt{2\pi\rho} \frac{\exp(-r/\rho)}{r}, \quad (1.2)$$

and falls off exponentially with a decay length  $\rho$ ,

$$\rho = \frac{\hbar}{\sqrt{2\mu S_{2n}}}, \quad (1.3)$$

where  $\mu$  is the reduced mass of the system and  $S_{2n}$  is the separation energy for the valence neutrons.

The di-neutron is unbound when free in nature. However, it was hoped that

the presence of the  ${}^9\text{Li}$  core would permit a strong correlation of the two neutrons. Although studies of the correlation of the neutrons emitted in breakup reactions [Iek93] are not consistent with the di-neutron model for  ${}^{11}\text{Li}$ , the simple interpretation of the core-halo neutron system serves as a general guide for understanding halo nuclei. A more detailed discussion of potential barriers is included in Appendix A. A realistic prediction of the nuclear densities in  ${}^{11}\text{Li}$ , Figure 1.2, based on wavefunctions in Woods-Saxon potentials, indicates a sizeable tail in the density distribution.

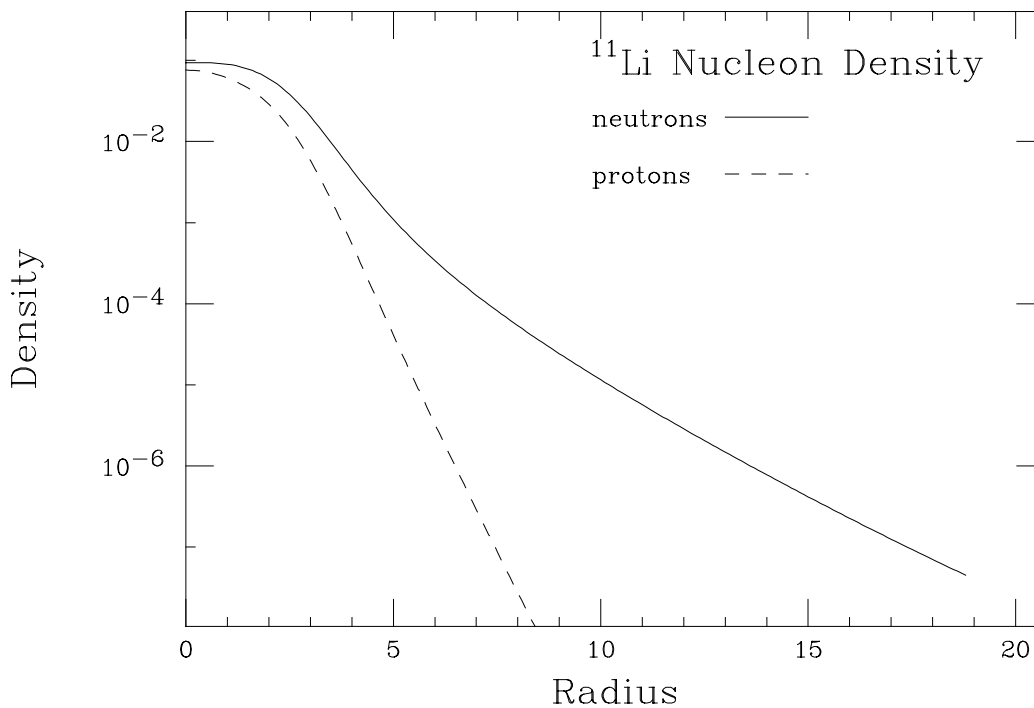


Figure 1.2: [She94] A Woods-Saxon calculation of the proton and neutron density distributions in  ${}^{11}\text{Li}$ .

The rms radius of halo particles can be estimated from a two-body (core-halo) treatment for halo nuclei [Han87].

$$\langle r_{halo}^2 \rangle = \frac{M_{core} + m_{halo}}{m_{halo}} \left[ \frac{M_{core} + m_{halo}}{M_{core}} \langle r^2 \rangle - \langle r_{core}^2 \rangle \right]. \quad (1.4)$$

In Table 1.1 the rms radii of the valence nucleons for a variety of nuclei are calculated.

Table 1.1: The rms radius of valence nucleons (Eq. 1.4) compared with the binding energy. The root-mean-square radii of the core and halo nuclei are taken from the 790A Mev interaction cross section data [Tan85a, Tan85b, Tan88].

Nucleus	Valence Nucleons	Binding Energy (keV)	RMS radius fm
$^{11}\text{Li}$	2n	295	$5.99 \pm 0.52$
$^{11}\text{Be}$	1n	504	$5.66 \pm 0.20$
$^6\text{He}$	2n	970	$4.50 \pm 0.03$
$^8\text{He}$	2n	2137	$3.04 \pm 0.03$
$^9\text{Li}$	1n	4060	$1.99 \pm 0.02$
$^{10}\text{Be}$	1n	6110	$1.46 \pm 0.19$
$^8\text{B}$	1p	137	$3.02 \pm 0.16$

The values are realistic for nuclei like  $^{11}\text{Li}$  and  $^{11}\text{Be}$ . However, for tightly bound nuclei, such as  $^9\text{Li}$  and  $^{10}\text{Be}$ , the two-body assumption leads to unrealistic values; for example, the rms radius of the valence nucleon is smaller than the rms radius of the core nucleus.

The simple two- and three-body nature of halo nuclei permits a treatment where the removal of halo nucleons probes the wavefunction of the halo nucleons. Appendix B summarizes experiments that show the presence of neutron halos in  $^{11}\text{Li}$  and  $^{11}\text{Be}$ , for the interested reader.

In the Serber limit, the momentum distributions of core and halo fragments following breakup are related to the Fourier Transform of the spatial wavefunction of the halo nucleon [Ser47]. A narrow momentum distribution implies a broad spatial distribution. Reactions that strip off halo nucleons, leaving the core intact, are particularly interesting since they sample the wavefunction of the halo nucleon primarily when the core-halo separation distance is large. Hence studies of core fragments should be sensitive to the details of the halo wavefunction in the region of interest where the halo extends beyond the core.

The three-body nature and low binding energy of  $^{11}\text{Li}$  pushed studies of this nucleus to the forefront in radioactive beam experiments. However, the interpretation of fragment momentum distributions from  $^{11}\text{Li}$  was complicated by a combination of reaction mechanism and final state interaction effects. For example, the Serber model assumes a direct breakup which implies that the two neutrons are emitted simultaneously. In this case, measurements probe the ground state of  $^{11}\text{Li}$ . However, some breakup events proceed by a sequential emission of the two neutrons and are sensitive to the properties of the unbound nucleus  $^{10}\text{Li}$ . Because the relative contributions of simultaneous and sequential breakups are not well known, uncertainties exist in the interpretation of results.

To resolve issues of the influence of reaction mechanism effects we measured the momentum distribution of  $^{10}\text{Be}$  core fragments following the breakup of a simple two-body system,  $^{11}\text{Be}$ . In Chapter 2 issues relevant to measurements of momentum distributions are discussed, and in Chapter 3 the distribution of  $^{10}\text{Be}$  fragment momentum parallel to the beam direction ( $p_{\parallel}$ ) following  $^{11}\text{Be}$  breakup is discussed. The advantages of this measurement are two-fold. The  $p_{\parallel}$  should directly reflect the momentum wavefunction of the halo neutron [Ber92], and the method utilized a high resolution spectrometer technique to measure the momentum distribution. We observed narrow distributions for a wide range of breakup targets (from Be to U) and found excellent agreement when the data was compared with a single particle calculation for a  $2s_{1/2}$  neutron in a Woods-Saxon potential which has a rms radius of 6.5 fm [Esb94]. This appears to indicate that the halo neutron momentum wavefunction is measured.

In Chapter 4 measurements of the momentum distribution of  $^7\text{Be}$  fragments following the breakup of  $^8\text{B}$  are presented. A recent measurement of the  $^8\text{B}$  quadrupole moment suggests that it possesses a prominent proton halo [Min92]. However, the

earlier reaction cross section measurements had not found evidence for a proton halo [Tan88]. Therefore, the momentum distributions of breakup  ${}^7\text{Be}$  core fragments provide a measurement of the proton rms radius from a perspective that is different from previous measurements. The distributions are narrow; however, they are not in agreement with a simple prediction based on the wavefunction of a p-orbital proton in a Woods-Saxon potential [Esb95]. In this case, it is necessary to include reaction mechanism effects; this leads to good agreement with the data. The wavefunction has a rms radius of 4.24 fm and is significantly larger than the  ${}^7\text{Be}$  [Esb95] core. However, the size of the proton halo of  ${}^8\text{B}$  is small when compared with the neutron halo of  ${}^{11}\text{Be}$ .

# Chapter 2

## Projectile-like Fragment Momentum Distributions

Momentum distributions of projectile-like fragments (fragments with velocities similar to that of the incoming projectile) have been measured for a wide range of stable projectile nuclei, i.e.  $^{12}\text{C}$ ,  $^{14}\text{N}$ , and  $^{16}\text{O}$  [Kid88, Gla90, Van79]. The momentum distribution widths are generally broad, on the order of 180 MeV/c and larger. Core and halo fragments following the breakup of halo nuclei have narrow momentum distribution widths ( $\sim 45$  MeV/c), in reasonable agreement with the Fourier transform of simple predictions for the halo neutron wavefunctions based on the low binding energies. It appears that the narrow momentum distributions reflect, via the uncertainty principle, the large spatial distribution of valence nucleons. Thus momentum distributions provide convincing evidence for neutron halos.

### 2.1 Momentum Distributions

When a projectile interacts with a target nucleus it can be broken apart or fragmented. The breakup fragments can be described in terms of two momentum components, one parallel with the beam velocity ( $p_{\parallel}$ ) and the other perpendicular to the beam velocity ( $p_{\perp}$ ). Experience with stable nuclei has led to the following general observations.

When Coulomb deflection contributions are taken into account the  $p_{\parallel}$  distributions of fragments have widths in relatively good agreement with the  $p_{\perp}$  distributions [Van79]. The  $p_{\parallel}$  distribution widths observed for light targets are generally the same as the  $p_{\parallel}$  distribution widths for breakup on heavy targets [Gla90]. A brief summary of fragmentation models is in Appendix C.

The nucleus  $^{11}\text{Li}$  is interesting because of its three-body, n-n- $^9\text{Li}$ , structure. However, a review of measurements of the fragment momentum distributions from  $^{11}\text{Li}$  breakup, in the following sections, shows the need to study a simpler two-body system.

## 2.2 Fragment Transverse Momentum Distributions from $^{11}\text{Li}$ Breakup

### 2.2.1 $^9\text{Li}$ Core $P_{\perp}$ Distributions

A narrow width was observed in the transverse momentum distribution of  $^9\text{Li}$  fragments from  $^{11}\text{Li}$  breakup showing, via Fourier transform, the presence of the halo [Kob88]. The distribution was initially fit with a two-component Gaussian shape, Figure 2.1. The first component was broad,  $224 \pm 28$  MeV/c Full Width at Half Maximum, while the other component was much narrower,  $54 \pm 28$  MeV/c FWHM [Kob88]. The broad component, which has a width similar to that expected from fragmentation of normal nuclei, was attributed to the removal of tightly bound neutrons from the normal sized  $^9\text{Li}$  core of  $^{11}\text{Li}$ , while the narrow component is associated with the removal of the weakly bound valence neutrons from the halo.

However, there is a problem with this interpretation since the relative contributions from each of the components (broad 70%, narrow 30%) is different from what is expected from a halo nucleus; the component associated with the removal of halo neutrons should dominate the cross section. A Gaussian (or sum of Gaussians)

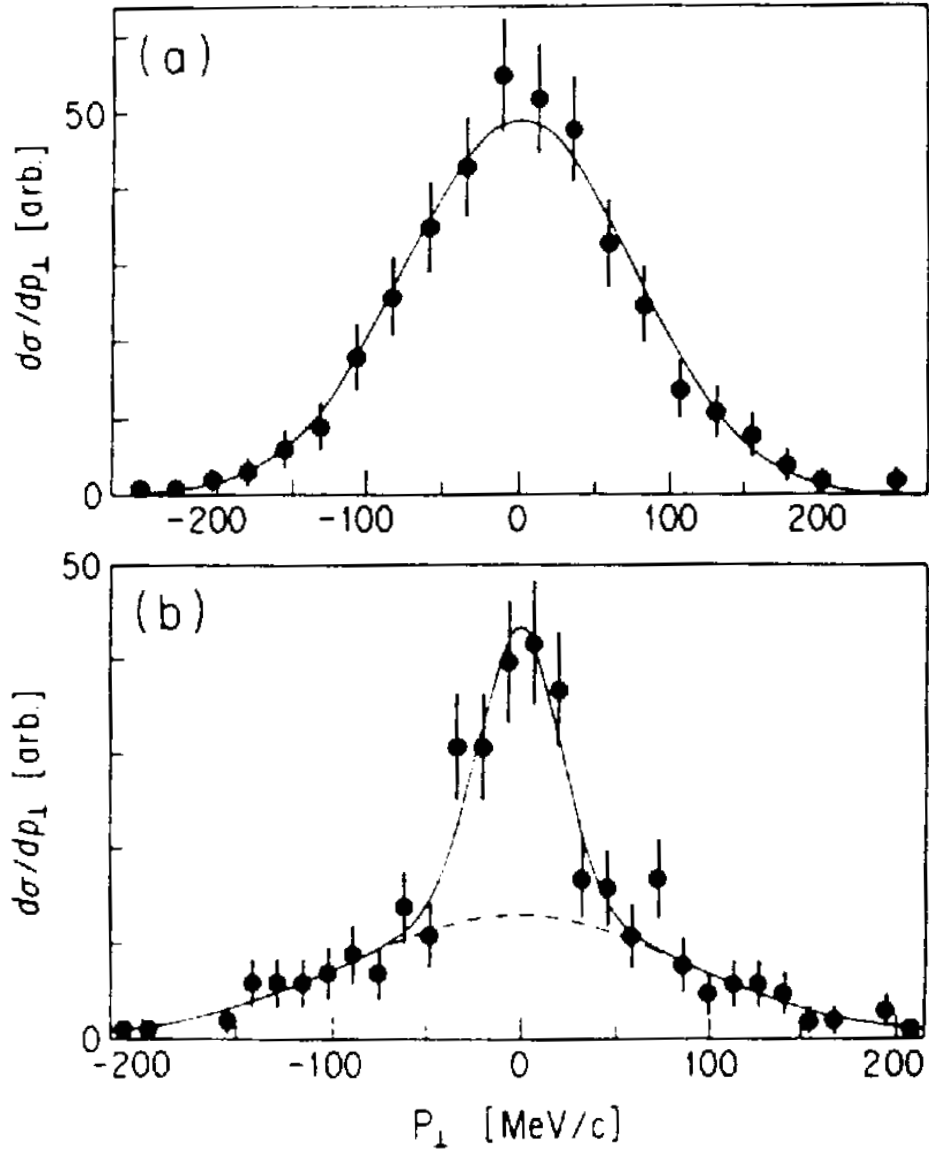


Figure 2.1: [Kob88] The transverse momentum distribution of core fragments following the breakup of 790A MeV ions in a carbon target. In (a) is a relatively broad distribution, 188 MeV/c FWHM, observed for  ${}^6\text{He}$  fragments from  ${}^8\text{He}$ . The  $p_{\perp}$  distribution of  ${}^9\text{Li}$  fragments following the breakup of  ${}^{11}\text{Li}$  is shown in (b) and is fit with two Gaussian components, 54 MeV/c FWHM and 224 MeV/c FWHM.

momentum distribution is not expected on any a priori grounds; therefore, further consideration of the shape of the fragment momentum distributions from halo nuclei was necessary.

As has been shown earlier, Hansen and Jonson [Han87] suggest that the wavefunction of halo nucleons outside the core will decrease exponentially with the shape associated with a Yukawa wavefunction, Equation 1.2. Since the Fourier transform of a Yukawa is a Lorentzian,

$$\Psi(\mathbf{p}) = \sqrt{\frac{\Gamma}{2\pi^2}} \frac{1}{\mathbf{p}^2 + \Gamma^2/4} \quad (2.1)$$

and

$$\Gamma = 2\sqrt{2\mu S_{2n}}, \quad (2.2)$$

a Lorentzian description of the core and halo fragment momentum distributions is a reasonable first approximation.

### 2.2.2 Neutron Angular Distributions

The angular distribution of neutrons from the breakup of  $^{11}\text{Li}$ , Figure 2.2, indicated a width of  $24 \pm 4$  MeV/c FWHM [Ann90]. This was much narrower than any previously measured fragment momentum distribution width and less than half the width of the  $p_{\perp}$  distribution of the  $^9\text{Li}$  cores. The narrow width is attributed both to the presence of the halo and to the fact that the neutrons are uncorrelated. This raised issues of the effects of the reaction mechanism and final state interaction effects.

## 2.3 Breakup Reaction Mechanisms

Because there are concerns that perturbations associated with the reaction mechanisms influence the distributions, a discussion of the most significant breakup processes (stripping, diffraction dissociation and Coulomb dissociation) is necessary.

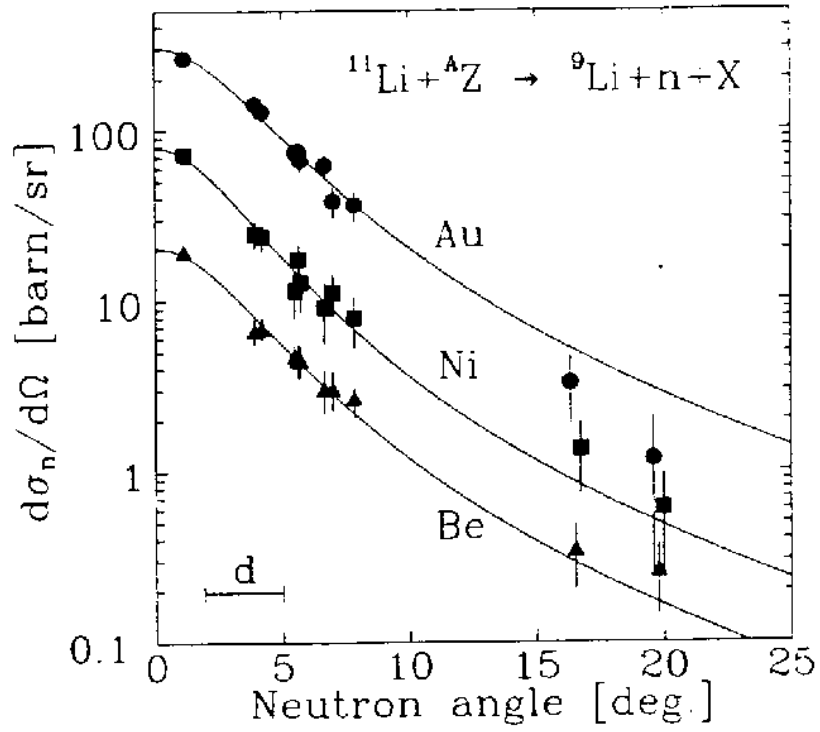


Figure 2.2: [Ann90] The angular distribution of neutrons following the breakup of  $^{11}\text{Li}$  are compared with Lorentzian shapes. The deduced widths are small,  $24 \pm 4$  MeV/c FWHM.

### 2.3.1 Stripping

In 1947 Serber interpreted the momentum distribution of neutrons produced when a 190 MeV beam of deuterons impinged on a target [Ser47]. A direct breakup process, stripping, was assumed. Stripping removes nucleons from the projectile when they come into contact with the target nucleus. The process can also be termed absorption since nucleons are absorbed or removed from the projectile by the target. This model assumes that the halo particle can be removed by an interaction sufficiently weak that the core momentum is unaffected by the breakup. It is also necessary that the core fragment momentum is not greatly affected by final state interactions while leaving the scene of the breakup. When halo nucleons are stripped away from the projectile the remaining core nucleons continue in their original motion. Therefore, the trajectory of the fragment is determined by the collective motion of the surviving nucleons at the instant of the breakup. In the case of a halo-core system the simple two-body nature implies, by conservation of momentum, that the core momentum reflects the momentum wavefunction of the halo nucleon.

### 2.3.2 Diffraction Dissociation

Another mechanism that induces breakup reactions is diffraction dissociation [Gla55]. Glauber explained that in diffraction dissociation the wavefunctions of a nucleons in a nucleus are localized as it approaches a target nucleus (assumed to to be a black disk). Portions of the wavefunctions become restricted, and the reduction in the volume of the wavefunctions increases the total energy of the system so that the nucleus is no longer in the ground state. The resulting excited nucleus is comprised of an admixture of excited states which decays.

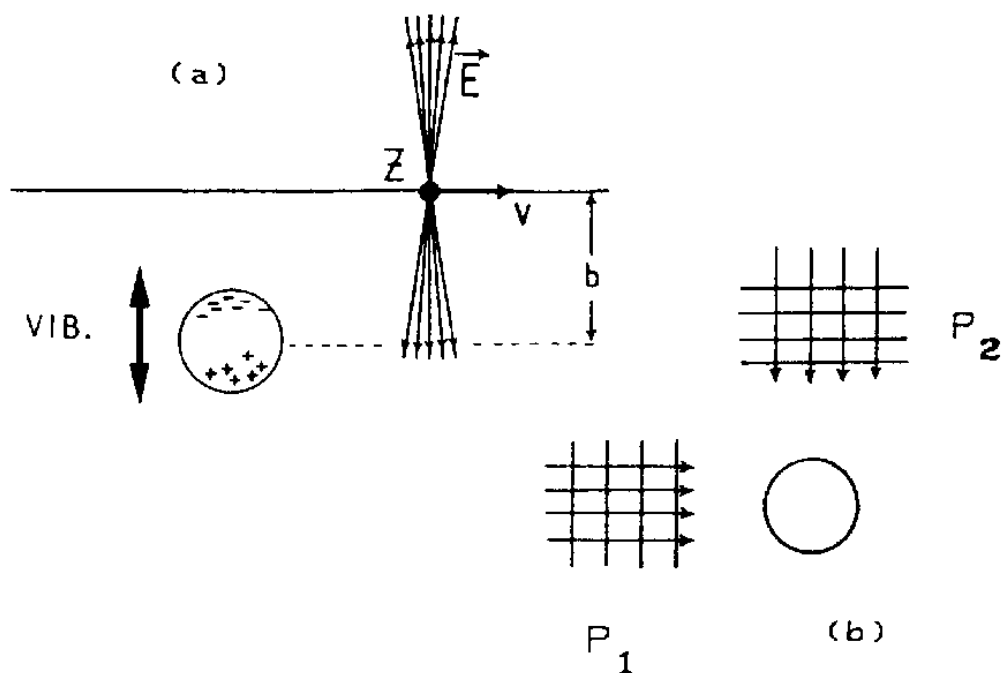


Figure 2.3: [Ber88] As a projectile approaches a target nucleus, the electric field lines are contracted into the plane which is perpendicular to the direction of travel. The resulting electric and magnetic field lines, that can be approximated with two plane waves, Coulomb excite the passing nucleus.

### 2.3.3 Coulomb Dissociation

The final breakup mechanism to be considered is Coulomb dissociation. The very low binding energy of halo nuclei leads to a large Coulomb dissociation cross sections, and the breakup mechanisms for halo nuclei are dominated by Coulomb processes for heavy targets [Bla91]. Coulomb excitation processes are discussed, for example in Winther and Alder [Win79] and the Electrodynamics text of J.D. Jackson [Jac75]; a straightforward development by Bertulani and Baur [Ber88] is summarized in Appendix D.

Coulomb excitation occurs when a projectile enters the Coulomb field of a target nucleus. The electric field of the target nucleus is contracted into the plane which is transverse to the incident direction of travel (chosen as the Z axis in Figure 2.3). The resulting electric and magnetic fields are associated with a spectrum of virtual photons which excite the projectile. With these considerations, the probability for excitation via dipole (E1) photons can be calculated, and the momentum distribution of fragments from Coulomb dissociation reflects the dipole excitation strength function.

Esbensen and Bertsch [Esb92] find that the dipole operator does not change the momentum of the breakup fragments much, and thus in halo nuclei the ground state halo particle momentum distribution should be similar to the momentum distribution of the dipole excitation strength. Therefore, although the reaction mechanism changes when considering breakup reactions on light and heavy targets the momentum distributions remain similar and primarily reflect the wavefunction of the halo nucleons.

Dipole excitation is the primary contributor to breakup at intermediate energies. Because excitation by E2 photons is generally much smaller than that of E1 excitation,

the E2 contribution is often neglected.

The predicted Coulomb breakup energy distribution in the projectile rest frame is obtained using this method. Further consideration of experimental conditions leads to the  $p_{\parallel}$  and  $p_{\perp}$  distributions of breakup fragments. When the target  $Z$  is sufficiently large, the Coulomb breakup cross section is much larger than the nuclear breakup cross section in halo nuclei, and there is little need to consider influences from nuclear processes.

### 2.3.4 Reaction Mechanism Effects on Momentum Distributions

Reaction effects influence measurements of neutrons and core fragments and measurements of the parallel and transverse components of fragment momentum in different ways. Absorption strongly affects neutrons since it is possible for the neutron to collide with a target nucleus and then scatter with a momentum that no longer reflects the initial state wavefunction. When a core fragment strikes a target nucleus it will likely be disintegrated as a result. Therefore, the momentum distribution of core fragments is less affected by absorptive effects than the momentum distribution of neutrons. In an extreme limit, absorption could lead the  $p_{\perp}$  distribution to become a Fraunhofer diffraction pattern, while the effect on the  $p_{\parallel}$  component narrows the distribution slightly [Ber92].

Diffraction influences the neutron and core fragments equally. However, since diffraction localizes the wavefunctions in the transverse direction, and not in the longitudinal direction, the  $p_{\parallel}$  distributions are only weakly perturbed [Bar95].

Finally, the initial and final state interactions associated with high  $Z$  targets are mainly from Coulomb deflection and multiple elastic scattering effects. These act in the direction perpendicular to the beam direction.

## 2.4 The $P_{\parallel}$ Distribution of ${}^9\text{Li}$ Fragments from ${}^{11}\text{Li}$ Breakup

Bertulani and McVoy showed that  $p_{\parallel}$  of core fragments measures the internal momentum of the halo particle and is relatively insensitive to the details of the interaction for both nuclear and Coulomb processes [Ber92]. A measurement of  ${}^9\text{Li}$  fragments following the breakup of  ${}^{11}\text{Li}$  fragments, at the NSCL, found that the  $p_{\parallel}$  distributions for Be, Nb and Ta [Orr92] and U [Orr95] targets are similar in width (around 45 MeV/c FWHM). The data agree with a prediction based on the momentum wavefunction of the two halo neutrons, Figure 2.4. Therefore, it appeared that  $p_{\parallel}$  distributions accurately reflect momentum wavefunctions.

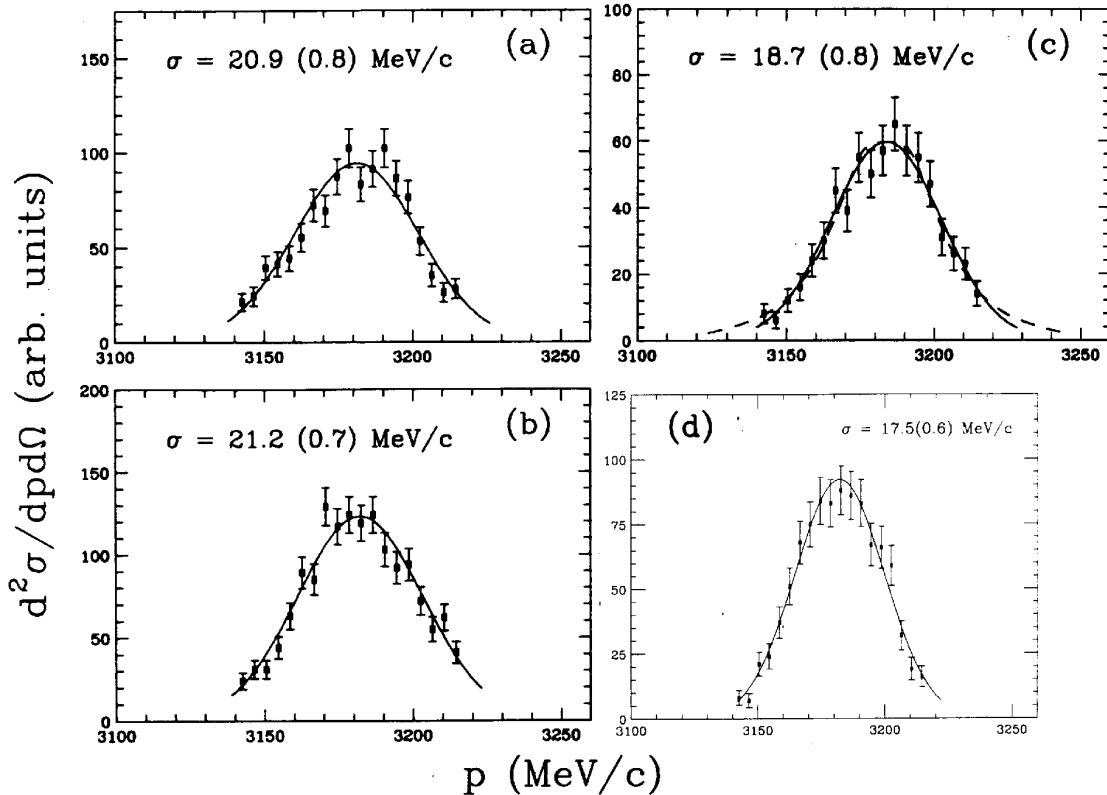


Figure 2.4: [Orr92] and [Orr95] The  $p_{\parallel}$  distribution of  ${}^9\text{Li}$  fragments following the breakup of 66A MeV  ${}^{11}\text{Li}$  in  ${}^9\text{Be}$ ,  ${}^{93}\text{Nb}$ ,  ${}^{181}\text{Ta}$  and  ${}^{238}\text{U}$  targets, (a) through (d) respectively. In (c) the dashed line is a dipole excitation calculation, Section 2.3.3, that is in excellent agreement with the data.

### 2.4.1 Problems with the ${}^9\text{Li}$ $P_{\parallel}$ Distributions

Data from the  ${}^9\text{Li}$   $p_{\parallel}$  distributions following the breakup of  ${}^{11}\text{Li}$  [Orr95] have provided room for discussion of how well we understand the reactions. The  $p_{\parallel}$  distribution from breakup on the Ta target is in agreement with the calculated momentum wavefunction of the halo neutrons and supports the Serber model approach. However, the widths of the distributions from breakup on other targets decrease slightly with increasing target mass.

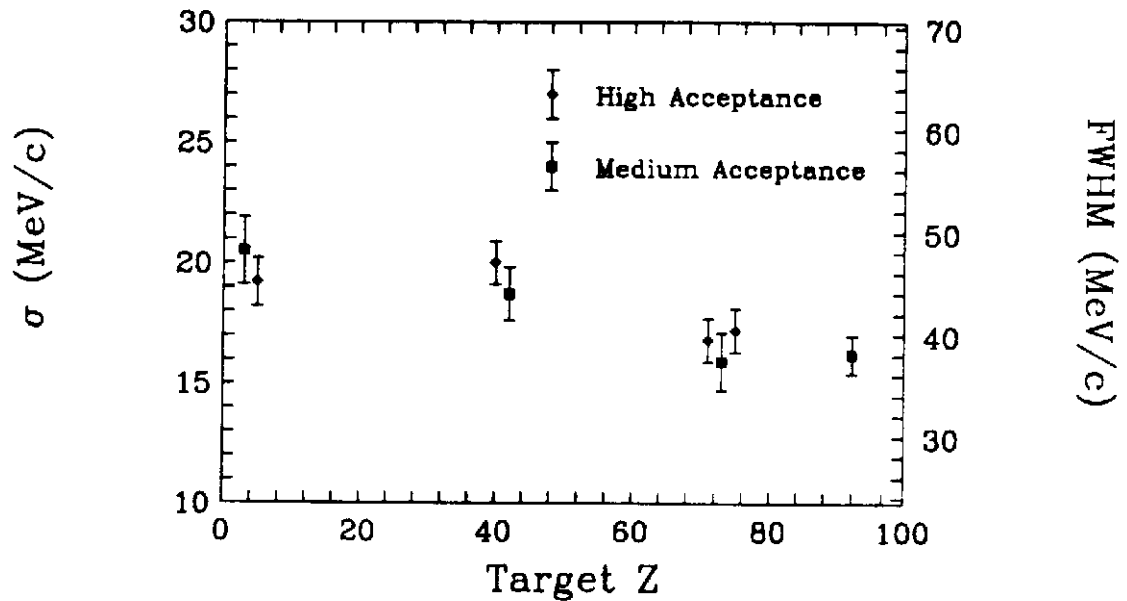


Figure 2.5: [Orr95] The  $p_{\parallel}$  distribution widths of  ${}^9\text{Li}$  fragments from  ${}^{11}\text{Li}$  breakup have a slight target  $Z$  dependence.

### Three-body Effects

There are complications in  ${}^{11}\text{Li}$  breakup due to reaction mechanism effects or, possibly, three-body effects. For example, breakups on the light target may proceed mainly via sequential emission of the neutrons while breakups on the heavier target would be expected to proceed by simultaneous emission of the two neutrons [Bar93]. This would

lead to different momentum distribution widths for light and heavy targets. Accurate predictions require a precise knowledge of the structure of the nuclei that participate in the breakup. However, existing uncertainties in experimental measurements, which are quite large in some cases, limit our understanding in complicated three-body systems.

Essential issues in the problem, for  $^{11}\text{Li}$ , are uncertainties in the ground state properties of  $^{11}\text{Li}$  and  $^{10}\text{Li}$ . Measurements of the  $^{11}\text{Li}$  binding energy were not in agreement ( ranging from  $170\pm 80$  keV [Thi75] to  $340\pm 50$  keV [Kob92] ), and the accepted value of  $295\pm 26$  keV [You93], which is a weighted result based on all measurements to date, has a sizeable uncertainty.

The ground state properties of  $^{10}\text{Li}$  are critical in sequential breakups. However, since  $^{10}\text{Li}$  is unbound it is difficult to study. Young *et al.* [You94] suggested that the low-lying structure is made up of a p-orbital state at 538 keV and a s-orbital state in the range of  $\leq 100$  keV. This just unbound s-orbital state was corroborated by a  $0^\circ$  sequential neutron decay spectroscopy measurement [Kry93]. This indicates that s-orbitals comprise a significant percentage of the wavefunction for the valence neutrons of  $^{11}\text{Li}$ . Because the angular momentum barrier is critical to the long range behavior of the wavefunction, this discovery significantly influenced the interpretation of some measurements.

## 2.5 Need to Study a Simpler System

These results for  $^{11}\text{Li}$  have led to a cross-road in the study of two-neutron halo nuclei. Evidence of the halo is observed. However the sensitivity to reaction mechanism effects, initial and final state interactions, and uncertainties in the ground state properties of the participating nuclei leads to an unacceptable level of uncertainty in the

results. The interplay between halo effects and reaction effects mandates studies on simpler two-body (one nucleon halo) systems to provide a basis for complete understanding of the more complicated three-body systems.



## Chapter 3

# The Neutron Halo of $^{11}\text{Be}$

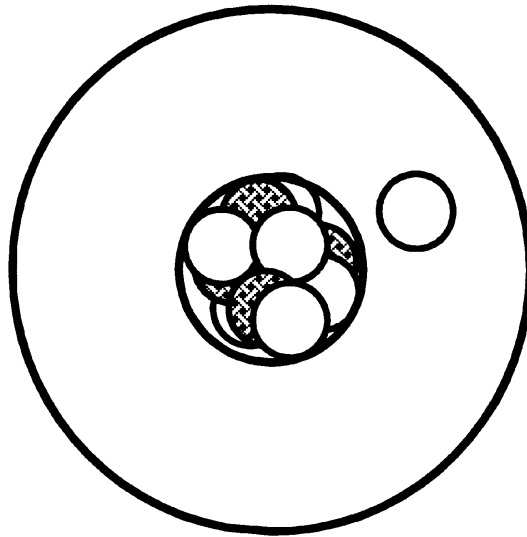


Figure 3.1: The nucleus  $^{11}\text{Be}$  is comprised of a normal sized  $^{10}\text{Be}$  core (2.30 fm) immersed in a neutron halo that has a rms radius of 6.5 fm.

In the early 1960s  $^{11}\text{Be}$  attracted attention because the parity of its ground state is inverted when compared to the simple shell model expectation [Sag93]. Therefore many of the important nuclear model parameters have been measured, and  $^{11}\text{Be}$  is well characterized. The parity inversion leads the ground state to be primarily determined by a single particle  $2s_{1/2}$  neutron state instead of the  $1p_{3/2}$  state. Although  $^{12}\text{Be}$  and

$^{14}\text{Be}$  are more neutron rich than  $^{11}\text{Be}$ , they are more tightly bound because of pairing effects. Therefore, the rms radii of their valence neutrons are not as large as the rms radius of the valence neutron of  $^{11}\text{Be}$ . Since  $^{11}\text{Be}$  breakup is not troubled by three-body issues it should provide a less complicated determination of halo characteristics than measurements on  $^{11}\text{Li}$ .

The binding energy of the valence neutron in  $^{11}\text{Be}$  has been measured precisely,  $504\pm 6$  keV [Ajz90], and the lack of an angular momentum barrier for the valence neutron makes the potential shape rather simple. A measurement of the spectroscopic factor indicates that the  $2s_{1/2}$  intruder state comprises nearly 77 % of the wave function [Ajz90]. Therefore, in the treatment of Hansen and Jonson [Han87] the extent of the halo is proportional to the square root of the binding energy with few other influences. Using a more realistic Woods-Saxon potential, with the depth adjusted to reproduce the binding energy [Esb94], Esbensen finds that the rms radius of the halo neutron is 6.5 fm when the radius of the core potential is chosen to match the measured radius of  $^{10}\text{Be}$  (2.30 fm [Tan88]).

### 3.1 The $P_{\parallel}$ Distribution of $^{10}\text{Be}$ Fragments from $^{11}\text{Be}$ breakup

We chose to study the  $p_{\parallel}$  distribution of  $^{10}\text{Be}$  fragments following the breakup of  $^{11}\text{Be}$ , because the  $p_{\parallel}$  distribution of core fragments should most accurately reflect the momentum wavefunction of the halo nucleon [Ber92, Ban93, Sag94].

### 3.1.1 The A1200 Fragment Separator

#### Production of the $^{11}\text{Be}$ beam

At the NSCL the method for producing beams of neutron rich nuclei near the drip-line is fragmentation [She92]. In this experiment the Radioactive Nuclear Beam (RNB) was produced when 80A MeV  $^{18}\text{O}$  ions, from the K1200 cyclotron, impinged on a 790 mg/cm<sup>2</sup> natural Be target. Just after the target, the resulting RNB consisted of particle stable isotopes ranging from  $^{17}\text{O}$  to the lighter particles like protons, deuterons and tritons. The makeup of this beam can be easily understood in the treatment of Goldhaber, discussed in Section C.1.

#### A1200 Radioactive Beam Facility

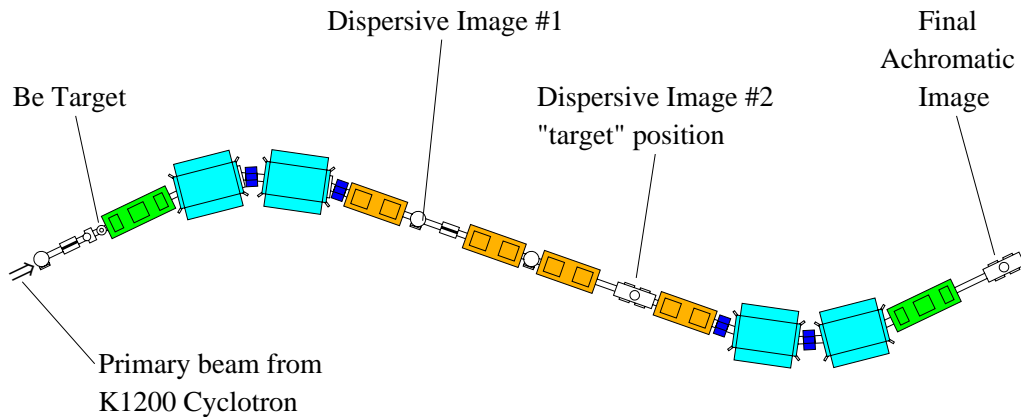


Figure 3.2: The A1200 fragment separator and beam analysing device.

The members of a RNB travel with nearly the beam velocity, and are filtered by the A1200 fragment separator. Most light ions produced in this manner are fully stripped of electrons, and by passing this beam through a magnetic dipole and then an aperture at a momentum dispersive image (see Figure 3.2) nuclei are separated by  $\mathbf{p}/q$ . For fully stripped ions traveling with exactly the same velocity, this gives separation by  $(m/q)$  or  $(A/Z)$ . However, because the fragments actually have a spread in velocity

centered around the beam velocity, or may not be fully stripped, the separation is not complete.

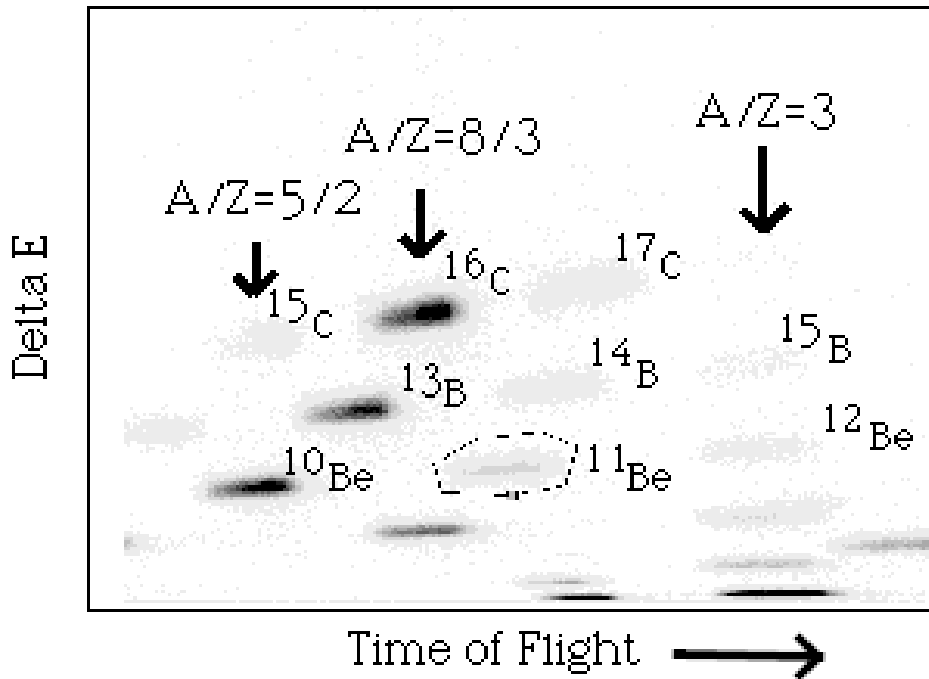


Figure 3.3: A plot of  $\Delta E$  vs. ToF which shows the isotopic separation of fragments that are analyzed in the A1200. The  $^{11}\text{Be}$  beam group is circled.

After the aperture  $A/Z$  groups are dispersed by different velocities (or times of flight through the A1200, ToF). Isotope groups are commonly identified by measuring both the energy (or energy loss) and the velocity of beam particles. Figure 3.3 shows  $\Delta E$  vs ToF for a particular spectrometer setting. In the figure the straight vertical line of isotopes is the  $A/Z=3$  line. Observable in this group, whose members all have the same ToF, are  $^{18}\text{C}$ ,  $^{15}\text{B}$ ,  $^{12}\text{Be}$ ,  $^9\text{Li}$ ,  $^6\text{He}$  and  $^3\text{H}$ , from the top to the bottom. Two other groups of isotopes that have identical velocities are present; they are the  $A/Z=8/3$  ( $^{16}\text{C}$  and  $^8\text{Li}$ ) and the  $A/Z=5/2$  ( $^{15}\text{C}$  and  $^{10}\text{Be}$ ) groups.

Table 3.1: The isotopes comprising the produced RNB after the first set of A1200 dipoles. Protons, deuterons tritons and  $\alpha$ 's are omitted.

Isotope	Percent of the RNB
${}^6\text{He}$	2.55
${}^8\text{Li}$	7.39
${}^9\text{Li}$	1.33
${}^{10}\text{Be}$	14.02
${}^{11}\text{Be}$	2.43
${}^{12}\text{Be}$	0.30
${}^{13}\text{B}$	14.35
${}^{14}\text{B}$	0.81
${}^{15}\text{B}$	0.10
${}^{15}\text{C}$	0.49
${}^{16}\text{C}$	21.23
${}^{17}\text{C}$	1.27
${}^{18}\text{C}$	0.01

The nucleus of interest is  ${}^{11}\text{Be}$ . The beam is selected by adjusting the first set of dipoles in the A1200 to maximize the rate of  ${}^{11}\text{Be}$  ions that pass through the momentum aperture located at Image 1. The rate was optimized at 4300  ${}^{11}\text{Be}$  particles per second with a field strength of 1.03034 Tesla. The central radius of the dipoles,  $\rho$ , at this field setting is 3.105 meters, and the energy of the  ${}^{11}\text{Be}$  beam is 63A MeV. The size of the aperture at the image permitted a  $\pm 0.5\%$  spread spread in the beam momentum which translates into approximately a  $\pm 1\%$  spread in the beam energy. The purity of the beam was not very good (2.4%  ${}^{11}\text{Be}$  ). However, as will be discussed later, the contaminants do not significantly affect the measurement of the  ${}^{10}\text{Be}$  fragment momentum distribution.

### The Principle of a Dispersion-matched Energy-loss Spectrometer

A dispersion-matched energy-loss spectrometer makes it possible to compensate for the energy spread of a beam with the correct achromatic optical conditions. Thus, in

spite of the relatively large spread in momentum of a produced RNB (up to 3% in the A1200) it is possible to measure, for example, transfer reactions with a momentum resolution of 0.05% [She92].

In this mode the first object position is located at the RNB production target, at the start of the A1200 Spectrograph. The produced fragments pass through a set of superconducting  $22.5^\circ$  dipoles, where the fragments are separated by  $\mathbf{p}/q$ . At the exit of the dipole set is a momentum dispersed image in the horizontal direction, Image 1. The momentum aperture located at this image permits, in our case, a spread of  $\pm 0.5\%$  in momentum for the produced  $^{11}\text{Be}$  beam.

An achromatic device must have an even number of images between the dipoles, and the A1200 is operated with two. One is at Image 1, and the other is at Image 2. The optics following the center pot are nearly a mirror reflection of the optics preceding the center pot of the A1200, so that in the second half of the A1200 the beam returns to an achromatic focus at the final image. As mentioned above, under optimum conditions the optics correct for the spread in momentum of the produced RNB so that all beam particles focus at a point at the final image.

A simple application of the Dispersion Matched Energy Loss Spectrometer technique is the measurement of target thicknesses. As described above when fragments are produced at the target position they are focused to a point at the focal plane. When a target is placed at the second dispersive image, the position of this focus point shifts on the focal plane because of the energy loss in the target. By adjusting the fields of the magnets that follow the target, the position of the focus can be returned to the center of the focal plane. This high resolution measurement of the energy loss of particles passing through a target permits a deduction of the target thickness.

Breakup fragments can be studied in a similar manner. When a breakup target

## Dispersion-Matched Energy-Loss Spectrometer

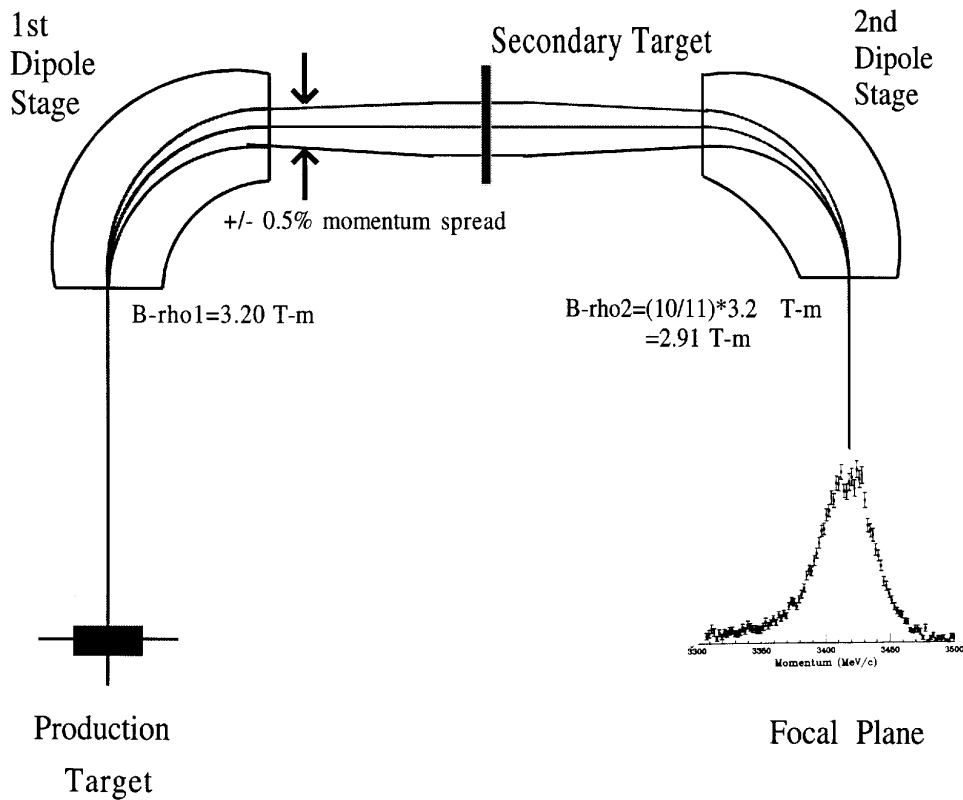


Figure 3.4: The principle of a dispersion matched energy loss spectrometer. A RNB has a momentum spread that is introduced by the production mechanism. However, the optics of the device return the beam to an achromatic focus at the focal plane. The spread in momentum of fragments produced at the secondary target is projected onto the focal plane.

is inserted at the Image 2 position, the magnetic fields can be adjusted to position the centroid of a particular fragment momentum distribution at the center of the focal plane (Figure 3.4). Since the momentum distribution of breakup fragments has a spread, it is projected onto the focal plane. This method measures the total momentum of breakup fragments. However, when the components ( $p_{\parallel}$  and  $p_{\perp}$ ) of the momentum are considered for a narrow distribution centered near 3400 MeV/c,  $p_{total} = \sqrt{p_{\parallel}^2 + p_{\perp}^2} \approx p_{\parallel}$  within 0.05%. Therefore, measurements of fragment momentum distributions with this technique serve as measurements of the  $p_{\parallel}$  distribution.

## Detector System

A standard A1200 detector setup identified the particles reaching the Focal Plane. A gas ionization chamber provided the energy loss signal, while a thick plastic stopping scintillator provided both a total energy signal and a start signal for timing information. The Time of Flight (ToF) measurement is made relative to the cyclotron rf-signal which has a period of 55 ns. The Z of a particle can be easily determined from a plot of  $\Delta E$  vs E, and as seen in Figure 3.3 isotopic resolution is obtained from a plot of  $\Delta E$  vs ToF when the A1200 spectrometer is operated in a simple transmission mode. A pair of two-dimensional position-sensitive Parallel Plate Avalanche Counters (PPAC) located at the Focal Plane (separated by 37.4 cm) measured the trajectories of the incoming particles. The second of these PPACs, historically known as PPAC3, was located at the focus and measured the position at the Focal Plane, which is related to the momentum of the particles. Four Si diodes located near the production target monitored the primary  $^{18}\text{O}$  beam intensity.

### 3.1.2 Analysis of $^{10}\text{Be}$ Fragment Momentum Distributions

In order to identify the  $^{10}\text{Be}$  fragments following  $^{11}\text{Be}$  breakup in the Image 2 target a straightforward approach is used. The  $^{10}\text{Be}$  reaction products travel with nearly the same speed as the incoming  $^{11}\text{Be}$  particles. When their speed is the same, the energy loss of  $^{10}\text{Be}$  ions in the Ionization Chamber is nearly the same as the energy loss of  $^{11}\text{Be}$  ions. For example, the  $^{10}\text{Be}$  breakup fragments have a larger energy loss per nucleon than  $^{11}\text{Be}$  particles that pass through the Ionization Chamber. Therefore to a good approximation  $^{10}\text{Be}$  fragments produced from  $^{11}\text{Be}$  breakup in the Image 2 targets have the same  $\Delta E$  and ToF as the  $^{11}\text{Be}$  group in Figure 3.3. Small changes in the velocity due to the energy lost in the breakup target lead to a slightly longer ToF and a slightly higher energy loss in the ionization chamber. The same contour that showed the  $^{11}\text{Be}$  group in Figure 3.3 is shown in Figure 3.5. It is important to note that Figure 3.3 was produced when a 3% momentum aperture was at Image 1, while all breakup data was collected using a 1% momentum aperture. The momentum spread of the secondary beam is important for determining the spread in ToF of fragments reaching the Focal Plane. Therefore, in Figure 3.5 the size of the spot for the  $^{10}\text{Be}$  breakup fragment group, collected with the 1% momentum aperture, is roughly three times smaller than in Figure 3.3.

#### Scattered Beam Contaminant

It is clear from the figure that this simple approach is not sufficient for selecting the  $^{10}\text{Be}$  breakup fragment group since two groups fall within this region. When certain reactions are studied in the A1200 problems can arise due to beam particles that scatter off the sides of the dipoles and reach the focal plane. Most RNB particles that do not have a reaction in the Image 2 target are stopped in the dipoles. In Figure 3.5 seven groups are labeled. The first of these groups is the  $^{10}\text{Be}$  breakup group, while

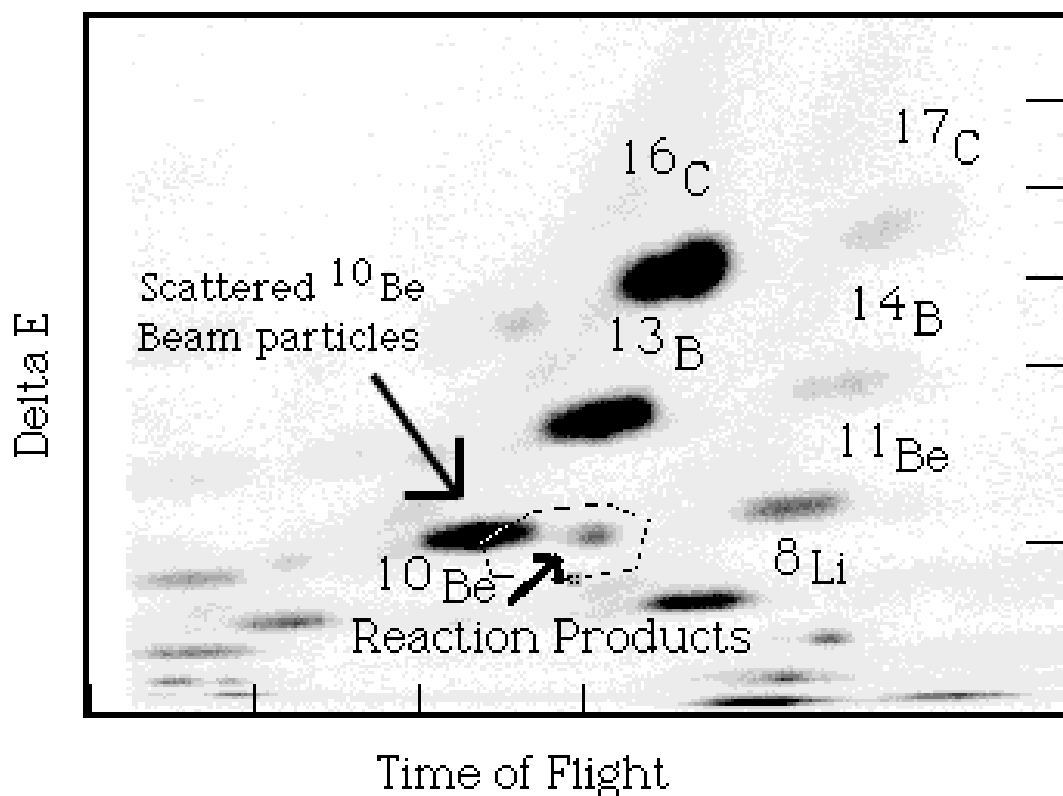


Figure 3.5: The reaction products that reach the focal plane of the A1200 when the Be target is inserted at the Image 2 target position. A 1% momentum aperture was used during the breakup runs. Therefore, the  $^{10}\text{Be}$  fragment group from  $^{11}\text{Be}$  breakup (circled) appears smaller than the  $^{11}\text{Be}$  group in Figure 3.3.

the other six are identified as  $^8\text{Li}$ ,  $^{11}\text{Be}$ ,  $^{13}\text{B}$ ,  $^{14}\text{B}$ ,  $^{16}\text{C}$  and  $^{17}\text{C}$  ions that are scattered in the dipoles and ultimately reach the focal plane.

The scattered beam made it necessary to require conditions other than  $\Delta E$  and ToF. The first conditions were on the vertical PPAC positions, Figure 3.6, to eliminate trajectories that could indicate scattering. The next condition was on a histogram which compares the total energy measured in the stopping scintillator with the flight time through the A1200 (E vs ToF), Figure 3.7.

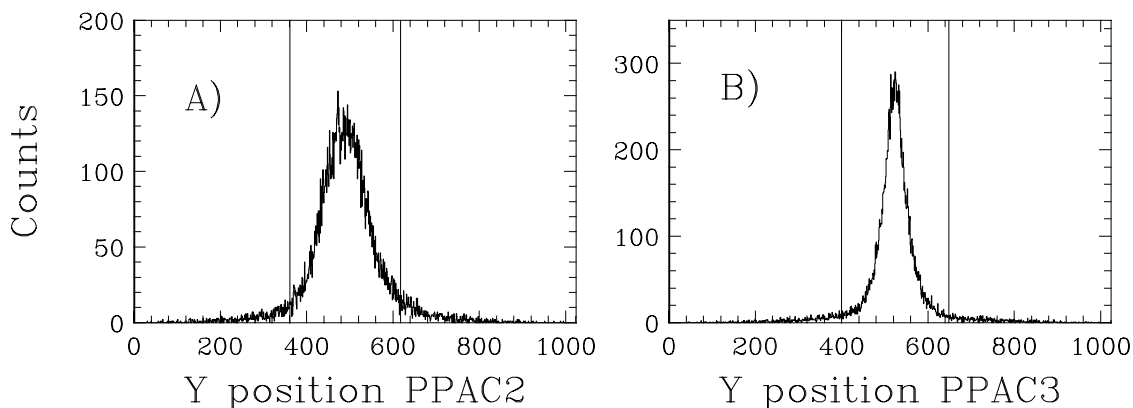


Figure 3.6: Conditions are applied to the position histograms to eliminate trajectories that may indicate beam scattering. The data in these figures are gated on the  $^{10}\text{Be}$  reaction products. We accept only  $^{10}\text{Be}$  fragments that lie within the vertical lines.

The final condition, which was found to be the most selective, was on a histogram which compares the Time of Flight with the horizontal position at the focus (ToF vs X), Figure 3.8. Because the momentum distribution was obtained from the X Focal Plane position, this condition could directly influence the distribution. However, the condition was made loose to avoid these problems. Furthermore, the width of the distribution was not sensitive to small changes in this condition.

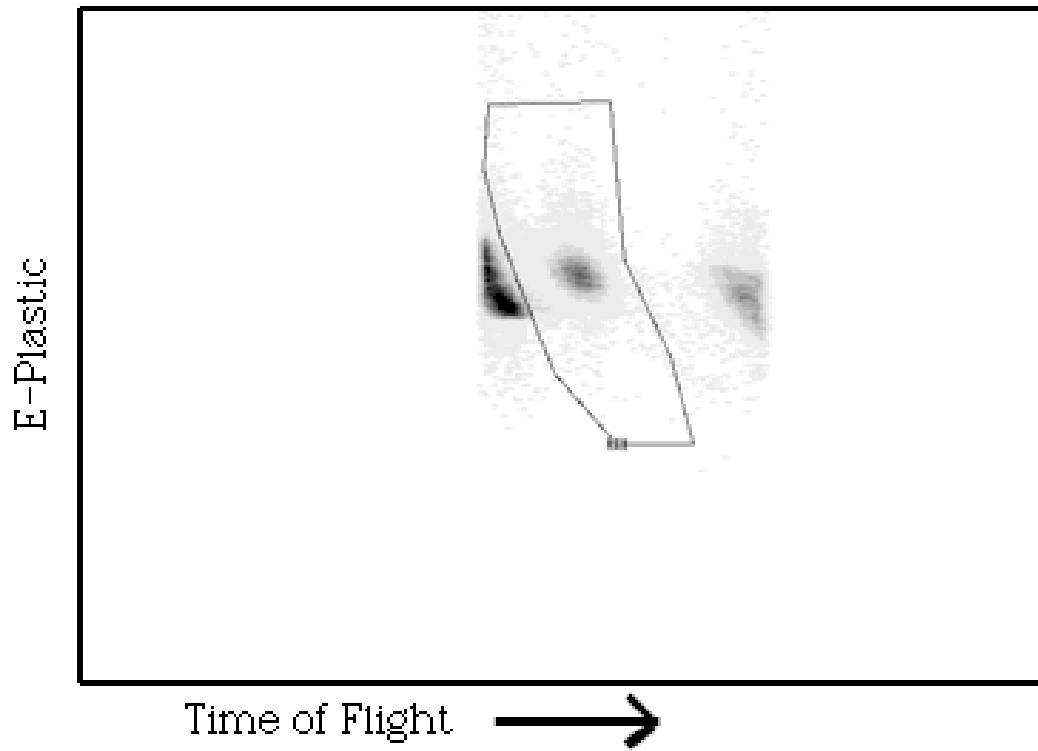


Figure 3.7: The total energy vs. ToF histogram is also used to isolate the  $^{10}\text{Be}$  reaction products. Again, this histogram is gated on the  $^{10}\text{Be}$  reaction products in Figure 3.5.

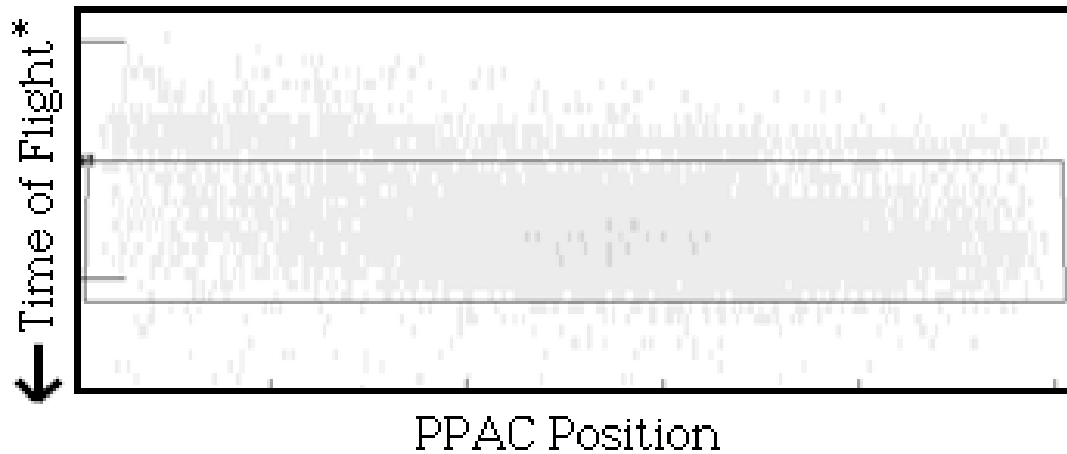


Figure 3.8: The most selective condition is on the Time of Flight\* vs. X focal plane position histogram. Time of Flight\* is a pseudo-parameter, based on the real Time of Flight, that removes the position dependence of the Time of Flight for particles that have different path lengths through the dipoles (related to different radii of curvature).

## Acceptance Limitations for the $^{10}\text{Be}$ Reaction Products

Breakup fragments produced in the Image 2 target are restricted in two ways by the acceptance of the device. The transverse acceptance of breakup fragments is approximately  $\Delta\theta = \pm 20$  mrad and  $\Delta\phi = \pm 10$  mrad. Even with this small acceptance  $^{10}\text{Be}$  breakup events from  $^{11}\text{Be}$  with transverse components as large as 68 MeV/c were accepted by the device. The second restriction is attributed to the longitudinal momentum acceptance of the dipoles which accept only fragments with a momentum of roughly  $\pm 1.5\%$  of the central value.

To measure the longitudinal momentum acceptance of the A1200 dipoles for breakup fragments, a  $^{10}\text{Be}$  beam, produced in the production target at the Target Pot, was transported to Image 2 and the fields in the second half of the A1200 were varied to position the beam at different places on the focal plane. Both the efficiency of transmission from the Image 2 to the Focal Plane and the momentum calibration of the Focal Plane as a function of position (bending radius) were determined from this measurement (Figures 3.9 and 3.10).

## Determination of the Momentum

The momentum of  $^{10}\text{Be}$  fragments is determined based on the simple relation,

$$\mathbf{Force} = q \mathbf{v} \times \mathbf{B} = mv^2/r \hat{\mathbf{r}}. \quad (3.1)$$

In our case, this leads to,

$$mv = p = q B \rho. \quad (3.2)$$

Using the momentum calibration, Figure 3.9, the momentum of  $^{10}\text{Be}$  breakup fragments was related to the bending radius by,

$$p = Z B \rho \times (299.8 \text{ C} \frac{\text{MeV}/c}{\text{Kgm}/s}) \approx 3415 \text{ MeV}/c, \quad (3.3)$$

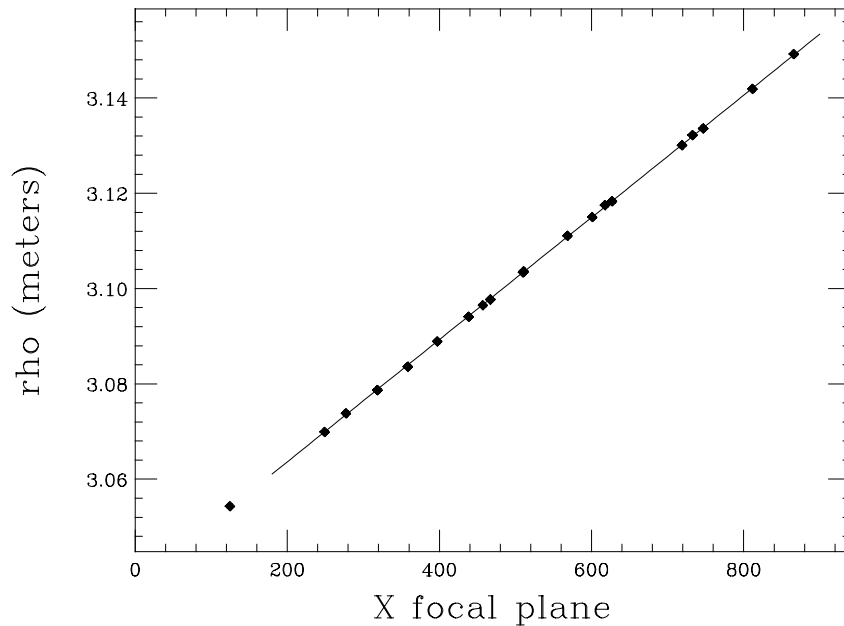


Figure 3.9: The momentum calibration of the A1200 focal plane.

$Z$  is 4 for a fully stripped  $^{10}\text{Be}$  fragment,  $B$  is the dipole magnetic field (roughly 0.917 Tesla), 299.8 is a units conversion factor obtained from

$$299.8 \text{ C} \frac{\text{MeV}/c}{\text{Kg}(\text{m/s})} = 1.602 \times 10^{-19} \text{ Coulomb} \left[ \frac{931.5 \text{ MeV}/(uc^2) \quad 6.022 \times 10^{26} \text{ u/Kg}}{2.9979 \times 10^8 (\text{m/s})/c} \right], \quad (3.4)$$

and  $\rho$  is the radius of curvature in the dipole,

$$\rho = 3.039 + 1.283 \times 10^{-4} X \text{ meters}. \quad (3.5)$$

In this formula  $X$ , the focal plane position measured in the PPAC, varies from 0 to 1024, and the  $\rho_{center}$  value is 3.105 meters.

The  $p_{\parallel}$  distributions required corrections for various experimental effects namely the efficiency of transmission to the focal plane, momentum resolution and energy straggling in the thick production targets.

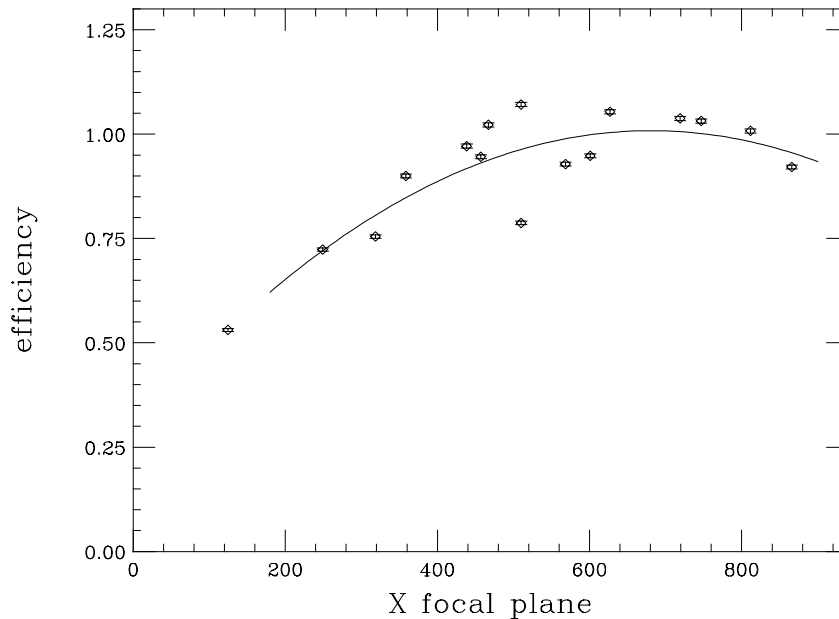


Figure 3.10: The transmission efficiency of the second half of the A1200 vs. position at the focal plane.

### Corrections to the Data for Experimental Effects

The transmission efficiency decreases at the edges of the focal plane and is asymmetric, perhaps because the quadrupole magnet fields were not optimized for transmission. The dipoles accept roughly  $\pm 1.5\%$  of the central momentum. However, only the central  $\pm 1\%$  of the distributions, where the transmission is relatively flat, is shown. The  $^{10}\text{Be}$  fragment distribution from breakup on the Ta target, where the central 5% of the distribution was measured, is discussed later. Figure 3.11 shows the momentum distributions after a correction for the transmission efficiency to the focal plane. To correct for the transmission efficiency the number of counts in a given bin is divided by the transmission efficiency. A quadratic fit to the data in Figure 3.10 is used as the efficiency curve,

$$\epsilon = 0.2048 + 2.105 \times 10^{-3}X - 1.398 \times 10^{-6}X^2. \quad (3.6)$$

The maximum transmission of the linear fit to the data is normalized to 1.0. The uncertainty in the number of counts per bin in the distribution is also divided by the transmission efficiency in order to maintain the same percentage of error in the data.

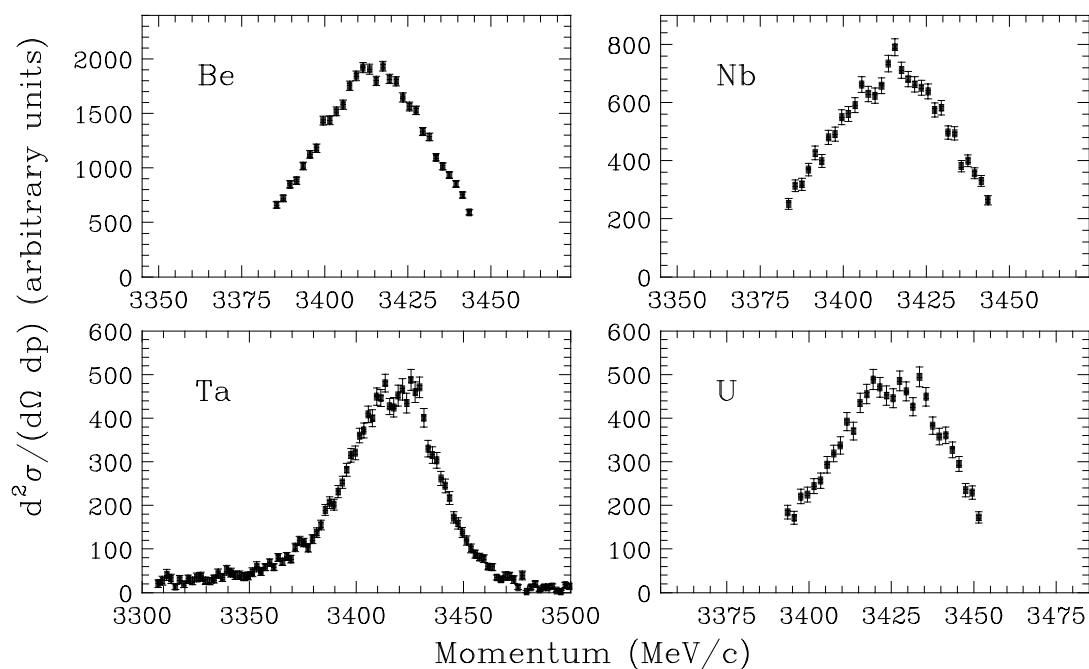


Figure 3.11: The efficiency corrected  $p_{||}$  distributions of  $^{10}\text{Be}$  fragments following the breakup of 63A MeV  $^{11}\text{Be}$  ions.

Momentum resolution and energy straggling effects were determined simultaneously by passing a  $^{10}\text{Be}$  beam through each of the breakup targets and measuring the momentum spread at the focal plane. At the same time a comparison of the change in momentum of the  $^{10}\text{Be}$  beam provided a measure of the energy loss in the targets, which is related to the target thicknesses. The details of the target measurements are in Table 3.2. The resolution functions were taken to be Gaussian in form. The correction for the resolution of the spectrometer and the energy straggling in the thick breakup targets is made by subtracting, in quadrature, the width found in column 3 of Table 3.2 from the widths of the transmission efficiency corrected distributions.

Table 3.2: Target thicknesses and momentum resolutions for the reaction targets.

Target	Target thickness mg/cm <sup>2</sup>	Momentum Resolution MeV/c
<sup>9</sup> Be	191	9.3
<sup>93</sup> Nb	249	11.6
<sup>181</sup> Ta	301	14.7
<sup>238</sup> U	275	13.5

In Appendix E an effect is discussed that indicates the size of the angular acceptance for breakup fragments can influence the width of the observed distribution. The momentum distribution of breakup fragments is not known a priori, and a correction to the data for the influence of the angular acceptance requires this distribution. Therefore, a procedure is developed that filters theoretical predictions of the momentum distribution through the acceptance of the device, which leads to a distribution that can be compared with the data. It appears that the change in width is small (decreased by  $\sim 6\%$ ).

The data is characterized in terms of the full width at half maximum height (FWHM). This avoids the association of the distribution with simple wavefunction shapes that cannot account for the subtle influences of perturbations or other reaction effects that can distort the observed momentum distributions. In order to find the widths of the distributions the maximum height of the distributions was first determined from the average of fits of Gaussian and Lorentzian line shapes to the data. Straight lines were fit to the sides of the distributions, and the width (FWHM) is the distance between the lines at half the maximum height.

Table 3.3: Widths ( $\pm$  uncertainties) of parallel momentum distributions of  $^{10}\text{Be}$  fragments following the breakup of  $^{11}\text{Be}$  on various targets. All widths are FWHM.

Target	Uncorrected [ MeV/c ]	Efficiency Corrected [ MeV/c ]	System Resolution [ MeV/c ]	Resolution Corrected [ MeV/c ]	$^{11}\text{Be}$ Rest Frame [ MeV/c ]
$^9\text{Be}$	44.5(2.0)	45.3(2.0)	9.3(1.0)	44.3(2.3)	41.6(2.1)
$^{93}\text{Nb}$	48.3(1.9)	50.1(1.9)	11.6(1.0)	48.7(2.2)	45.7(2.0)
$^{181}\text{Ta}$	48.2(1.9)	50.3(2.0)	14.7(1.0)	48.1(2.2)	45.2(2.1)
$^{238}\text{U}$	45.8(2.1)	46.3(2.1)	13.5(1.0)	44.3(2.3)	41.6(2.2)

### Transformation into the $^{11}\text{Be}$ Rest Frame

The final procedure is to transform the distribution into the  $^{11}\text{Be}$  rest frame which reduces the width by the relativistic factor  $\gamma = \sqrt{1/(1 - \beta^2)}$ , roughly 5%. Corrections to the widths and the transformation are detailed in Table 3.3.

### 3.1.3 Discussion of the $^{10}\text{Be}$ $P_{\parallel}$ Distributions

The results for the Be, Nb and U targets show the central 2% of the measured momentum distributions. However, three different spectrometer magnetic field settings were used to measure the central 5% of the distribution from the Ta target. The data from each setting with the Ta target are normalized by the beam current measured in the beam monitor Si PIN diodes, and the final distribution is obtained by adding the three data sets together and properly taking into account the overlap of the settings. The distribution on the Ta target does not show any indication of a two component structure as has been suggested by earlier measurements of the transverse momentum distribution of  $^{10}\text{Be}$  cores from the breakup of  $^{11}\text{Be}$  [Kob89].

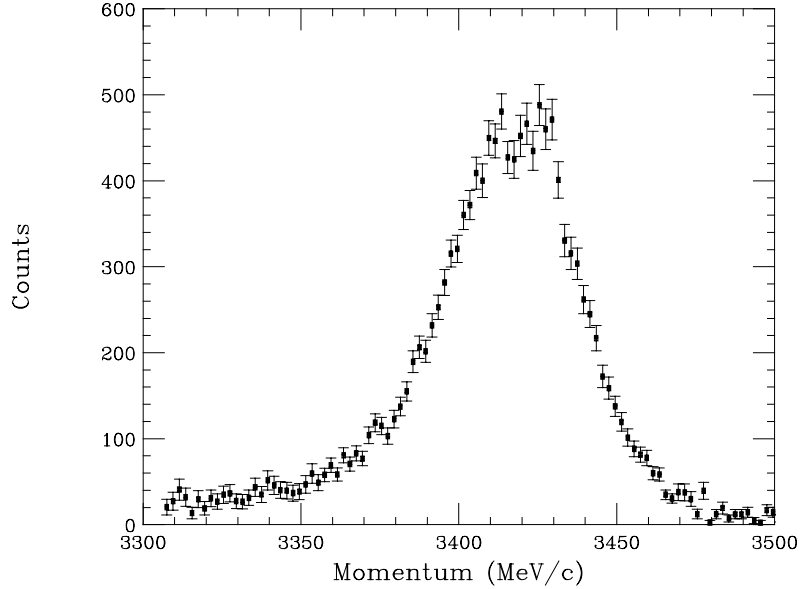


Figure 3.12: The  $p_{||}$  distribution of  $^{10}\text{Be}$  fragments following breakup in the Ta target. The background is low, and the asymmetry hints that a dissipative tail may be present on the low momentum side.

### $^{10}\text{Be}$ from Contaminants in the RNB

It is possible that  $^{10}\text{Be}$  fragments could be produced by nuclei in the RNB other than  $^{11}\text{Be}$ . For example, as can be seen in Figure 3.3, the nuclei  $^{14}\text{B}$  and  $^{16}\text{C}$  have a similar velocity to that of  $^{11}\text{Be}$ . Therefore, these nuclei could also produce  $^{10}\text{Be}$  fragments that would arrive at the focal plane with a ToF similar to that of the  $^{10}\text{Be}$  fragments produced by  $^{11}\text{Be}$  breakup events. It is possible to determine the centroid of the  $^{10}\text{Be}$  fragment momentum distribution from contaminants, and using the Goldhaber model, Section C.1, the widths of the distributions produced from these contaminants; see Table 3.4.

The momentum distribution measured for breakup in the Ta target has a narrow width with a relatively flat background. The contaminant nuclei produce broad  $^{10}\text{Be}$  fragment distributions that are peaked at momenta quite different from the peak in

Table 3.4: The expected mean momentum and widths of  $^{10}\text{Be}$  fragment momentum distributions from nuclei in the RNB that could produce  $^{10}\text{Be}$  fragments. Predicted widths, FWHM, are from the Goldhaber model with  $\sigma_o=80$  MeV/c, Section C.1.

Isotope	Centroid MeV/c	Width MeV/c
$^{13}\text{B}$	3616	297
$^{14}\text{B}$	3341	330
$^{15}\text{C}$	3760	355
$^{16}\text{C}$	3511	376
$^{17}\text{C}$	3289	393

the observed distribution. This indicates that breakup reactions from the contaminants do not significantly contribute to the observed distribution. There is a slight asymmetry on the low momentum side of the distribution that may originate from the  $^{14}\text{B}$  contaminant which would produce  $^{10}\text{Be}$  fragments peaked at 3341 MeV/c. However, it is also possible that this asymmetry is rooted in dissipative reaction processes that produce low momentum tails in the fragmentation of nuclei in this energy range [Sou92].

The transverse acceptance for breakup fragments plays a significant role for determining the transmission of a distribution with a given width. The one-neutron breakup of  $^{11}\text{Be}$  has a very large cross section and produces  $^{10}\text{Be}$  fragments with a very narrow momentum distribution width ( $\sim 43$  MeV/c); thus the bulk of this distribution is transmitted. On the other hand, the contaminants will have a relatively small cross section for producing  $^{10}\text{Be}$  fragments, and the associated  $^{10}\text{Be}$  fragment distribution widths are quite large. Thus very few  $^{10}\text{Be}$  fragments produced by contaminants will reach the Focal Plane. For these reasons  $^{10}\text{Be}$  fragments from the breakup of  $^{11}\text{Be}$  dominate the distributions we observe.

### Distribution Widths Independent of the Reaction Mechanism

The Be, Nb, Ta and U breakup targets provide the opportunity to investigate the effects of the different reaction mechanisms. While breakup in the Be target is dominated by nuclear mechanisms (approximately 6% Coulomb [Ann94]), breakup in the U target is essentially all from Coulomb mechanisms [Ann94], and the breakup in the Nb and Ta targets is induced by a mixture of nuclear and Coulomb mechanisms. It appears that the width of the parallel momentum distributions is not strongly related to the target mass indicating that the widths of the momentum distributions are not sensitive to the reaction mechanism.

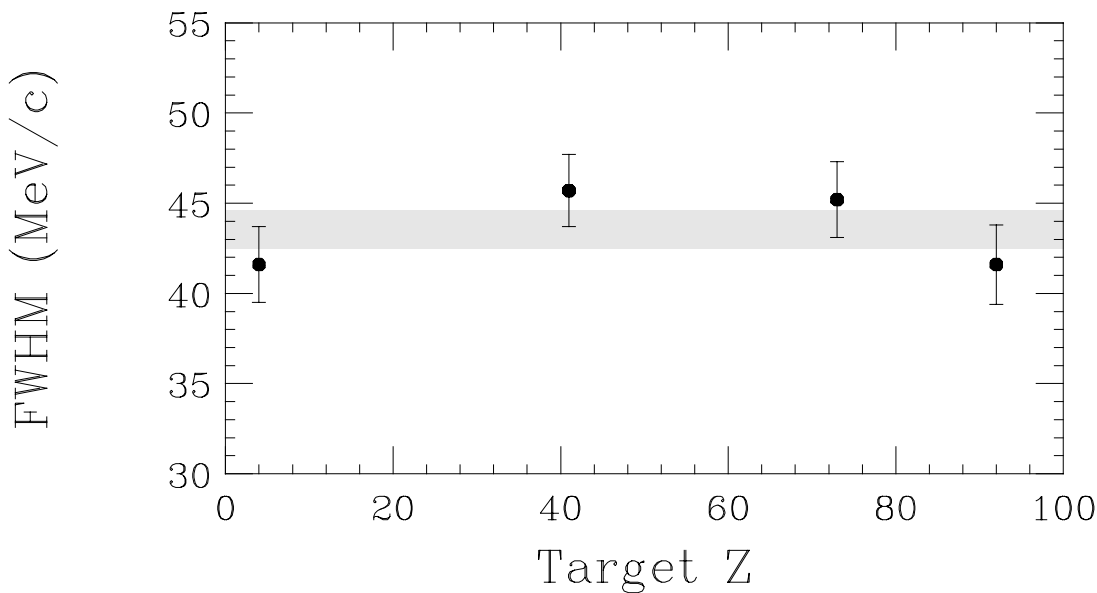


Figure 3.13: The corrected widths of the  $^{10}\text{Be}$  momentum distributions in the  $^{11}\text{Be}$  rest frame. The widths are in agreement, showing no systematic dependence on the target. The weighted average (shaded region) is  $43.6 \pm 1.1$  MeV/c.

### Prediction for the $2s_{1/2}$ Neutron Momentum Wavefunction

The momentum wavefunction of the halo neutron in  $^{11}\text{Be}$  is obtained by assuming a  $2s_{1/2}$  neutron bound in a Woods-Saxon potential with the parameters adjusted to reproduce the binding energy and the rms radius of the  $^{10}\text{Be}$  core. The parallel

momentum distribution is the projection of this spherically symmetric momentum density distribution ( $|\Psi^*\Psi|$ ) onto one axis [Esb94]. In the spirit of the Serber model we compare this prediction with the data for all breakup targets, and the prediction is transformed into the laboratory frame and convoluted with the momentum resolution of the spectrometer and the energy straggling in the targets.

A final step is to correct the shape of the distribution for a change that occurs due to the limited transverse acceptance (discussed in Appendix E). The changes in shape arise when a non-Gaussian distribution passes through a limited transverse acceptance. An approximate method was used to estimate the effect of the limited acceptance and the changes are small. The width of the prediction is reduced from 45.4 MeV/c to 43.7 MeV/c (6%).

The momentum distribution obtained from the projection of the  $2s_{1/2}$  neutron wavefunction onto the parallel momentum axis is in good agreement with the distributions from all of the targets, Figure 3.14. However, this method does not take into account any reaction mechanism effects and is a reasonable approximation for breakup on a light target where stripping dominates.

On the heavy target, where Coulomb dissociation is the dominant breakup mechanism, subtle changes to the distribution could occur. For example, at this energy the momentum distribution from a dipole excitation calculation [Esb94] is slightly narrower (39.8 MeV/c) than the width of the momentum distribution of the  $2s_{1/2}$  neutron wavefunction (45.4 MeV/c), Figure 3.15. This is likely because of complex dynamical factors in the dipole excitation process. Our data does not show a systematic change in the momentum distribution width with increasing target mass. Therefore, we choose to neglect these reaction mechanism effects and compare all data with the wavefunction of the halo neutron.

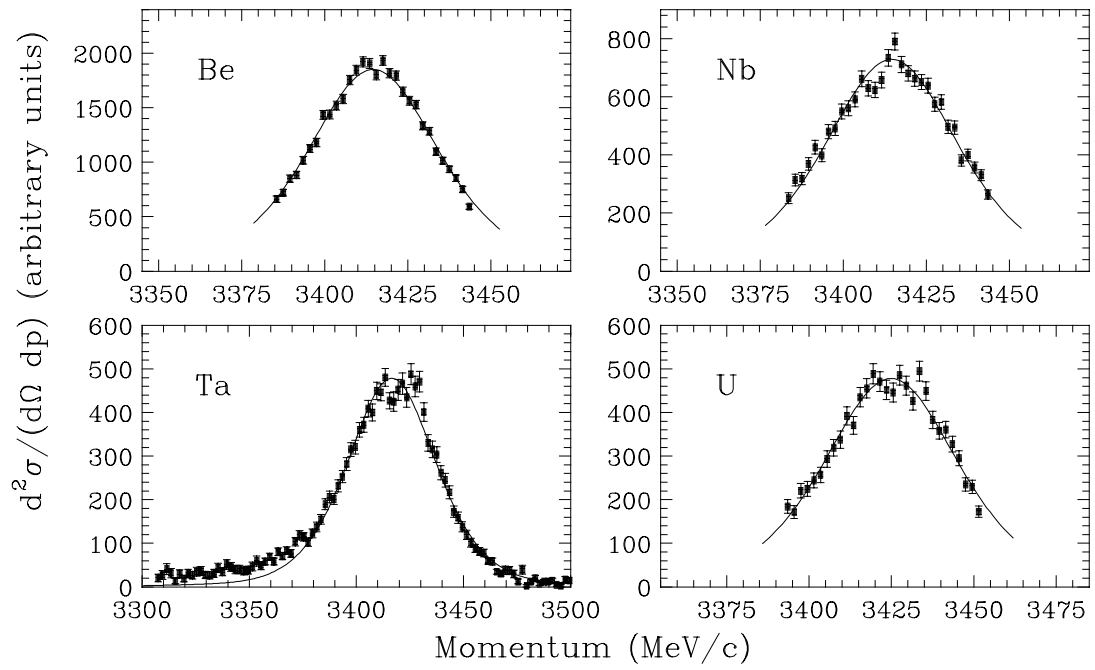


Figure 3.14: The  $p_{\parallel}$  distributions of  $^{10}\text{Be}$  core fragments compared with the a projection of the wavefunction of a  $2s_{1/2}$  neutron, bound in a Woods-Saxon potential by 500 keV, onto the  $p_{\parallel}$  axis [Esb94].

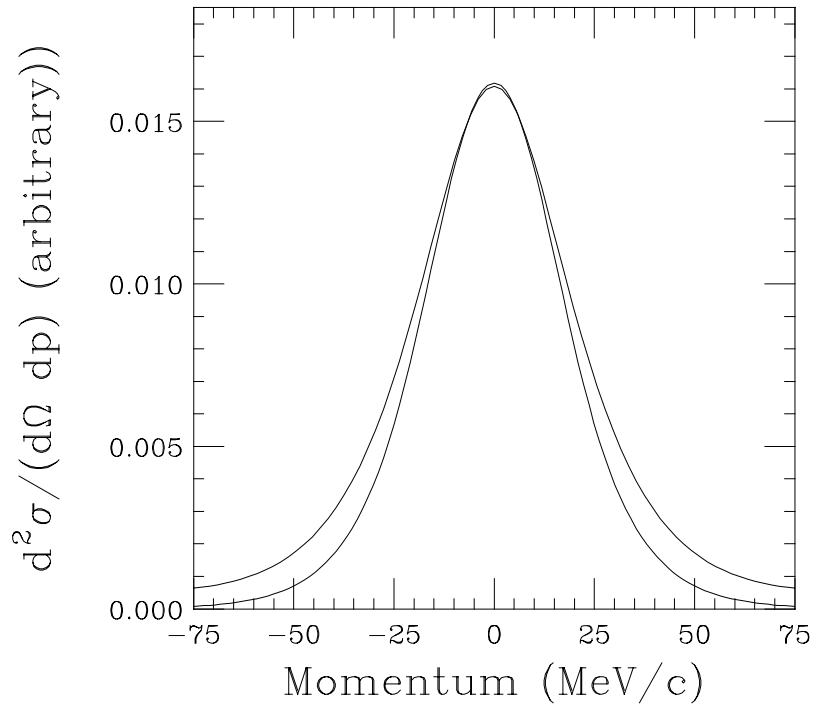


Figure 3.15: [Esb94] The width of the  $p_{\parallel}$  distribution of the  $2s_{1/2}$  neutron is slightly broader than a perturbation theory prediction of the  $^{10}\text{Be}$   $p_{\parallel}$  distribution expected from dipole excitation of  $^{11}\text{Be}$ .

## $P_{\parallel}$ Distribution to Determine Ground State

The  $p_{\parallel}$  distribution is sufficient to establish that the valence neutron is in the  $2s_{1/2}$  orbital rather than the  $1p_{3/2}$  orbital. Figure 3.16 shows the  $p_{\parallel}$  distributions that correspond to these orbitals [Bro95a] and the data from the Be target. The data are transformed into the  $^{11}\text{Be}$  rest frame, and agree with the  $2s_{1/2}$  wavefunction. To account for the influence of the acceptance, Appendix E, the corrected theoretical distribution for the  $2s_{1/2}$  orbital was obtained. The data were scaled by the difference between the corrected and the uncorrected distributions, point by point, to account for the small difference in transmission.

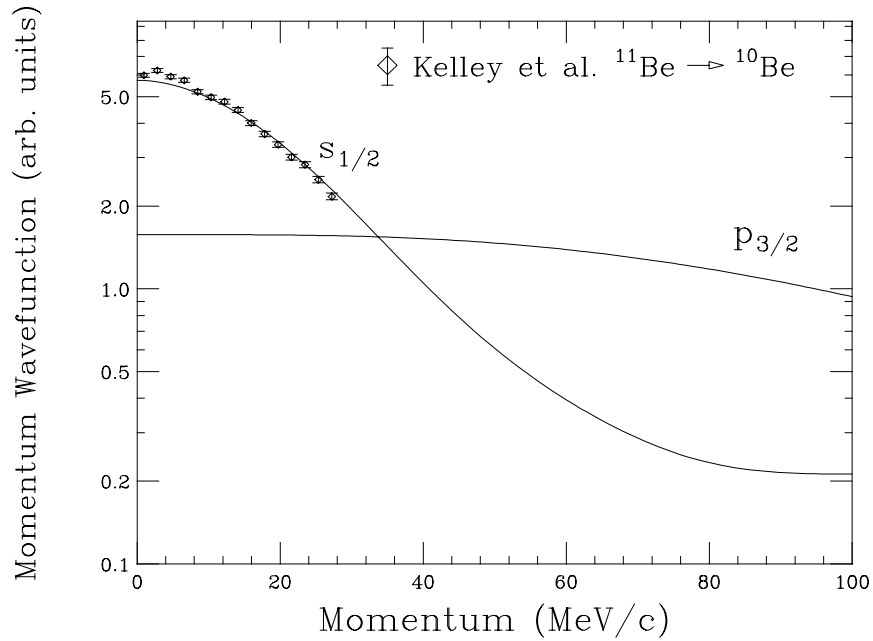


Figure 3.16: The  $p_{\parallel}$  distribution sufficient to show that the  $2s_{1/2}$  intruder state dominates the valence neutron wavefunction. The momentum wavefunctions are from [Bro95a].

## 3.2 Comparison with the Transverse Momentum Distributions of Fragments from $^{11}\text{Be}$ Breakup

### 3.2.1 $P_{\perp}$ Distribution of Core Fragments

The transverse momentum distribution of  $^{10}\text{Be}$  fragments from the breakup of 790A MeV  $^{11}\text{Be}$  [Kob89] was measured and was fit with a two-component Gaussian distribution, Figure 3.17. As with  $^{11}\text{Li}$ , the broad component, 257 MeV/c FWHM, was associated with the removal of core neutrons, and the narrow component, 59 MeV/c FWHM, was associated with the removal of the more peripheral halo neutrons. Because diffraction and other reaction mechanism effects influence  $p_{\perp}$ , this distribution is not expected to reflect the momentum wavefunction of the halo neutron as accurately as the  $p_{\parallel}$  distributions.

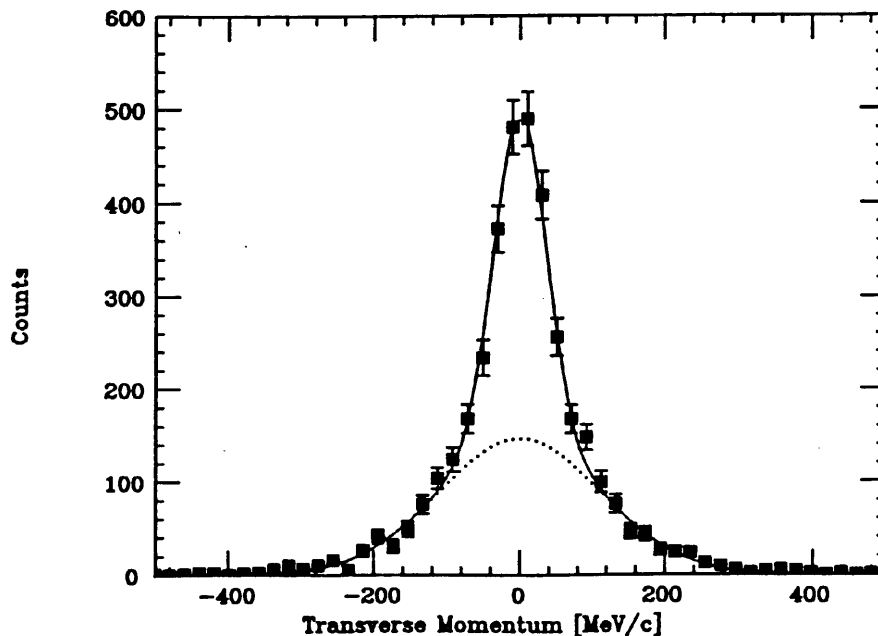


Figure 3.17: [Kob89] The transverse momentum distribution of  $^{10}\text{Be}$  cores following the breakup of 790A MeV  $^{11}\text{Be}$ .

### 3.2.2 Angular Distribution of Neutrons

The angular distribution of neutrons following the breakup of  $41\text{A } ^{11}\text{Be}$  was measured by [Ann93, Ann94] in an attempt to isolate and study the different reaction mechanisms. The neutrons were detected in an array that covered the lab angles from  $0^\circ$  to  $97^\circ$  while a  $\Delta E$ - $E$  detector telescope at  $0^\circ$  measured the charged fragments. With gross assumptions about the reaction mechanisms, this information made it possible to separate the data into two categories.

The first category, exclusive reactions, includes breakups with both a fast neutron and a  $^{10}\text{Be}$  core in the final state. These reactions are assumed to result from dissociation reactions, Section 2.3. On a heavy target the reactions are from Coulomb dissociation while on a light target diffraction dissociation is the breakup mechanism.

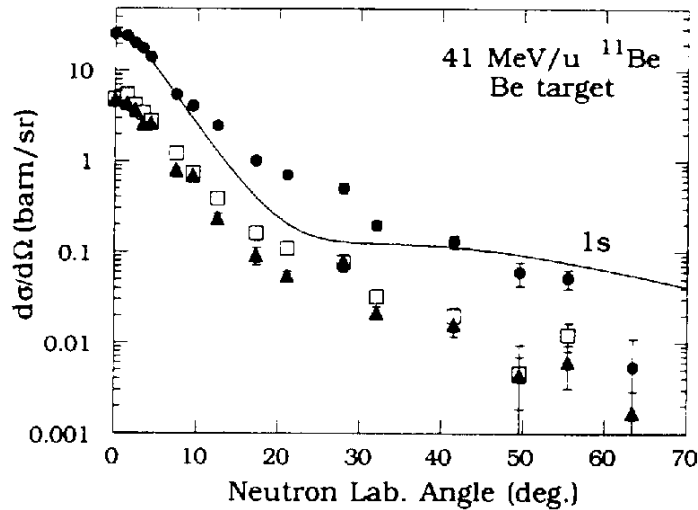


Figure 3.18: [Ann94] The angular distribution of neutrons following the breakup of  $41\text{A MeV } ^{11}\text{Be}$  is in agreement with a prediction based on a  $2s$ -orbital neutron ( $1s$  in some notation) in a simple square-well potential. A narrow width ( $\Gamma=60 \text{ MeV}/c$ ) is extracted from the restricted inclusive data (circles,  $n + \text{no } ^{10}\text{Be}$ ). Also shown are the distributions for  $n + \text{He}$  (triangles) and  $n + \text{Li}$  (squares).

The second category was termed restricted inclusive and includes events with a

neutron detected in coincidence with any fragment other than a  $^{10}\text{Be}$  core, Figure 3.18. These events are assumed to result from stripping reactions in which the core collides with a target nucleus and is broken apart. This type of reaction is claimed to leave the motion of the halo neutron mostly undisturbed so that the resulting angular distribution should reflect the initial state wavefunction.

It was apparent, from the restricted inclusive events, that the neutron distributions from violent core-target collisions contain information about the halo wavefunction. A Lorentzian width parameter  $\Gamma=60$  MeV/c was extracted from the data and is consistent with the simple interpretation of [Han87] where  $\Gamma = \sqrt{8\mu S_n} = 58$  MeV/c. The differential cross sections derived from the data were found to be in good qualitative and quantitative agreement with the predictions for the various breakup reaction categories.

A discrepancy arises, however. A Lorentzian width parameter of  $\Gamma=60$  MeV/c is inferred from the angular distributions of neutrons from  $^{11}\text{Be}$  [Ann93, Ann94] while a width of 43.6 MeV/c (average of the four targets) is obtained from the present work. The difference in the width of the parallel momentum distribution of core fragments and the width derived from the angular distribution of neutrons may arise from differences in the effects of the reaction mechanism (and in initial and final state reactions) on the parallel momentum of core fragments and the transverse momentum of halo fragments. In contrast to the case for angular distributions where a particular line-shape must be assumed to interpret the data, a distribution width can be measured directly from the parallel momentum distribution. Furthermore, a Lorentzian distribution shape results from the assumption that the  $^{10}\text{Be}$  core provides a square-well potential, and that outside the core the valence neutron wavefunction falls off as a Yukawa. More realistic potential shapes, for example a Woods-Saxon, should be used for comparison with the data.

### 3.3 Neutron Halo Radius

The agreement between the data and the calculation of Esbensen [Esb94], using a Woods-Saxon potential, supports the use of the rms radius, 7.2 fm, to determine the neutron halo radius in  $^{11}\text{Be}$ . This is the rms radius for the relative motion of the neutron and the core. In the  $^{11}\text{Be}$  rest frame the halo neutron rms radius is 6.5 fm ( $7.2 \times 10/11$ ) and is consistent with the value  $6.4 \pm 0.7$  fm that is required to reproduce the E1 strength observed in the Coulomb breakup of  $^{11}\text{Be}$  [Nak94] (and Section B.6).

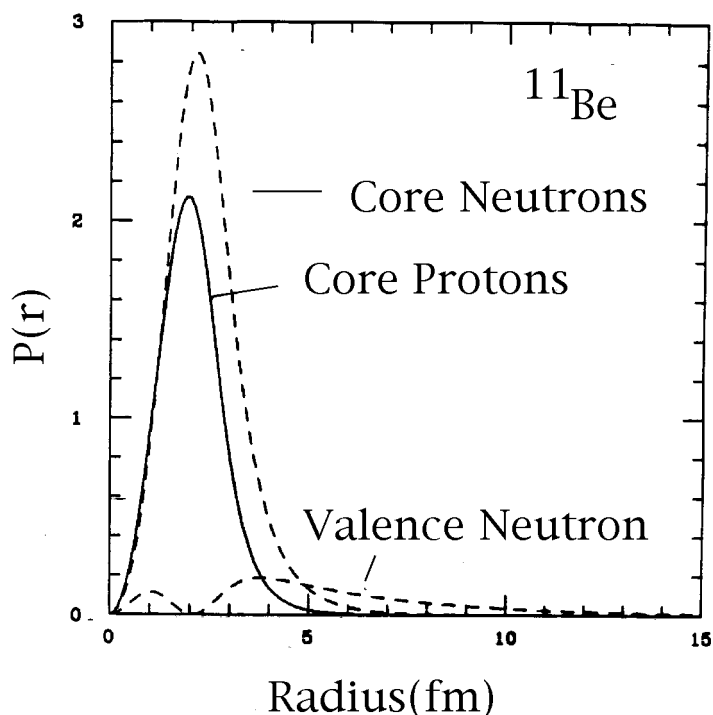


Figure 3.19: [Bro95] The probability distribution of nucleons in  $^{11}\text{Be}$ .

By comparing the probability distribution of nucleons in the  $^{10}\text{Be}$  core with the distribution of the valence  $2s_{1/2}$  neutron [Bro95a], which has a node near 2 fm, the extent of the neutron halo is plainly seen. All measurements to date on the nucleus  $^{11}\text{Be}$  are consistent with the presence of a prominent neutron halo, and the present result finds excellent agreement with the wavefunction of the halo neutron.



# Chapter 4

## Search for a Proton Halo in ${}^8\text{B}$

The discovery of neutron halos in weakly bound neutron rich nuclei such as  ${}^{11}\text{Li}$  and  ${}^{11}\text{Be}$  raises the issue of the possible existence of proton halos in proton rich nuclei. It had been argued that a loosely bound proton would be localized by the Coulomb barrier, hindering the formation of a halo [Han93]. The valence proton in  ${}^8\text{B}$  is less tightly bound than the neutrons in  ${}^{11}\text{Li}$  and  ${}^{11}\text{Be}$ . However, the Coulomb barrier and the angular momentum barrier for the p-orbital proton increase the effective barrier height and decrease the extent of the proton wavefunction. The issue has been resurrected by recent measurements and theoretical models that suggest  ${}^8\text{B}$ , bound by only 137 keV, may possess a proton halo. The present experimental situation is unclear since the interpretations of experimental results are not in agreement on this issue. The earliest evidence of a proton halo was in 1992, but there are only a few measurements to date that would be sensitive to a halo in  ${}^8\text{B}$ .

### 4.1 Experimental Measurements of the Nuclear Size of ${}^8\text{B}$

The interaction cross section measurements of light nuclei at 790A MeV that found evidence for neutron halos [Tan85a, Tan85b, Tan88] showed no enhancement in the

$^8\text{B}$  reaction cross section. The rms radii obtained for the boron isotopes indicate that the nuclear size does not change significantly in the range from  $^8\text{B}$  through  $^{15}\text{B}$ . It is interesting in this case to compare the difference between the rms radii of the proton and neutron density distributions; Figure 4.1 shows that the proton density distribution in  $^8\text{B}$  does extend beyond the neutron density distribution.

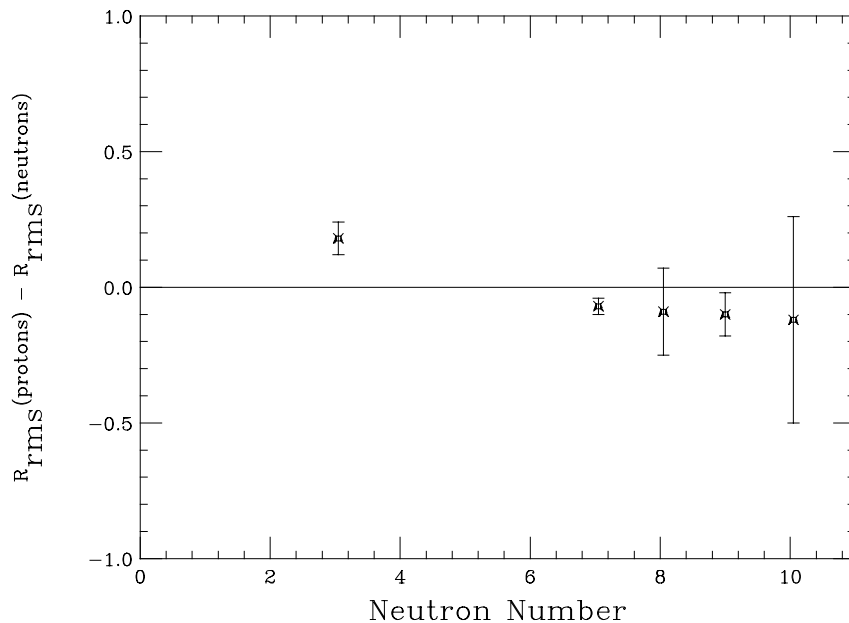


Figure 4.1: The difference between the rms radii of the proton and neutron density distributions in the boron isotopes, obtained from the 790A MeV cross section data. Data from [Tan88].

The 790A MeV reaction cross section data [Tan88] indicates that the rms radius of the valence proton, obtained from Equation 1.4 and the radii of  $^8\text{B}$  ( $2.38 \pm 0.04$  fm) and  $^7\text{Be}$  ( $2.31 \pm 0.02$  fm), is only 3.02 fm. This value is much smaller than the rms radius of the neutron halo in  $^{11}\text{Be}$  (6.5 fm), and appears to indicate that the nuclear distributions in  $^8\text{B}$  are similar to those of normal nuclei.

A recent measurement of quasielastic scattering of 40A MeV  $^8\text{B}$  on a  $^{12}\text{C}$  target [Pec95] found that the small angle cross section was not easily reproduced in a coupled-channels calculation and probably reflects the loose binding of the valence

proton. However, the proton removal cross section was also measured and showed no significant enhancement of the breakup cross section.

The first evidence of a proton halo came from a measurement of the quadrupole moment of  ${}^8\text{B}$  ( $68.3 \pm 2.1$  mb); it was found to be much larger than that of the mirror nucleus  ${}^8\text{Li}$  ( $32.7 \pm 0.6$  mb) [Min92]. The observed value was reproduced using shell model wavefunctions generated in Woods-Saxon potentials. The rms radius of the five protons in this model was considerably larger, 2.99 fm, than the rms radius of the three neutrons, 2.20 fm, and was taken as an indication of a prominent proton halo in  ${}^8\text{B}$ . However, these results do not necessarily provide definitive evidence of a proton halo. For example, the quadrupole moment may be enhanced by contributions from a deformed  ${}^7\text{Be}$  core [Rii93b, Cso93].

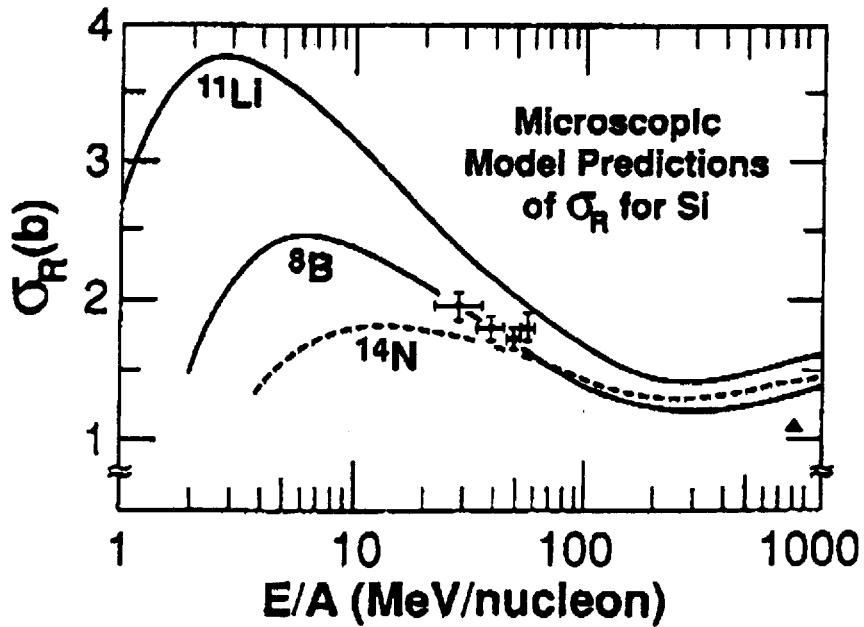


Figure 4.2: [War95] The breakup cross section of  ${}^8\text{B}$  compared with a microscopic calculation that shows the trend expected if  ${}^8\text{B}$  has a proton halo. Also shown are calculations for the two neutron halo nucleus  ${}^{11}\text{Li}$  and the normal sized nucleus  ${}^{14}\text{N}$ .

Finally, the  ${}^8\text{B}$  cross section in active targets was recently measured at the NSCL. A stack of silicon  $\Delta E$  detectors measured reaction rates in the range between 20A and

60A MeV [War95]. The increase of the nucleon-nucleon cross section at low energies leads one to expect that, if present in  ${}^8\text{B}$ , halo effects should dominate breakups. A comparison of the data with a microscopic calculation which assumes a proton halo indicates that the observations are consistent with an extended proton distribution. The cross section data are shown in Figure 4.2 with the microscopic calculation showing the expected enhancement from the halo that would dominate at lower energies.

## 4.2 The $P_{\parallel}$ and $P_{\perp}$ Momentum Distributions of ${}^7\text{Be}$ Fragments Following the Breakup of ${}^8\text{B}$

In an attempt to understand the existing discrepancies, we have approached the problem from an independent direction by simultaneously measuring the  $p_{\parallel}$  and  $p_{\perp}$  distributions of  ${}^7\text{Be}$  fragments produced in the breakup of  ${}^8\text{B}$  on  ${}^9\text{Be}$ ,  ${}^{93}\text{Nb}$  and  ${}^{197}\text{Au}$  targets. The  $p_{\parallel}$  distributions of  ${}^{10}\text{Be}$  fragments following the breakup of  ${}^{11}\text{Be}$  ions indicated that the breakup reactions accurately probed the wavefunction of the halo neutron. Therefore, it was expected that the  ${}^8\text{B}$  breakup data could also be understood by a direct comparison with the momentum wavefunction of the valence proton.

Narrow distribution widths are observed ( $\sim 75$  MeV/c). However, as will be discussed later, the reaction mechanisms appear to strongly influence the observed distributions. Thus, it seems premature to conclude that  ${}^8\text{B}$  has a halo. None the less, realistic predictions of the core fragment momentum distributions, based on the wavefunction of a proton bound by 137 keV in a p-orbital Woods-Saxon potential, include reaction mechanism effects and are found to agree with the data. The rms radius of the theoretical wavefunction is 4.24 fm and indicates that the valence proton has a much larger radial extent than the  ${}^7\text{Be}$  core (2.31 fm [Tan88]).

### 4.2.1 Experimental Details

To obtain a high quality relatively pure  $^8\text{B}$  beam both isotope separation devices at the NSCL, the A1200 fragment separator and the RPMS Wien-filter, were used to remove contaminants from the  $^8\text{B}$  beam. A beam of 60A MeV  $^{16}\text{O}$  ions, from the K1200 cyclotron, was fragmented in a thick Be production target. Products passed through the A1200 fragment separator, with an Al absorber (wedge) placed at the second dispersive image. Isotopes reaching the focal plane were dispersed because of differential energy losses in the wedge, and a moveable aperture at the focus eliminated most contaminants. The resulting beam consisted of the N=3 isotones, with a large 34.3A MeV  $^7\text{Be}$  component ( $^8\text{B}:\text{}^7\text{Be}=1:20$ ).

This beam then passed through the RPMS Wien-filter which separated the isotones, leaving a 95% pure 41.2A MeV beam of 300  $^8\text{B}$  particles per second at the breakup target. The  $^8\text{B}$  beam momentum spread was limited to  $\pm 0.25\%$  by the aperture located at the first dispersive image of the A1200, and the relative velocity of ions reaching the breakup target was determined by their time-of-flight over a 40 meter flight path between a thin plastic scintillator and the particle detector telescopes. This insured that the detected  $^7\text{Be}$  particles came from reactions of 41.2A MeV  $^8\text{B}$  in the target, instead of the 34.3A MeV  $^7\text{Be}$  component of the incoming beam.

After the RPMS, a pair of two-dimensional position sensitive Parallel Plate Avalanche Counters (PPACs) located upstream of the target permitted a reconstruction of the incoming particle trajectories. Downstream of the target position, breakup products were detected in two 5 cm by 5 cm  $\Delta\text{E}-\Delta\text{E}-\text{E}$  telescopes. The first  $\Delta\text{E}$  detector was a position sensitive Si detector that was segmented into 16 vertical strips and 16 horizontal strips. This corresponds to a strip spacing of 3.125 mm. The second was a Si PIN-diode, and the E signal was provided by a stopping CsI detector. Tele-

Table 4.1: Description of detectors that comprise the two telescopes, and the energy loss of a 40A MeV  $^7\text{Be}$  ion (provided for reference). Note that in the telescopes the order of the detectors was Strip Detector, PIN-diode and the stopping CsI detector.

Detector	Thickness ( $\mu\text{m}$ )	Thickness ( $\text{mg}/\text{cm}^2$ )	$^7\text{Be}$ E-loss (MeV)
Telescope 1			
Strip Detector	502	117.0	22.8
PIN-diode	504	117.4	22.9
Telescope 2			
Strip Detector	304	70.8	13.6
PIN-diode	518	120.7	23.5

scope 1 was 60 cm from the target and covered angles  $\theta=3.3^\circ$  to  $-1.4^\circ$  (horizontal) and  $\phi = \pm 2.4^\circ$  (vertical). The second was 50 cm away from the target and covered the angles  $\theta = -2.6^\circ$  to  $-8.3^\circ$  and  $\phi = \pm 2.9^\circ$ .

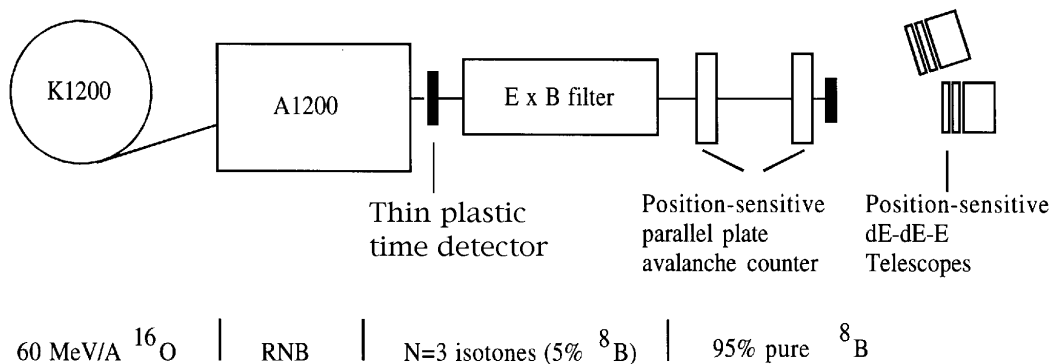


Figure 4.3: A schematic illustration showing the overall layout of experimental apparatus used in the  $^8\text{B}$  breakup experiment.

The target thicknesses were chosen to make the  $p_{\parallel}$  momentum distribution broadening effects, caused by the differential energy loss of  $^7\text{Be}$  and  $^8\text{B}$ , similar to the momentum resolution. The average size of this effect is approximately 10 MeV/c. This is insignificant when subtracted in quadrature from the measured fragment distribution widths.

Table 4.2: Target thicknesses in the  $^8\text{B}$  breakup experiment.

Target	Target thickness (mg/cm <sup>2</sup> )
$^9\text{Be}$	47
$^{93}\text{Nb}$	85
$^{238}\text{U}$	97

### 4.3 Analysis of the Data

The  $^7\text{Be}$  reaction products detected in the telescopes were selected using  $\Delta E$  vs.  $E$  signals. Because channeling, an effect related to the crystal structure of the silicon, occurred in the Si PIN-diodes it was also necessary to consider the energy signal from the position sensitive Si strip detectors. The  $^7\text{Be}$  ions were easily identified using redundant  $\Delta E$ - $E$  selections. The relative flight time of incoming ions was used to identify  $^8\text{B}$  projectiles that impinged on the target, and the final condition was applied to the PPAC located immediately in front of the target and defined the beam spot on the target (5 mm by 7 mm FWHM). With these requirements it was possible to cleanly identify  $^7\text{Be}$  fragments following the breakup of  $^8\text{B}$ , Figure 4.4.

#### Angular Deflection Calibration

The angular deflection of breakup fragments was determined from the measured position in each of the position sensitive detectors. Incoming trajectories were obtained from the two PPACs which were separated by 1.22 meters. Using this trajectory, the position on the target was extrapolated. The separation of the final PPAC and the target was 2.5 cm. After the target, the scattering trajectory was determined from the position on the target and the position in the strip detector. The angular resolution, 10 mrad, was obtained from a target out run where there was no deflection.

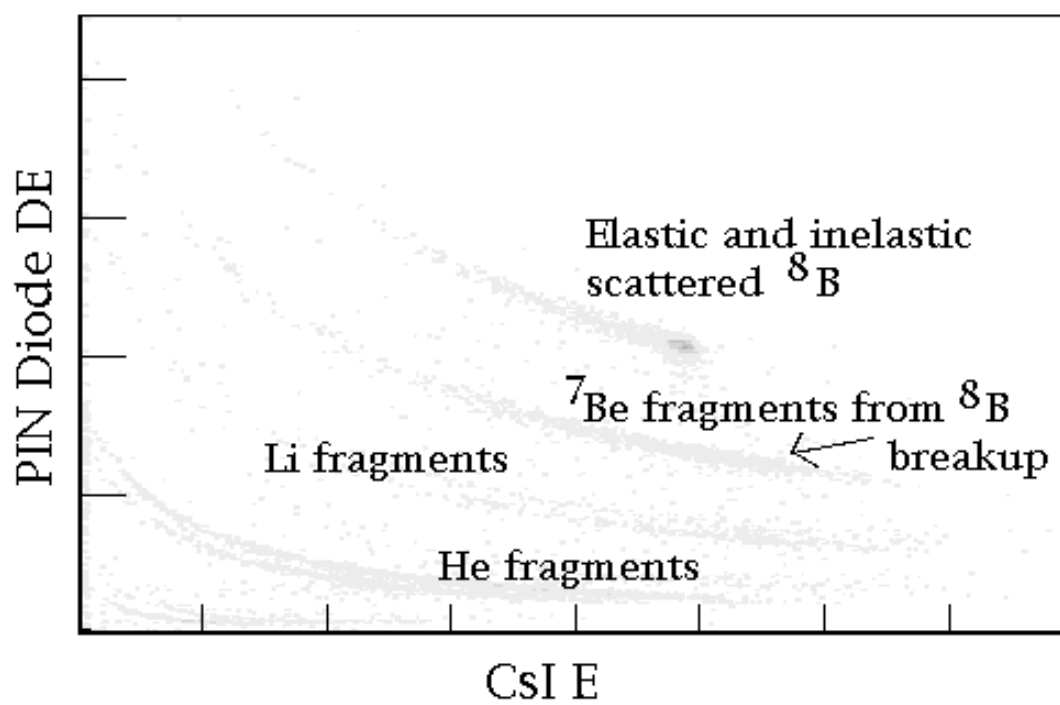


Figure 4.4:  $\Delta E$  vs  $E$  showing the  $^7\text{Be}$  fragments from  $^8\text{B}$  breakup measured in Telescope 2. Li, and He fragments from  $^8\text{B}$  breakup are also identified.

## Momentum Calibration

An energy calibration was obtained using  ${}^7\text{Be}$  beams at six different energies. These beams were produced with two A1200 magnetic rigidities that provided  ${}^7\text{Be}$  at energies of 51.47A MeV and 41.41A MeV. Two aluminum targets, 190 mg/cm<sup>2</sup> and 398 mg/cm<sup>2</sup>, located in a target ladder degraded these beams so that  ${}^7\text{Be}$  beam energies of 51.5A MeV, 47.3A MeV, 42.3A MeV, 41.4A MeV, 36.3A MeV and 30.1A MeV were obtained. A position dependent response in the CsI detectors required that these detectors be sectioned into 256 sub-detectors using the position sensitive detectors. The total momentum was determined from the sum of the energies measured in the telescope. The overall momentum calibration of each telescope indicated that at 2000 MeV/c the resolution,  $\Delta p/p$ , was better than 0.5%. The measured deflection angle was used to determine the  $p_{\parallel}$ .

### 4.3.1 The $P_x$ Distributions

The  $p_{\parallel}$  and  $p_{\perp}$  of breakup fragments was measured. However, it is necessary to assume a distribution shape, for example Lorentzian or Gaussian, to interpret  $p_{\perp}$  distributions. In comparison, a projection of the  $p_{\perp}$  distribution onto one axis removes this complication and provides a distribution that is simpler to interpret.

The  $p_x$  distributions are the projection of  $p_{\perp}$  onto the horizontal axis. Although a set of PPACs was present, to permit ray tracing of the incoming  ${}^8\text{B}$  and outgoing  ${}^7\text{Be}$  trajectories, it was found that the angular resolution for deflections (19 MeV/c) was comparable to the angular spread of the incoming beam (26 MeV/c). Therefore, the data are binned according to the horizontal position of the strip that detects them. These distributions are corrected by subtracting in quadrature the widths of the angular spread of the incoming  ${}^8\text{B}$  beam and the contribution due to multiple

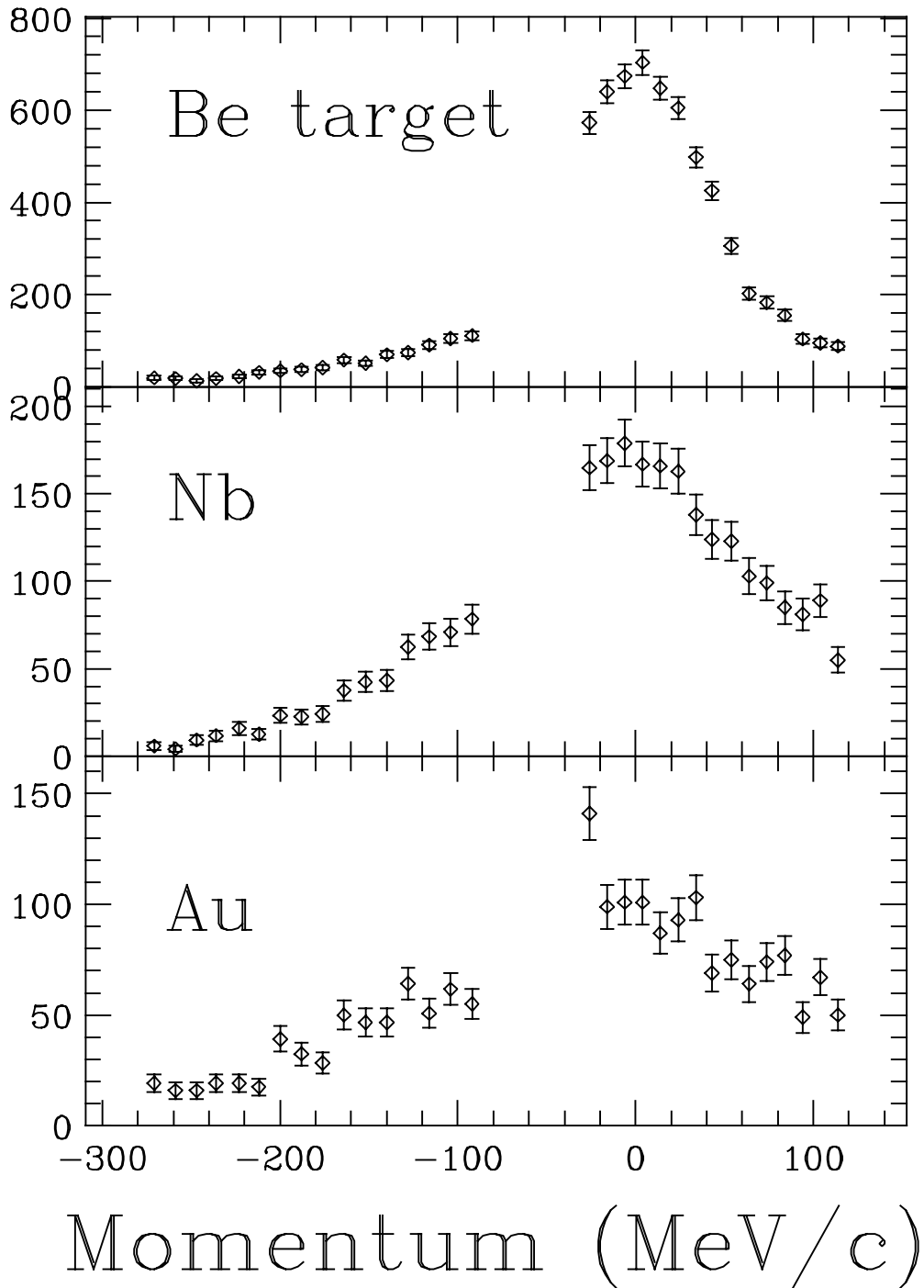


Figure 4.5: The  $p_x$  distributions of  ${}^7\text{Be}$  fragments following the breakup of  ${}^8\text{B}$ .

Table 4.3: Summary of the  $p_x$  distribution results.

Target	Uncorrected FWHM ( MeV/c )	Resolution and Beam spread ( MeV/c )	Multiple scattering ( MeV/c )	Corrected FWHM ( MeV/c )
Be	$91\pm 8$	$26\pm 1$	8	$87\pm 8$
Nb	$162\pm 15$	$26\pm 1$	34	$156\pm 15$
Au	$242\pm 20$	$26\pm 1$	56	$234\pm 20$

scattering from the measured widths (FWHM) of the  $p_x$  distributions.

Like the  $p_{\parallel}$  distribution,  $p_x$  distributions result from a projection of the momentum density distribution onto one axis. Therefore, in the absence of reaction mechanism and final state interaction effects these distributions could be directly compared. For example, the  $p_{\parallel}$  and  $p_x$  distributions are almost the same for the  ${}^9\text{Be}$  target. On the other hand, the  $p_{\parallel}$  distribution for breakup in the Au target is narrow while the  $p_x$  distribution has a width near 240 MeV/c, apparently because of a sideways Coulomb deflection in the field of Au. Since  $p_{\parallel}$  is less affected than  $p_{\perp}$  by reaction mechanism details and final state interactions, such as diffraction and Coulomb deflection [Ber92],  $p_{\parallel}$  is the focus of the remaining sections.

### 4.3.2 The $P_{\parallel}$ Distributions

The  ${}^7\text{Be}$  fragment  $p_{\parallel}$  distributions measured in Telescope 1 and Telescope 2 are shown in Figure 4.6. Experimental effects that broaden the observed  $p_{\parallel}$  distributions are assumed to have Gaussian resolution functions. The widths of these functions (FWHM) are subtracted, in quadrature, from the widths of the  $p_{\parallel}$  distributions. These include the small, but not negligible, spread in the momentum of the incoming beam; the momentum resolution of the telescopes and the energy spread associated with the thick targets. Finally, the transformation into the  ${}^8\text{B}$  rest frame reduces the width

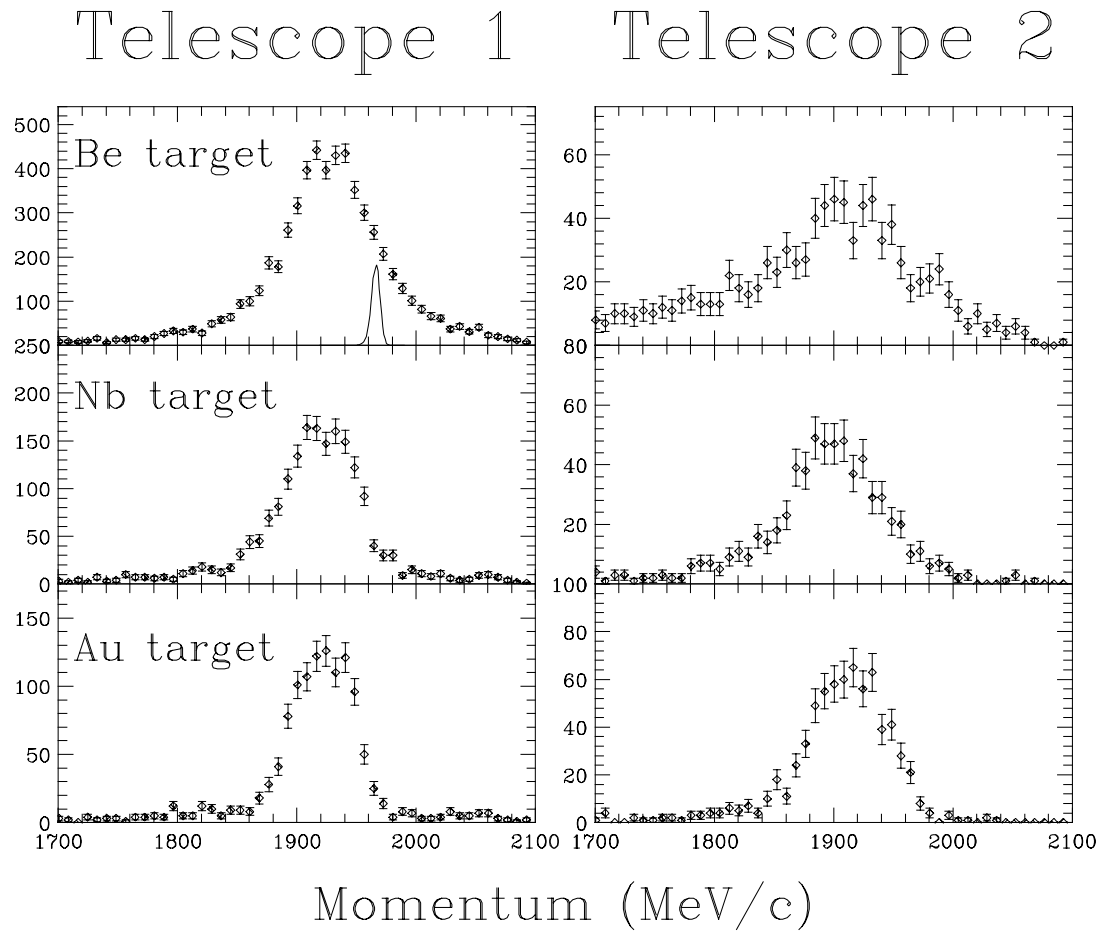


Figure 4.6: The  $p_{\parallel}$  distributions of  ${}^7\text{Be}$  fragments following the breakup of  ${}^8\text{B}$ . The narrow distribution shown with the Telescope 1 Be target data shows the momentum resolution ( $\sim 0.5\%$ ) obtained from one of the energy calibration measurements.

Table 4.4: Widths (uncertainties) of the  $p_{||}$  distributions of  ${}^7\text{Be}$  fragments following  ${}^8\text{B}$  breakup. All widths are FWHM.

Target	Uncorrected FWHM ( MeV/c )	Resolution and Beam Spread ( MeV/c )	Differential E-loss ${}^7\text{Be}$ and ${}^8\text{B}$ ( MeV/c )	Corrected FWHM ( MeV/c )	${}^8\text{B}$ Rest Frame ( MeV/c )
Telescope 1					
Be	$86\pm 4$	$13.5\pm 1$	8	$85\pm 4$	$81\pm 4$
Nb	$73\pm 4$	$13.5\pm 1$	10	$71\pm 4$	$68\pm 4$
Au	$67\pm 3$	$13.5\pm 1$	8	$65\pm 3$	$62\pm 3$
Telescope 2					
Be	$140\pm 20$	$12.1\pm 1$	8	$139\pm 20$	$133\pm 19$
Nb	$87\pm 10$	$12.1\pm 1$	10	$86\pm 10$	$82\pm 10$
Au	$80\pm 6$	$12.1\pm 1$	8	$79\pm 6$	$75\pm 6$

by 4.4%.

Target out runs showed that the background was smaller than 0.2 counts per MeV/c for all targets. Therefore, there was no background subtraction. The distributions are displayed in 8 MeV/c bins.

## 4.4 Results

The present results yield  $p_{||}$  distribution widths around 62-81 MeV/c in Telescope 1, and show a systematic dependence of the widths on the target  $Z$ . These widths are much smaller than those of normally bound nuclei, and based on this information alone, one would conclude that  ${}^8\text{B}$  has a proton halo. On the other hand, the momentum wavefunction of a proton bound by 137 keV in a p-orbital Woods-Saxon potential, that is adjusted to reproduce the proton separation energy and the  ${}^7\text{Be}$  core radius, yields a momentum distribution width of 160 MeV/c [Esb95].

#### 4.4.1 The $P_{\parallel}$ Distribution from Nuclear Breakup Processes

In the Serber interpretation, the data from breakup in the Be target, where nuclear process dominate the breakup, could be compared with the momentum wavefunction of the valence proton. However, the two are not in agreement (81 MeV/c vs. 160 MeV/c). Since the Serber approach fails to reproduce the data it appears that the reaction mechanisms influence the final momenta of the core fragment following the removal of the p-orbital valence proton. Therefore, the details of the breakup reaction must be included in the calculations.

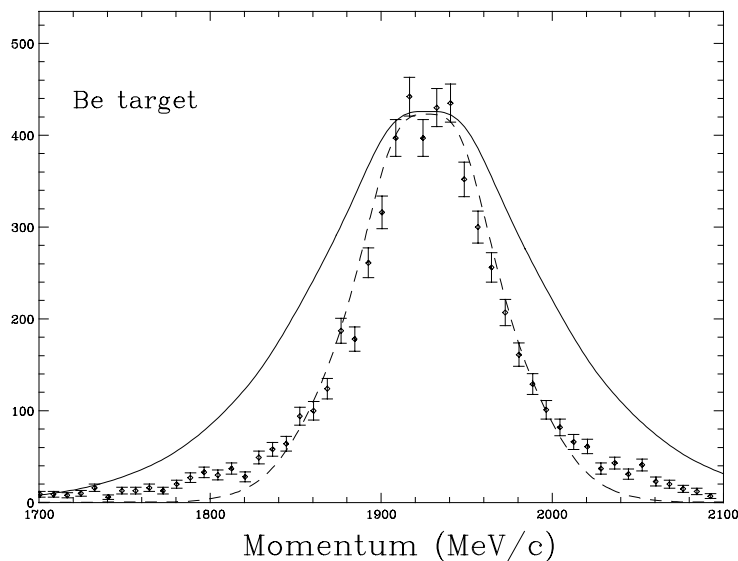


Figure 4.7: The data from breakup in the Be target compared with the predicted  $p_{\parallel}$  distribution of a p-orbital proton bound by 137 keV in a Woods-Saxon potential. The solid(dashed) line represents the distribution without(with) an absorptive cut-off [Bro95a].

In the spirit of the Friedman model and the Extended Serber model, discussed in Appendix C, Brown *et al.* have explored the sensitivity of the predicted  $p_{\parallel}$  distribution to an absorptive cut-off radius [Bro95b]. When the cut-off radius is defined as the radius where the density of the valence proton exceeds the density of the  ${}^7\text{Be}$  core, only

the wavefunction outside this limit is considered. The resulting width of the proton  $p_{\parallel}$  distribution is 96 MeV/c, nearly in agreement with the data. This approach is not rigorously correct, since it does not attempt to imitate the situation where the wavefunction is sampled only at large impact parameters, but the method does demonstrate that the observed distribution should be sensitive to these effects.

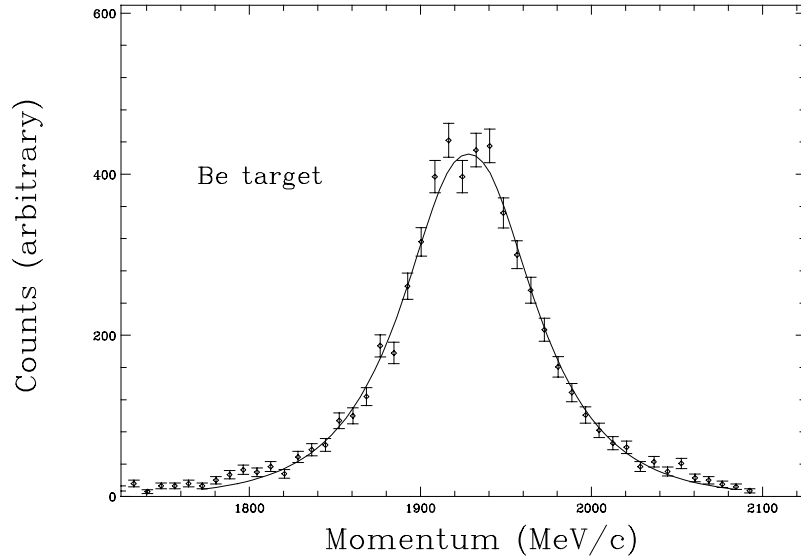


Figure 4.8: The  $p_{\parallel}$  predicted by Esbensen’s model that specifically considers the  $m_{\ell}$  sub-states. Only absorptive processes are included [Esb95].

In comparison, Esbensen [Esb95] is developing a model that considers the orientation of the quantum sub-states of the  $p_{3/2}$  wavefunction. The general model was described by [Bar93] though reaction effects that could alter the distribution will be added. Specifically, an interaction of the target with a proton in a  $m_{\ell}=0$  state (oriented along the beam axis) would usually lead to a collision of the core with the target nucleus, and possibly a disintegration of the core. Therefore, absorption of protons that are in the  $m_{\ell} = 0$  sub-state is highly suppressed when measuring core fragments. Esbensen finds that the  $m_{\ell}=0$  sub-states contribute only 18% of the total breakup cross section, instead of 33%, and this leads to a distribution of width 83 MeV/c.

In the future, diffractive effects, that broaden the distribution, will be added to the model.

### **Measurement of ${}^7\text{Be}$ Fragment $P_{\parallel}$ from 1471A MeV ${}^8\text{B}$ in a Dispersion Matched Energy Loss Spectrometer**

Recently, a group at GSI measured the  $P_{\parallel}$  momentum distribution of  ${}^7\text{Be}$  fragments following the breakup of 1471A MeV  ${}^8\text{B}$ . The resulting momentum distribution from breakup in a light (carbon) target [Sch95] has a width of  $81 \pm 6$  MeV/c, in excellent agreement with the present data.

#### **4.4.2 The $P_{\parallel}$ Distribution From Coulomb Breakup Processes**

The magnitude of the valence proton wavefunction in  ${}^8\text{B}$  at large radii is of interest for determining the rate of the  ${}^7\text{Be}(p,\gamma){}^8\text{B}$  reaction that leads to high energy neutrinos in the sun. A longstanding problem for solar models is an inability to reproduce the  ${}^8\text{B}$  formation rate in the sun, which is deduced from the observed rate of high energy neutrinos reaching the earth. In an effort to solve the solar neutrino problem, recent exclusive measurements of Coulomb breakup have been used to determine this rate, via Detailed Balance, for energies of 600-1000 keV [Mot94]. The E2 contribution to the breakup cross section must be known to extract the relevant E1 part of the reaction rate from these experiments, but the size of the contribution is debatable [Lan94].

The inclusive momentum distributions that we measure are sensitive to the interference of the E1 and E2 contributions to the breakup process. The distribution from the Au target has a noticeable asymmetry, the signature of the interference, and permits an estimate of the E2 contribution.

The Coulomb breakup is calculated in a perturbative model similar to [Esb91], and

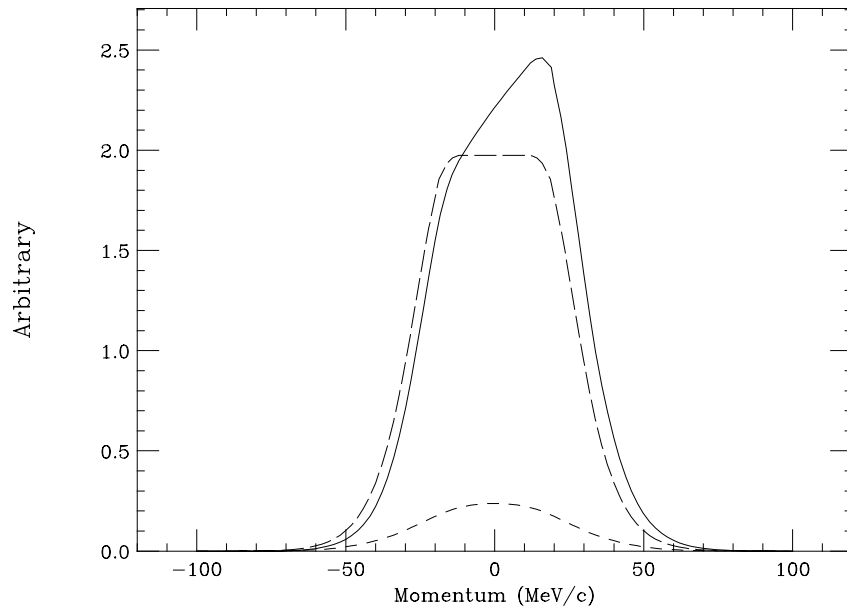


Figure 4.9: [Esb95] The predicted shapes of the momentum distributions from E1 (long dashes), E2 (short dashes) and E1+E2 (solid) Coulomb breakup. An asymmetry in the shape of the distribution is the result of the E1+E2 interference.

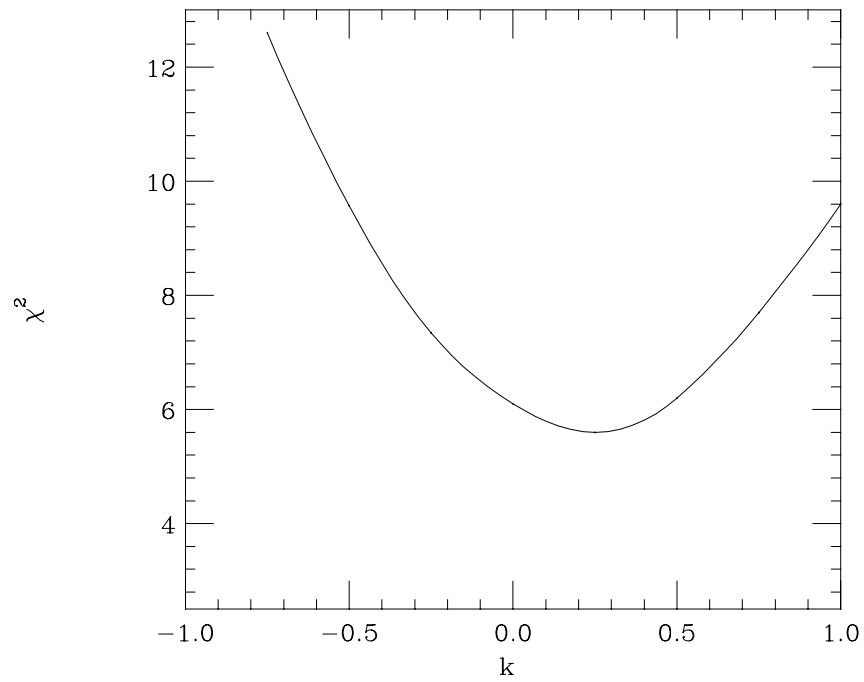


Figure 4.10: The  $\chi^2$  minimization to obtain the E2 strength that best reproduces the observed  ${}^7\text{Be}$   $p_{\parallel}$  distribution from  ${}^8\text{B}$  breakup on the Au target.

by varying the E2 strength ( $|E1+kE2|^2$ ) it was possible to adjust  $k$  to reproduce the data [Esb95]. Negative values of  $k$  represent the mirror reflection of the asymmetric distribution which gives a distribution sloped in the opposite direction. The  $\chi^2$  is minimized when  $k=0.25$  in this model; this corresponds to an E2 contribution that is 0.7% of the total breakup cross section. In Figure 4.11 the resulting distribution is transformed into the lab frame, convoluted with experimental effects and shown in comparison with the data from breakup in the Au target.

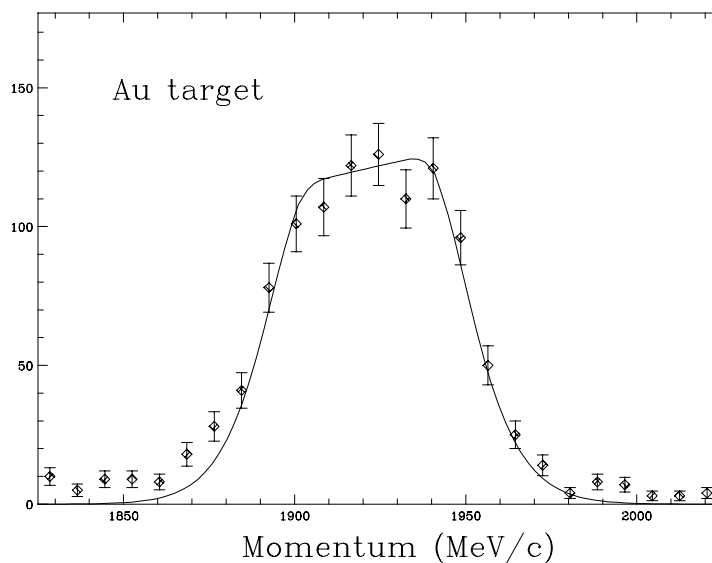


Figure 4.11: The  ${}^7\text{Be}$  fragment  $p_{\parallel}$  data compared with the predicted distribution obtained when  $k=0.25$  [Esb95]. The corresponding E2 strength is 0.7% of the total strength.

#### 4.4.3 Angular Dependence of the Width of the $P_{\parallel}$ Distribution

Since the Cartesian components of the momentum wavefunction may not be separable into independent functions of each coordinate [Rii93a], the measured parallel momentum distribution could be sensitive to the angular coverage of the detectors, as described in Appendix E. By measuring the  $p_{\parallel}$  and  $p_{\perp}$  of the fragments simul-

taneously we observed these effects. The  $p_{\perp}$  perturbations associated with the Nb and Au targets appear to distort the  ${}^7\text{Be}$  angular distributions. Therefore, we briefly comment only on the Be target data.

When a Lorentzian distribution ( $\Gamma=95$  MeV/c) is assumed the limited acceptance leads to  $p_{\parallel}$  distribution widths of 80 MeV/c and 180 MeV/c in the two telescopes. Although the measured distribution widths are  $81\pm 6$  MeV/c and  $133\pm 19$  MeV/c the dependence is similar to that expected for a Lorentzian momentum distribution, though not as extreme. Poor statistics in Telescope 2 limit discussion on this topic.

In contrast, the fragment  $p_{\parallel}$  distribution widths from 250A MeV  ${}^{12}\text{C}$  ions [Kid88] remain constant out to at least  $4.5^\circ$ , and indicate a different, more Gaussian-like behavior in the fragmentation of tightly-bound stable nuclei.

## 4.5 Valence Proton Radius

The  $p_{\parallel}$  distributions of  ${}^7\text{Be}$  from  ${}^8\text{B}$  on both light and heavy targets appear to be significantly influenced by reaction mechanism effects. Predictions that agree well with the data assume a single-particle p-orbital proton bound by 137 keV. The corresponding rms radius for the valence proton is large (4.24 fm) [Esb95] and is taken to indicate that  ${}^8\text{B}$  possess an extended proton distribution for the valence proton. A comparison of the probability distribution of core nucleons with the distribution of the valence proton shows that at large radii the density of the proton is dominant.

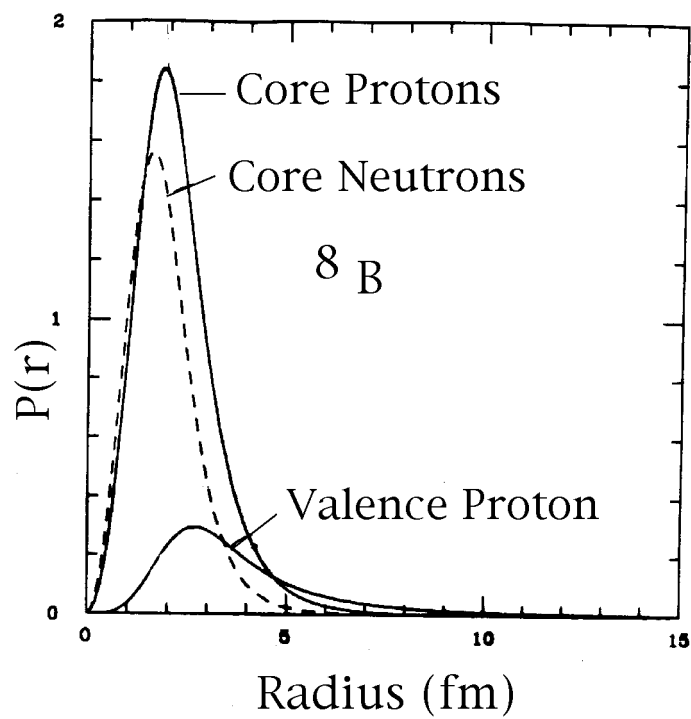


Figure 4.12: [Bro95a] The probability distribution of nucleons in  $^8\text{B}$ .

# Chapter 5

## Summary and Outlook

The two measurements of breakup fragment momenta in the direction parallel with the beam direction described in Chapters 3 and 4 are in good agreement with predictions based on the loosely bound nature of the valence nucleons. However, the fragment momentum distributions are found to have very different sensitivities to the reactions that lead to their formation.

In the first case,  $^{10}\text{Be}$  fragments following the breakup of  $^{11}\text{Be}$ , the data agree with a simple projection of the spherically symmetric wavefunction of a  $2s_{1/2}$  neutron bound by 500 keV in a Woods-Saxon potential. The influences of reaction mechanism effects appear small and are not included in our comparisons with the data. For example, the  $p_{\parallel}$  distribution expected from Coulomb dipole excitation leads to a width that is roughly 14% narrower than that of the projected momentum wavefunction [Esb94]. A similar sized decrease in width is found by [Bro95a] when a radial cut-off, described in Section 4.4.1, is included in the projection of the momentum wavefunction. Therefore, it appears that the observed momentum distributions reflect the momentum of the halo neutron of  $^{11}\text{Be}$  with only small influences arising from the reaction mechanisms.

The situation for  $^8\text{B}$  is somewhat different. The momentum distributions are narrow, which indicates a different behavior from the fragmentation of normal nuclei

where widths of 180 MeV/c FWHM or larger are expected [Gol74]. However, the simple projected wavefunction of a p-orbital proton bound by 137 keV in a Woods-Saxon potential is not in agreement with the observed  $p_{\parallel}$  distributions. When reaction mechanism effects are included in the calculations the predicted widths are decreased substantially, and are in much better agreement with the data. In fact, it appears that the  $p_{\parallel}$  distribution observed for breakup on the Au target reveals the contribution of E2 strength in the Coulomb breakup calculation. In the future, Esbensen will make more detailed dynamical calculations in order to account for the higher order effects of the reaction mechanisms [Esb95].

The results of the two measurements indicate that when the extent of the halo is large, as in the case of  $^{11}\text{Be}$  (rms radius=6.5 fm), the reaction mechanisms do not strongly influence the breakup core fragments, and that simple measurements of the core fragments reflect the properties of the halo nucleon. In the case of  $^8\text{B}$ , the valence proton does extend considerably (4.25 fm). However, since the proton density is not as prominent at large radii as the neutron halo of  $^{11}\text{Be}$ , the reaction mechanisms influence the  $^7\text{Be}$  fragment momentum distributions from  $^8\text{B}$  breakup.





# Appendix A

## Theoretical Discussion of Halo Nuclei

Theoretical studies of halo nuclei have progressed, and the influence of various potentials on the wavefunction of halo nucleons has been studied by [Rii92]. There is a clear dependence of the extent of the wavefunction on the binding energy. However, when the rms radius of the wavefunction of a neutron in a square-well potential was compared with that of a neutron in a Gaussian shaped potential, the wavefunction associated with the Gaussian shape extended slightly further. In this case the "softer" wall of the Gaussian potential permits a somewhat larger halo. Because the dependence on the potential shape can be observed in such a simple calculation, it is clear that realistic potentials should be used for comparisons with data. Riisager *et al.* approach their studies using Gaussian shaped potential shapes,

$$U(r) = S_0 \exp(-r^2/b^2). \tag{A.1}$$

The value  $b=2.1$  fm is realistic for a nuclear core radius.

### A.1 Importance of the Binding Energy

Consideration of a valence s-orbital neutron shows that as the binding energy increases the wavefunction of the valence neutron is "squeezed" into the core, Fig-

ure A.1. Since other potential barriers, such as the angular momentum barrier and the Coulomb barrier, also play key roles in determining the long-range characteristics of the wavefunction, these potentials must also be considered.

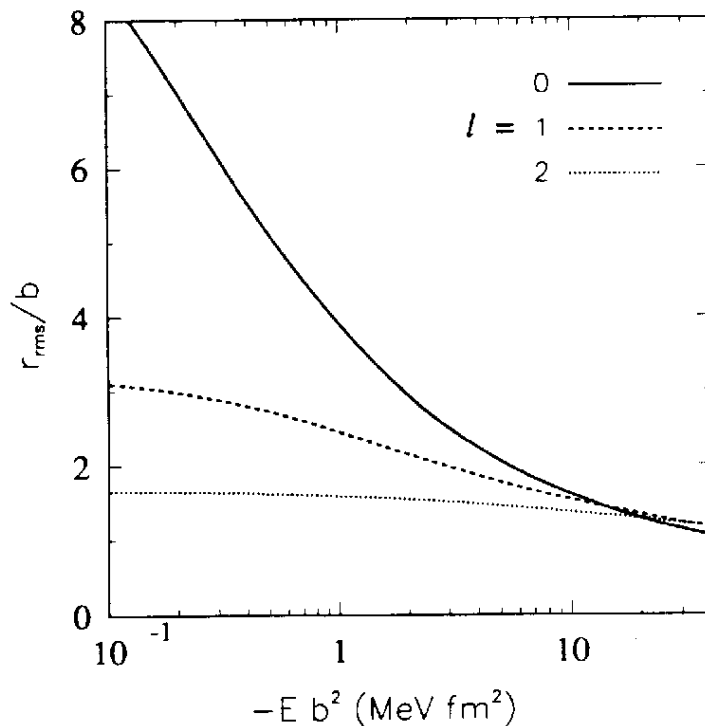


Figure A.1: [Rii92] The dependence of the rms radius of valence neutrons on binding energy ( $b \approx 2.1$  fm).

### Importance of the Angular Momentum Barrier

The halo nucleus  $^{11}\text{Be}$  is not complicated by the angular momentum barrier. However, to understand the long range behavior of the wavefunctions in other weakly bound nuclei with valence nucleons in non-s-orbitals, for example  $^8\text{B}$  ( $\ell=1$ ), this potential is important. The angular momentum barrier is,

$$V(r) = \ell(\ell + 1) \frac{\hbar^2}{2mr^2}. \quad (\text{A.2})$$

It appears, from Figure A.1, that significant penetration can occur only for s- and p-orbital neutrons that have small binding energies. The wave function diverges as

$E^{-1/2}$  for an s-wave neutron, and as  $E^{-1/4}$  for a p-wave neutron. Higher angular momentum orbitals remain finite regardless of the binding energy. Although there have not yet been any studies of neutron halo nuclei that have a single halo neutron in a non-s-orbital a few candidates do exist ( $^{14}\text{B}$ ,  $^{15}\text{C}$  and  $^{17}\text{C}$ ). When studies of a broader range of nuclei have been completed, our detailed understanding of the influences of the angular momentum barrier will be greatly enhanced.

## A.2 Importance of the Coulomb Potential Barrier

The Coulomb potential barrier is large in high  $Z$  nuclei. However, it appears that light proton rich nuclei like  $^8\text{B}$  can possess an extended proton distribution. Much like the angular momentum barrier, the Coulomb barrier inhibits a halo in in weakly-bound proton-rich nuclei. Assuming that the charge distribution is Gaussian, the Coulomb potential is,

$$U(r)_{Coulomb} = \frac{Z_{halo}Z_{core}\epsilon^2}{r} \text{erf}(r/b_{core}). \quad (\text{A.3})$$

Here  $\text{erf}$  is the error function. As the binding energy decreases the rms radius of the wavefunction increases. However, near 100 keV  $\text{fm}^2$  in Figure A.2 the barrier penetration of the proton wavefunction is dominated by the Coulomb potential, and below this value there appears to be little sensitivity to the binding energy.

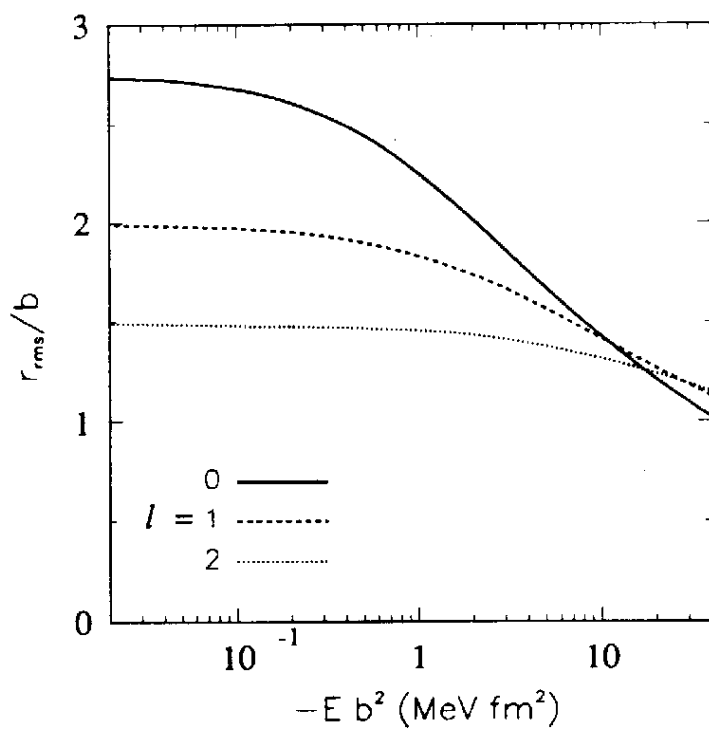


Figure A.2: [Rii92] The dependence of the rms radius of a valence proton on binding energy for a nucleus that has four protons in the core, for example  ${}^8\text{B}$ .

# Appendix B

## Experimental Evidence for Halo Nuclei

Simple problems of barrier penetration are well understood, and the current measurements on  $^{11}\text{Li}$  and  $^{11}\text{Be}$  taken independently are consistent with an interpretation that includes a halo. When considered collectively, the measurements overwhelmingly favor the existence of neutron halos.

### B.1 Enhanced E1 Transition Strength

The first excited state of  $^{11}\text{Be}$  is only 320 keV above the ground state, and the first observation indicating a neutron halo was in 1983 when a very short gamma decay lifetime ( $1.7 \times 10^{-13}$  seconds) of this state was observed [Mil83]. Such a small lifetime requires that large distances, on the order of the size of a halo, must be involved in the transition.

### B.2 Measurements of Reaction Cross Sections

Reaction cross section measurements appear to be a straightforward method of measuring nuclear sizes, since the cross section is nearly proportional to the square of the rms radius. In the Berkeley experiments [Tan85a, Tan85b, Tan88] isotopic identifi-

cation was obtained for reaction products from interactions of 790A MeV He, Li, Be and B isotopes in a range of targets. Therefore, reactions that changed either the A or Z of the projectile were detected. The "interaction" cross sections were initially analyzed using a simple "hard sphere" Glauber-model approach,

$$\sigma_I = \pi[R_I(target) + R_I(projectile)]^2. \quad (\text{B.1})$$

However, the radii extracted for the  $^3\text{He}$  and  $^4\text{He}$  isotopes indicated that a different approach was necessary to interpret the data. Using a model developed by Karol [Kar75] that treats nuclei as "soft" spheres rather than "hard" spheres or black disks, values of the rms radii of the proton, neutron and matter density distributions were obtained.

The systematics of the rms radii provided a measure of the growth in nuclear size with increasing atomic number, and a comparison with the well known  $r = r_o A^{1/3}$  rule. It was observed that the rms radius of most light p-shell nuclei was nearly the same, lying between 2.3-2.4 fm. However, the neutron-rich nuclei  $^6\text{He}$ ,  $^8\text{He}$ ,  $^{11}\text{Be}$ ,  $^{14}\text{Be}$ , and  $^{11}\text{Li}$  exhibited nuclear radii that were considerably larger than other more tightly bound nuclei, see Figure 1.1.

The information provided by the difference between the rms radius of the neutrons and the rms radius of the protons, seen in Figure B.1, clarifies that this group of nuclei possesses thick neutron skins or halos.

The reaction cross sections of  $^6\text{He}$  ( $S_{2n}=970$  keV) and  $^8\text{He}$  ( $S_{2n}=2100$  keV) showed indications of extended neutron distributions. However, a deformation due possibly to clustering could lead to erroneous values for the rms radii derived from cross section data for the proton and neutron density distributions. For example, a thick neutron layer surrounds the nucleus  $^8\text{He}$ , though the binding energy of the valence neutrons is large. In this case, it appears that the neutron layer is simply the result of having two

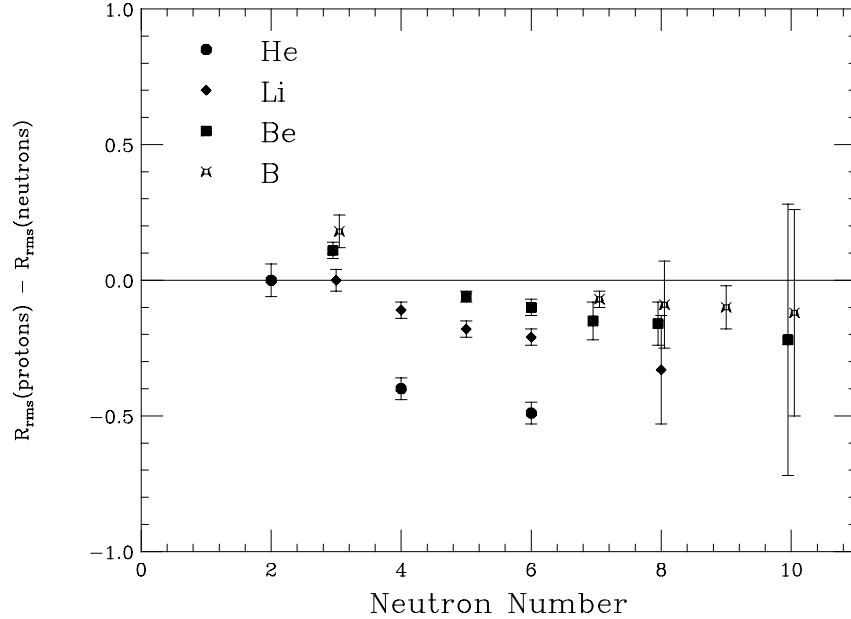


Figure B.1: The difference between the proton density rms radius and the neutron density rms radius obtained from the 790A MeV cross section measurements. Data from [Tan88].

protons and six neutrons in the nucleus. This leads to rather different Fermi energies for the protons and neutrons.

### B.3 Energy Dependence of the $^{11}\text{Be}$ Reaction Cross Section

A two- or three-body approach for halo nuclei is permitted only by an assumption that there is a well defined distinction between the core and the halo. To investigate this assumption Fukuda *et al.* [Fuk91] measured the reaction cross section of 33A MeV  $^{11}\text{Be}$  and compared with the 790A MeV data of Tanihata [Tan88]. Consideration of the energy dependence of the nucleon-nucleon cross sections, permitted a more accurate determination of the proton and neutron density distributions than could be obtained from the 790A MeV data alone. As can be seen from the increase in the

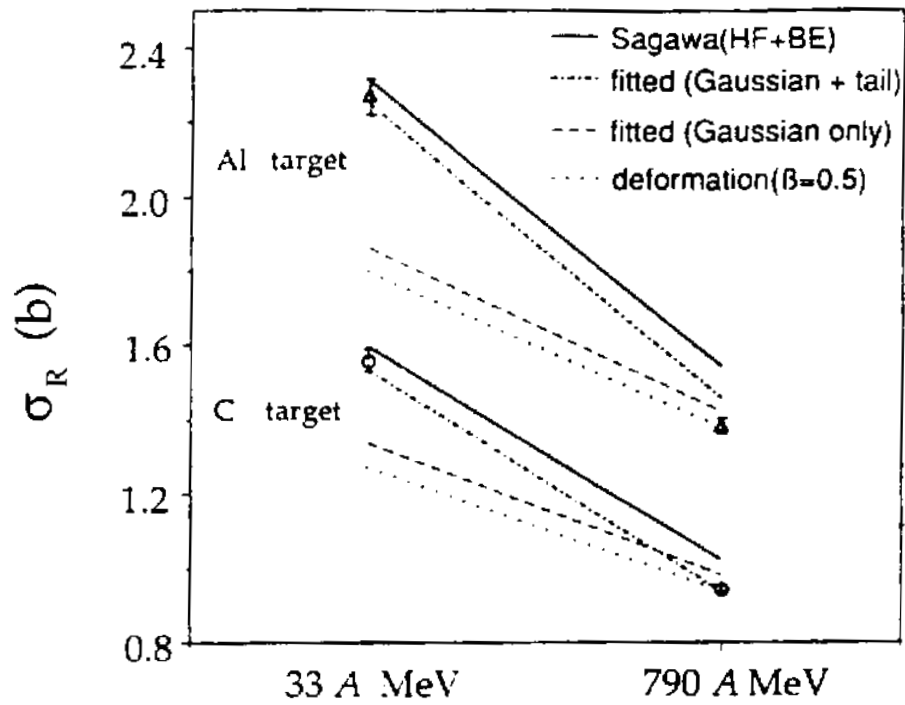


Figure B.2: [Fuk91] The energy dependence of the  $^{11}\text{Be}$  reaction cross section. The two models that fit the trend of the data both include a large halo, while a deformation in  $^{11}\text{Be}$  does not reproduce the data.

nucleon-nucleon cross sections,

$$\sigma_{pp}(33MeV)/\sigma_{pp}(790MeV) = 2.0 \quad (\text{B.2})$$

and,

$$\sigma_{pn}(33MeV)/\sigma_{pn}(790MeV) = 7.2, \quad (\text{B.3})$$

at lower energies the reaction cross section is sensitive to the neutron distribution at a density that is much lower than is the case for the cross section data of Tanihata.

An increase in the reaction cross section, similar to that expected for a neutron halo structure, was observed. However, because the increase in the cross section could also be produced by deformation, for example due to clustering in the nucleus, the data were compared to predictions from several halo models and cluster models. The data favors a Hartree-Foch calculation with a well depth that gives the neutron separation energy. Because the change in the cross section is most sensitive to the tail of the density distribution, the observed behavior shows the presence of the extended tail in the wavefunction of the valence neutron. However, the method is not very sensitive to the details of the wavefunction.

## B.4 Large Electromagnetic Dissociation Cross Section

The nucleus  $^{11}\text{Li}$  became the focus of many experiments because of its three-body nature and very low binding energy ( $295 \pm 26$  keV). The low binding indicates that the Coulomb breakup cross section on heavy targets should be enhanced [Han87], and it has been suggested that a soft dipole mode could exist that is figuratively represented as an oscillation of the core against the halo neutrons. This oscillating mode would have an energy much lower than the giant dipole resonance, which represents the oscillation of all of the protons in the nucleus against all of the neutrons.

The Soft Dipole oscillation is easily excitable via electromagnetic excitation when a halo nucleus passes near a heavy nucleus at relativistic velocities. A study of the Coulomb breakup cross section of 70A MeV  $^{11}\text{Li}$  showed a strong target  $Z$  dependence [Bla91]; the reaction cross section changed from 1.24 barns on C to 7.23 barns on Pb. This supported the neutron halo model for  $^{11}\text{Li}$ . However, the data were also consistent with breakup cross sections expected from excitation of the giant dipole resonance. Therefore further experiments were necessary in order to fully probe the wavefunction.

## B.5 The $^{11}\text{Li}$ Dipole Excitation Strength Function

To determine what breakup mechanism accounts for the reaction cross section data, soft dipole excitation or giant dipole excitation, a kinematically complete measurement of the full three-body systematics for Coulomb dissociation of  $^{11}\text{Li}$  was performed at the NSCL [Sac93, Iek93]. A beam of 30A MeV  $^{11}\text{Li}$  nuclei impinged on a Pb target and the decay energy spectrum of  $^{11}\text{Li}$  from Coulomb Excitation was measured using a position sensitive  $^9\text{Li}$  fragment detector and a wall of neutron detectors. The dipole excitation strength function was deduced from the relative energy spectrum of the  $^9\text{Li}$ -n-n system and showed a low energy peak near 1 MeV. Since the giant dipole resonance energy should correspond to an excitation energy near  $77A^{-1/3}$  MeV (34 MeV) this observation strongly favored the neutron halo interpretation.

Early interpretation of the data assumed that a soft dipole resonance state participated strongly in the process. However, the shape was also consistent with that expected from breakup into the continuum, Figure B.3. The observation of Coulomb reacceleration of the heavy core after breakup (see Appendix F) provided evidence that the breakup time scale was very short and was consistent with a direct breakup

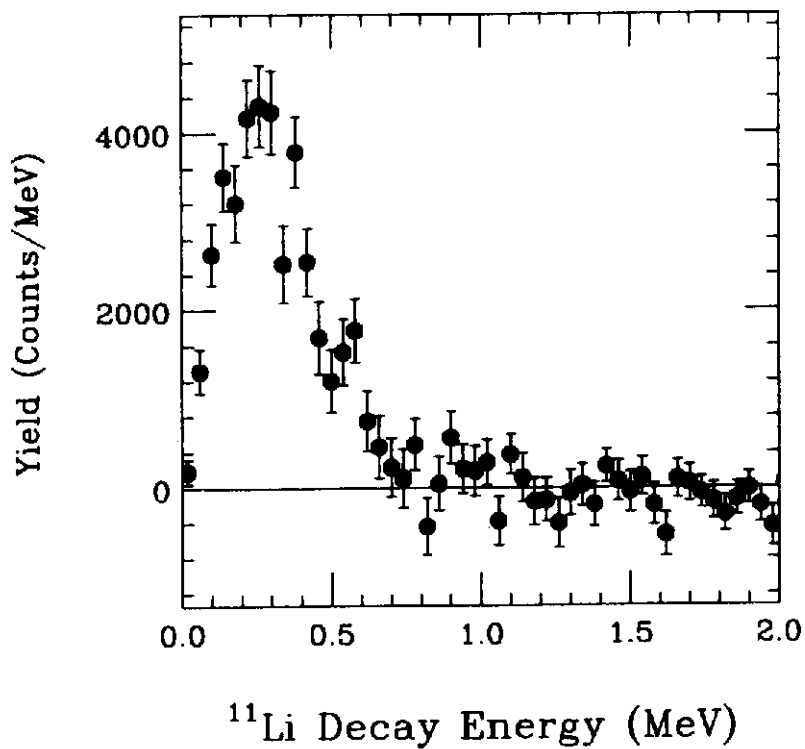


Figure B.3: [Sac93] The decay energy spectrum of  $^{11}\text{Li}$  from Coulomb excitation. A Monte Carlo simulation that accounts for the acceptance of the measurement indicates a peak near 1 MeV in the dipole excitation strength function. The low energy peak is associated with a large separation distance for the  $^9\text{Li}$  core and two neutrons that comprise  $^{11}\text{Li}$

into continuum states. Because the breakup processes are direct, measurements reflect the ground state properties.

## B.6 The $^{11}\text{Be}$ Dipole Excitation Strength Function

The large halo-core separation distance can be directly related to a concentration of strength at low energy in the dipole-excitation strength function. Therefore, the  $^{10}\text{Be}$ -n relative energy spectrum from breakup on a Pb target [Nak94] was measured which permitted a determination of the E1 strength function of  $^{11}\text{Be}$ . In the model used by Nakamura *et al.* the rms radius of the halo neutron that reproduces the data is  $6.4 \pm 0.7$  fm.

The measurement of the  $^{10}\text{Be}$ -n center of mass scattering angle permitted a complete investigation of the Coulomb post-acceleration effect (Appendix F), which implies that for a direct breakup charged fragments will emerge with a higher average energy than neutrons. This effect is strongly related to the impact parameter, and as can be seen in Figure B.4, this trend is followed. Therefore, the presence of Coulomb reacceleration is further evidence that the breakup process is direct, into continuum states, a key assumption in the Serber model.

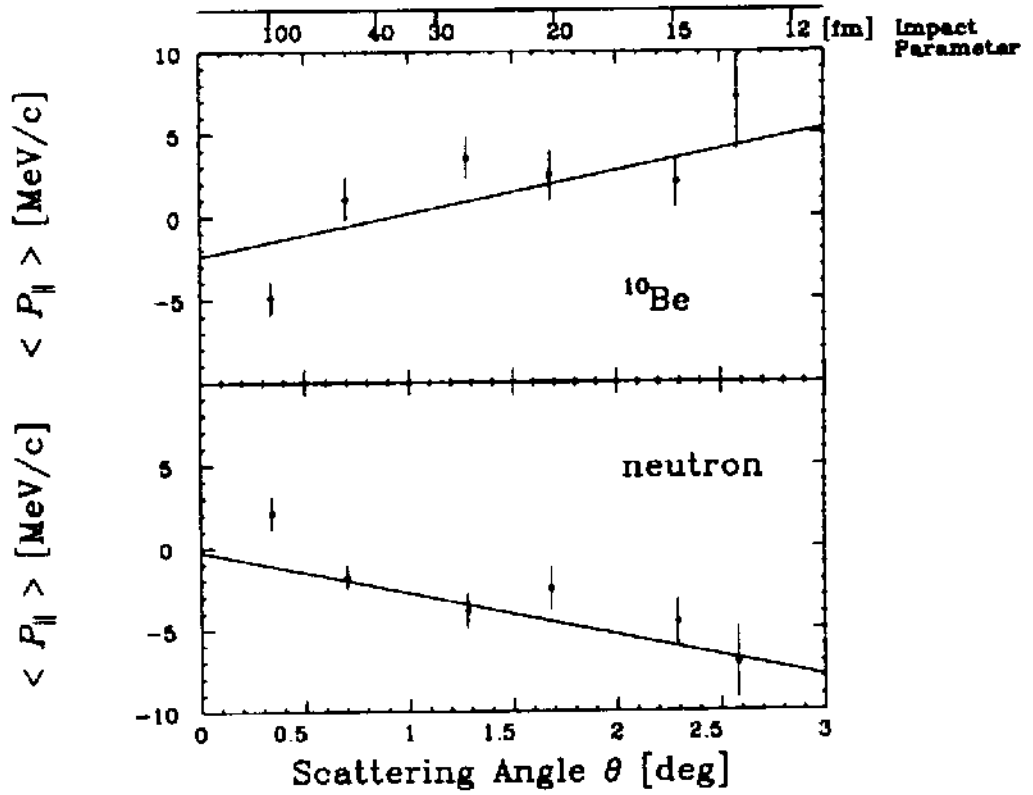


Figure B.4: [Nak94] The mean momentum of breakup neutrons and  $^{10}\text{Be}$  cores plotted vs. the center of mass angle. The trend expected from Coulomb reacceleration is observed. This strongly favors a direct breakup interpretation of the data from  $^{11}\text{Be}$  Coulomb breakup.



# Appendix C

## Models for Fragment Momentum Distributions

### C.1 The Goldhaber Model

The standard model for projectile-like fragment momentum distributions in intermediate and high energy fragmentation of stable nuclei is the Goldhaber model [Gol74]. In this model the width of fragment momentum distributions is related to the Fermi energy of the projectile; a Boltzman energy distribution is assumed. When a reaction strips away a portion of the projectile, the momentum distribution for the remaining part, the fragment, is

$$P_{fragment} = \sum_{A_{fragment}} p_i; \quad (C.1)$$

$p_i$  is the initial momentum of the fragment nucleons in the projectile prior to the breakup. The distribution is statistically related to the number of nucleons in the initial projectile and the number of nucleons in the final fragment. The momentum distributions are Gaussians with widths,

$$\sigma = \sigma_0 \sqrt{\frac{A_{fragment}(A_{projectile} - A_{fragment})}{A_{projectile} - 1}}. \quad (C.2)$$

The parameter  $\sigma_0$  is related to the Fermi momentum and is generally near 80 MeV/c. Hence for one nucleon removal in a fragmentation reaction the fragment momentum

distribution width  $\sigma=80$  MeV/c is anticipated; this leads to a width of 188 MeV/c (Full Width at Half Maximum, FWHM).

## C.2 The Serber Model

In a two-body system the Serber assumption [Ser47] implies that the momentum distribution of the core fragment directly reflects the momentum wavefunction of the halo neutron. Since the Serber model does not include reaction effects, the momentum distribution of halo and core fragments should be identical to the momentum wavefunction of the halo neutrons.

## C.3 The Friedman Model

The Friedman model includes influences of reaction mechanism effects [Fri83]. In first order the width of the momentum distribution is related to the cluster separation energy and the reduced mass of the halo neutrons,  $\sigma \propto \sqrt[4]{2\mu S_n}$ . This is related to the Yukawa parameter  $\rho$  (Equation 1.3) which describes the exponential fall-off of the wavefunction. However, the Friedman model assumes an absorptive cut-off limit which distinguishes it from the Serber model. It is thought that central collisions, where the core impacts the target, will result in a disintegration of the core. Collisions that remove only a few nucleons are generally peripheral, and this assumption leads to the absorptive cut-off. The absorptive cut-off limits consideration of the wavefunction only to impact parameters that are larger than the cut-off radius.

An additional effect related to the transfer of potential energy into kinetic energy as the projectile exits the Coulomb field of the target nucleus is termed Coulomb distortion. When the breakup occurs the potential energy will be divided among the projectile nucleons based on their charge. As the fragments accelerate out of the

Coulomb field of the target the  $p_{\parallel}$  distribution is distorted.

The widths predicted by the Friedman model  $\left(\propto \sqrt[4]{\frac{A_f(A_p - A_f)}{A_p} S_n}\right)$  are similar to those predicted by the Goldhaber model  $\left(\propto \sqrt{\frac{A_f(A_p - A_f)}{(A_p - 1)}}\right)$ . However, the treatment of Friedman moves a step beyond that of Goldhaber by including specific details about the structure of the fragment, the separation energy, that may have a strong influence on the fragment momentum distributions.

## C.4 The Extended Serber Model

The extended Serber model [Uts85] was developed by Utsunomiya and includes both Coulomb distortion and an absorptive cut-off limit. A key difference between the extended Serber model and the Friedman model is that the absorptive cut-off limit is determined by a critical radius where the constituents of the projectile take on a two-body nature. The core halo separation distance is characterized such that either the halo nucleon can be absorbed without disturbing the core ( $R > R_c$ ) or an interaction with the target would result in a destruction of the core ( $R < R_c$ ). Although the model was first applied to the stable nuclei  $^{12}\text{C}$ ,  $^{13}\text{C}$ , and  $^{14}\text{N}$  prior to the discovery of halo nuclei, this approach seems well suited for explaining the fragment momentum distributions from halo nuclei.



# Appendix D

## Coulomb Dissociation

Coulomb excitation occurs when a projectile enters the Coulomb field of a target nucleus. A summary of [Ber88] follows. At high velocities the electric field of the target nucleus is contracted into the plane which is transverse to the incident direction of travel (chosen as the  $z$  axis in Figure 2.3). The resulting electric and magnetic fields that the projectile nucleus will encounter, assuming straight line trajectories, are given by the equations,

$$E_z = \frac{-Z_{target}e\gamma vt}{[b^2 + (\gamma vt)^2]^{3/2}} \quad (D.1)$$

$$E_{\perp} = \frac{-Z_{target}e\gamma b}{[b^2 + (\gamma vt)^2]^{3/2}} \quad (D.2)$$

$$B_{\perp} = \beta \times \mathbf{E}_{\perp} \quad (D.3)$$

and,

$$B_z = 0. \quad (D.4)$$

Where  $v$  is the speed of the projectile,  $\beta=v/c$ ,  $1/\gamma = \sqrt{1-\beta^2}$  and  $t$  is time ( $t=0$  at the distance of closest approach).

When the interaction time is sufficiently short ( $\Delta t \sim b/\gamma c$ ) the electric fields can be approximated with two plane waves, one traveling parallel with the trajectory of the projectile and the other transverse to the trajectory of the projectile. The energy

incident on the projectile nucleus is,

$$I = \frac{c}{4\pi} |\mathbf{E} \times \mathbf{B}|, \quad (\text{D.5})$$

and the spectrum of virtual radiation, *ie.* the number of equivalent photons of energy  $\hbar\omega$  is given by,

$$N(\omega, b) = \frac{Z_{target}^2 \alpha}{\pi} \left(\frac{\omega}{\gamma v}\right)^2 \left(\frac{c}{v}\right)^2 \left[ K_1^2(\omega b/\gamma v) + \frac{1}{\gamma^2} K_0^2(\omega b/\gamma v) \right]. \quad (\text{D.6})$$

Here  $\alpha=1/137$ , and  $K_i(\omega b/\gamma v)$  are Modified Bessel functions. The probability for excitation via dipole (E1) photons is,

$$P(b) = \int I(\omega, b) \sigma_\gamma(\hbar\omega) d(\hbar\omega) \quad (\text{D.7})$$

$$= \int N(\omega, b) \sigma_\gamma(\hbar\omega) \frac{d(\omega)}{\omega}. \quad (\text{D.8})$$

The momentum distribution of fragments from Coulomb dissociation reflects the dipole excitation strength function, which is related to  $\sigma_\gamma(E_{breakup})$ .

# Appendix E

## The Influence of a Limited Acceptance on $P_{\parallel}$ Distributions

It has been pointed out that observed widths of the  $p_{\parallel}$  distribution might be affected by an incomplete acceptance for the breakup products [Rii93a], and the necessary corrections are not negligible for most measurements to date. In this section the effects that an incomplete angular acceptance for breakup fragments can have on the parallel momentum distributions are discussed, and analytical results for some simple cases are obtained. Finally, a correction procedure that is useful in the more general case is described.

### E.1 Nature of the Problem

The momentum distribution of the halo particles is not known a priori; however, two limiting forms, Lorentzian and Gaussian, are in common use. Hansen and Jonson [Han87] assume a Yukawa spatial wavefunction (Equation 1.2). When  $\Gamma = 2\hbar/\rho$ , and

$$\mathbf{p} = p_x \hat{\mathbf{e}}_x + p_y \hat{\mathbf{e}}_y + p_z \hat{\mathbf{e}}_z, \quad (\text{E.1})$$

the Fourier transform of the Yukawa radial wavefunction is a Lorentzian momentum wavefunction for the neutrons,

$$\Psi(\mathbf{p}) = \sqrt{\frac{\Gamma}{2\pi^2}} \frac{1}{\mathbf{p}^2 + \Gamma^2/4}. \quad (\text{E.2})$$

Therefore, a Lorentzian description of the halo and core fragment momentum distributions is a reasonable first approximation.

On the other hand, measurements of the fragment momentum distributions from tightly bound normal nuclei such as  $^{12}\text{C}$ ,  $^{14}\text{N}$  and  $^{16}\text{O}$ , [Kid88, Gla90, Sil88, Van79], are well described by Gaussian distributions. The Goldhaber model Section C.1, relates the width of the fragment momentum distribution to the Fermi momentum of the incoming projectile, and assumes a Boltzman energy distribution for nucleons. This leads to Gaussian momentum distributions with  $\sigma$  near 100 MeV/c (FWHM=2.355  $\sigma$ ).

Momentum distributions following the breakup of lightly bound halo nuclei have often been described by Gaussians or sums of Gaussians; however this description must be regarded as phenomenological, with no theoretical basis. More realistic distributions are generally intermediate in shape between Gaussian and Lorentzian, so that these distributions provide good starting points for dealing with the acceptance problem.

The situation for a Gaussian distribution is extraordinarily simple. Because it is separable into independent functions of the Cartesian components,

$$|\Psi^*(\mathbf{p})\Psi(\mathbf{p})| = \frac{1}{\sqrt{(2\pi\sigma^2)^3}} \exp\left(\frac{-|\mathbf{p}|^2}{2\sigma^2}\right) \quad (\text{E.3})$$

$$= \frac{1}{\sqrt{(2\pi\sigma^2)^3}} \exp\left(\frac{-p_x^2}{2\sigma^2}\right) \exp\left(\frac{-p_y^2}{2\sigma^2}\right) \exp\left(\frac{-p_z^2}{2\sigma^2}\right), \quad (\text{E.4})$$

a limited acceptance in  $p_x$  and  $p_y$  does not change the shape of the distribution of  $p_z$ . Thus measurements of breakup momenta from normal, stable nuclei are at most weakly influenced by acceptance effects.

However if the momentum distribution is non-Gaussian (e.g. Lorentzian or the sum of Gaussians) the incomplete acceptance for fragments can change the observed momentum distribution. The effect is rooted in the inseparability of the Cartesian components of the momentum density distribution. Key points relevant to measuring non-Gaussian momentum distributions are the following, an analytical solution for the predicted line shape of a Lorentzian distribution after passing through a limited acceptance, evidence that a strongly limited transverse acceptance (pinhole) leads to a increase in the width of the  $p_{\parallel}$  distribution when the observation angle is large enough, and a comparison with recent observations of the breakup of  $^{11}\text{Li}$  on Be and U targets. Finally a simple approach to estimating transverse acceptance effects when the analytical form of the density distribution cannot be integrated in closed form is outlined.

## E.2 Results

The measured momentum distributions are related to the momentum density distribution which is the square of the momentum wavefunction,

$$\rho(\mathbf{p}_{\mathbf{L}}) = |\Psi^*(\mathbf{p}_{\mathbf{L}})\Psi(\mathbf{p}_{\mathbf{L}})|. \quad (\text{E.5})$$

In the lab system,

$$\mathbf{p}_{\mathbf{L}} = p_x \hat{\mathbf{e}}_x + p_y \hat{\mathbf{e}}_y + ((1/\gamma)p_z + p_{ave.}) \hat{\mathbf{e}}_{\parallel} = p_{\perp} \hat{\mathbf{e}}_{\perp} + p_{\parallel} \hat{\mathbf{e}}_{\parallel}, \quad (\text{E.6})$$

when  $p_{ave}$  is the fragment average momentum, and  $\gamma$  is the relativistic correction factor. Observed momentum distributions reflect a projection onto a particular axis,

i.e. an integration of the momentum density distribution over the other coordinates in momentum space.

## E.2.1 Lorentzian Distribution

For a Lorentzian distribution

$$\rho(\mathbf{p}_L) = \frac{\Gamma}{2\pi^2} \frac{dp_x dp_y}{[\mathbf{p}^2 + \Gamma^2/4]^2}. \quad (\text{E.7})$$

The transverse ( $\perp$ ) and parallel ( $\parallel$ ) momentum distributions of this distribution are, assuming complete acceptance:

$$P(p_\perp) = \int_{-\infty}^{\infty} \rho(\mathbf{p}_L) dp_\parallel = \frac{\Gamma}{4\pi} \frac{1}{[p_\perp^2 + \Gamma^2/4]^{3/2}}, \quad (\text{E.8})$$

and

$$P(p_\parallel) = \int_{-\infty}^{\infty} \int_{-\infty}^{\infty} \rho(\mathbf{p}_L) dp_x dp_y = \frac{\Gamma}{2\pi} \frac{1}{(p_\parallel - p_{ave})^2 + \Gamma^2/4}. \quad (\text{E.9})$$

Notice that in the lab frame the  $p_\parallel$  distribution is broadened by  $\gamma$ , since  $p_\parallel - p_{ave} = (1/\gamma)p_z$ . When the entire momentum space is not sampled, the integration limits are finite, and  $P(p_\parallel)$  is modified. To simplify the integrations the transverse acceptance limits are taken to be rectangular in shape, and are given by  $p_{xlim} = \pm p_{ave} \sin(\Delta\theta/2)$  and  $p_{ylim} = \pm p_{ave} \sin(\Delta\phi/2)$ . Then the observed fragment parallel momentum distribution is [Mat94],

$$P_{obs}(p_\parallel) = \frac{\Gamma/\pi}{(p_\parallel - p_{ave})^2 + \Gamma^2/4} \times \left[ \frac{p_{xlim} \text{Atan}\left(\frac{p_{ylim}}{\sqrt{(p_\parallel - p_{ave})^2 + p_{xlim}^2 + \Gamma^2/4}}\right)}{\sqrt{(p_\parallel - p_{ave})^2 + p_{xlim}^2 + \Gamma^2/4}} + \frac{p_{ylim} \text{Atan}\left(\frac{p_{xlim}}{\sqrt{(p_\parallel - p_{ave})^2 + p_{ylim}^2 + \Gamma^2/4}}\right)}{\sqrt{(p_\parallel - p_{ave})^2 + p_{ylim}^2 + \Gamma^2/4}} \right] \quad (\text{E.10})$$

The influence of a incomplete acceptance is demonstrated in Figure E.1, where the parallel momentum distribution of a Lorentzian distribution ( $\Gamma=50$  MeV/c) is given for complete acceptance and for an acceptance similar to that of the medium acceptance mode of the A1200 Spectrograph at the National Superconducting Cyclotron

Table E.1: Widths of the  $p_{\parallel}$  distribution from a Lorentzian momentum density distribution ( $\Gamma=50$  MeV/c) that passes through various aperture sizes.

Aperture	Angular Acceptance (mrad)	Width (FWHM)	Transmission [ % ]
Complete	$\Delta\theta = \Delta\phi = \pm\pi$	$\Gamma$	100.
A1200	$\Delta\theta = \pm 20 \quad \Delta\phi = \pm 10$	$0.86 \Gamma$	58.2
Line	$\Delta\theta = \pm\pi \quad \Delta\phi = \pm 0.5$	$0.77\Gamma$	4.59
Pinhole	$\Delta\theta = \Delta\phi = \pm 0.5$	$0.64\Gamma$	0.313

Laboratory. The solid line is for complete acceptance, while the long dashed line shows the change in shape and transmission efficiency for the A1200 acceptance ( $\Delta\theta = 40$  mrad and  $\Delta\phi = 20$  mrad). In the center of mass (cm) frame the full width at half maximum (FWHM) with complete (A1200) acceptance is 50 MeV/c (43.1 MeV/c). While the decrease in width is only 15% there is a marked decrease in the tails of the distribution. This corresponds to the parameters for the  $p_{\parallel}$  distribution of  $^{10}\text{Be}$  fragments from  $^{11}\text{Be}$  in the case where simple assumptions lead to a distribution which appears to be close to a Lorentzian momentum distribution. For completeness the distributions observed when the acceptance is a horizontal line ( $\Delta\theta = \pm\pi$  mrad and  $\Delta\phi = \pm 0.5$  mrad) and when the acceptance is a pinhole ( $\Delta\theta = \Delta\phi = \pm 0.5$  mrad) are included, as suggested by [Rii93a]. Details are found in Table E.1.

## E.2.2 Dependence of Width on Angle

Although an incomplete acceptance can influence the observed distribution this feature can be used to characterize the nature of the momentum distribution even with low statistics experiments. For a Lorentzian density distribution, the width of the  $p_{\parallel}$  distribution depends strongly on the scattering angle when  $p_{\perp} > \Gamma$ . This effect is most easily explained for a pinhole transverse acceptance. Then the  $p_{\parallel}$  distribution

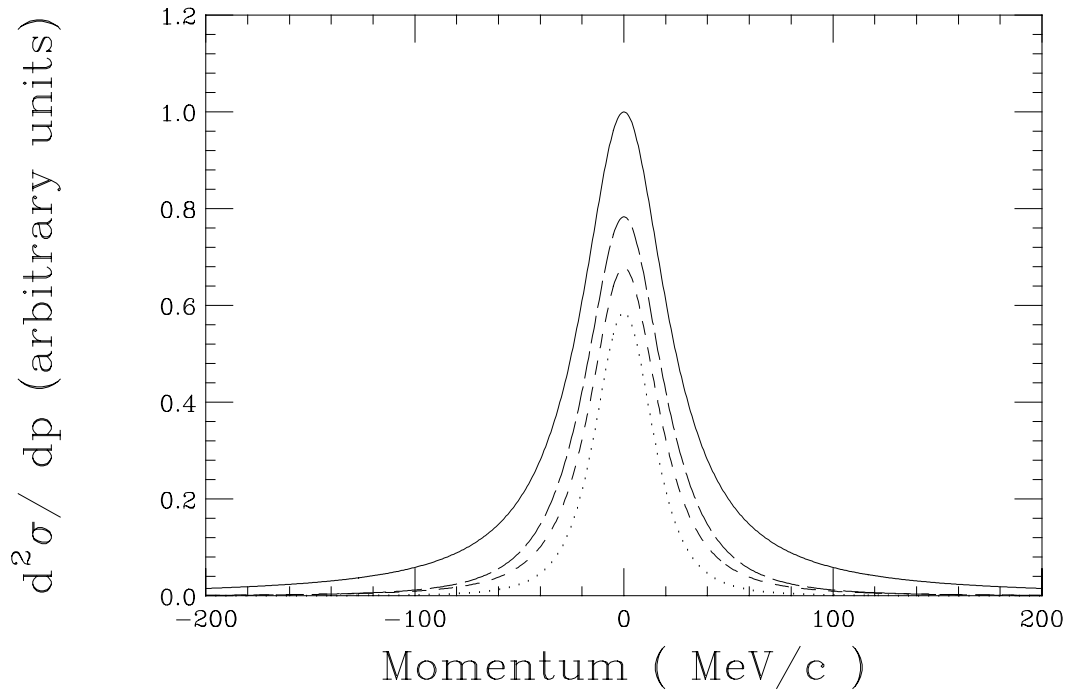


Figure E.1: The expected  $p_{||}$  distributions for a fragment with  $p_{ave}=3400$  MeV/c and with  $\Gamma=50$  MeV/c are shown for complete acceptance (solid), for an acceptance similar to that of the A1200 Spectrograph medium acceptance mode (long dashes), for a pinhole acceptance (short dashes X10), and for a horizontal line acceptance (dots X100). See Table 1 for details.

is given by evaluating  $|\Psi^*\Psi|$  at a value of  $p_{\perp}$  corresponding to the position of the pinhole.

$$P_{obs}(p_{\parallel}) = \frac{\Gamma}{2\pi^2} \frac{1}{[(p_{\parallel} - p_{ave})^2 + p_{\perp}^2 + \Gamma^2/4]^2}; \quad (\text{E.11})$$

$p_{\perp} = p_{ave} \sin(\theta_{lab})$  and  $\theta_{lab}$  is the detector angle with respect to the beam. The width  $W$  of the  $p_{\parallel}$  distribution is,

$$W = 2\gamma\sqrt{\sqrt{2} - 1}\sqrt{p_{\perp}^2 + \Gamma^2/4} FWHM. \quad (\text{E.12})$$

When the pinhole is placed at  $0^\circ$  (i.e.  $p_{\perp} = 0$  MeV/c) the width is (cm frame)  $W=0.64\Gamma$  FWHM, while for large angles the width of the parallel momentum distribution depends linearly on  $p_{\perp}$ .

Figure E.2 shows the  $p_{\parallel}$  distribution width (cm frame) expected for a small angular acceptance ( $\Delta\theta = \Delta\phi=12$  mrad). The solid line is for a Lorentzian momentum distribution with  $\Gamma = 50$ , while the dashed line is for a Gaussian momentum distribution (no acceptance dependence is expected). The data shown are from a recent experiment [She95] on the breakup of  $37\text{A}$  MeV  $^{11}\text{Li}$  in Be and U targets.

The Be target data follow the trend predicted for a Lorentzian momentum density distribution although the increase in width is somewhat smaller than predicted. This is consistent with the conclusion that the measured  $^9\text{Li}$  momentum distribution is similar to that for a Lorentzian. The distributions from breakup in the U target are in better agreement with a Gaussian momentum density distribution. This may result from effects of the Coulomb-excitation mechanism [Esb94] that dominates breakup in the U target and/or from final state interactions.

### E.2.3 Complex Momentum Distributions

The data of [She95] show that in some instances the shape of the  $p_{\parallel}$  momentum distribution is sensitive to the collection of breakup fragments. However, these data

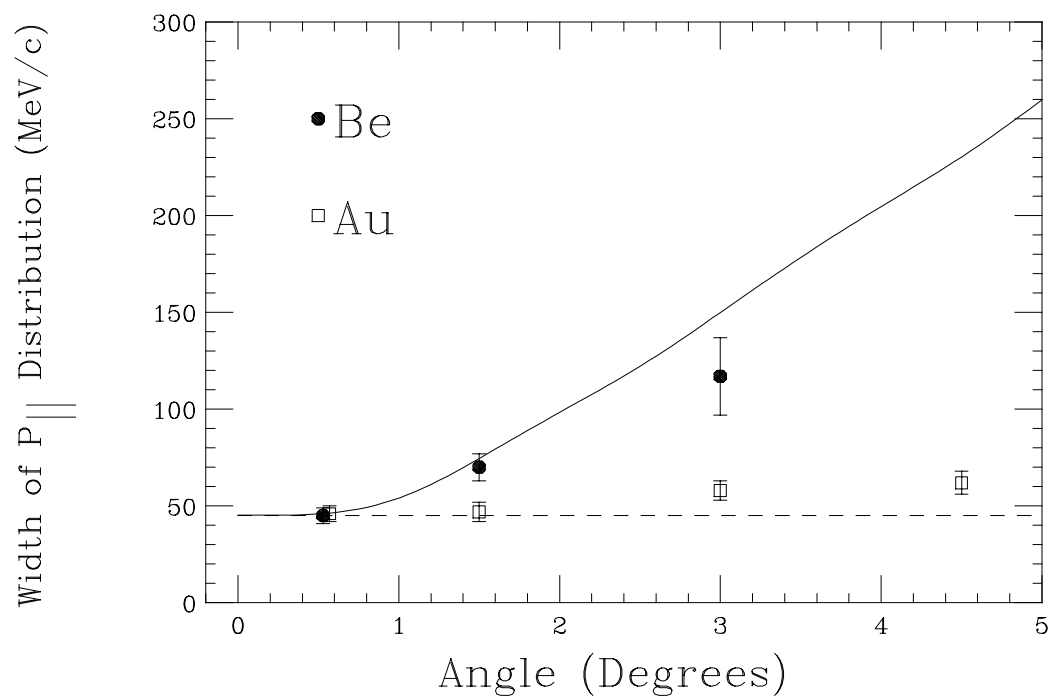


Figure E.2: The expected  $p_{||}$  distribution from a Lorentzian density distribution (solid) and a Gaussian density distribution (dashed) compared with data from the breakup of  $^{11}\text{Li}$  in the S320 [She95]. For this case  $p_{\perp} = p_{ave} \sin(\theta)$  where  $p_{ave} = 2300$  MeV/c. Details are given in the text.

also suggest that the effect is not as pronounced as expected from fragments having a Lorentzian shaped distribution. This indicates that fragments are emitted with a distribution that is more complex than either a Gaussian or a Lorentzian shape. In order to estimate the effects of incomplete acceptance on complex (non-Lorentzian, non-Gaussian) momentum distributions, a technique based on the superposition of Gaussian distributions, to fit more complex shapes is developed here. The basic assumptions are that the momentum density distribution is symmetric in three dimensional space and that the density is continuously decreasing as  $|p|$  increases. It appears that such a distribution can be well described by a linear combination of Gaussian distributions.

$$\rho(\mathbf{p}_L) \approx A \exp\left(\frac{-|\mathbf{p}_L^2|}{2\sigma_A^2}\right) + B \exp\left(\frac{-|\mathbf{p}_L^2|}{2\sigma_B^2}\right) + \dots \quad (\text{E.13})$$

If the original distribution and the linear combination of Gaussians have closely the same probabilities for all important momenta in space,  $P(p_x, p_y, p_{||})$ , then the two distributions will give essentially the same observations, regardless of the nature of the acceptance.

The influence of an incomplete acceptance on a superposition of Gaussian distributions is simple to determine. Integration of each Gaussian distribution over the acceptance limits provides the transmission coefficient,  $\epsilon$ , for each of the component Gaussian distributions. For example, for the first component above,

$$\epsilon(\sigma_A) = \int \int \frac{1}{2\pi\sigma_A^2} \exp\left[\frac{-(p_x^2 + p_y^2)}{2\sigma_A^2}\right] dp_x dp_y. \quad (\text{E.14})$$

The final step necessary to obtain the  $p_{||}$  distribution is to superimpose the Gaussian distributions taking into account the transmission efficiencies.

$$P_{obs}(p_{||}) \approx \epsilon(\sigma_A)A \exp\left(\frac{-(p_{||} - p_{ave})^2}{2\sigma_A^2}\right) + \epsilon(\sigma_B)B \exp\left(\frac{-(p_{||} - p_{ave})^2}{2\sigma_B^2}\right) + \dots \quad (\text{E.15})$$

This approach has the advantage that the dependence of the transmission coefficients on the acceptance can be represented as a single curve, see Figure E.3. Thereafter,

any theoretical result can be fitted by a series of Gaussians, the corresponding transmissions taken from the curve, and the filtered result compared to the experimental data.

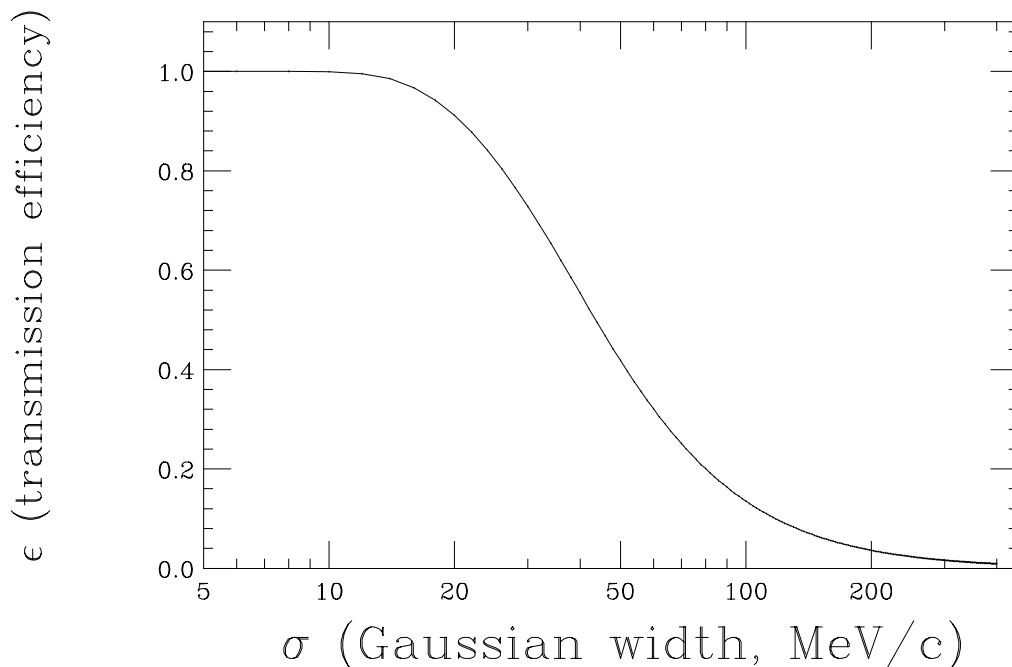


Figure E.3: The transmission of the A1200 spectrograph for a Gaussian distribution as a function of its standard deviation. The curve is calculated for  $^{10}\text{Be}$  fragments with  $p_{ave}=3400$  MeV/c produced in the A1200 medium acceptance mode, ( $\Delta\theta = \pm 20$  mrad and  $\Delta\phi = \pm 10$  mrad).

This approach has been tested for a Lorentzian distribution where the analytical results of Equation E.10 are available. In Figure E.4 are shown the results of fitting a Lorentzian distribution with three Gaussians (two Gaussians were not adequate). The resulting filtered distribution agrees well with the analytical result, except in the far wings of the distribution, and predicts the width of the observed  $p_{\parallel}$  distribution within 1%. This approach is adequate at  $0^\circ$ ; however, at detector angles other than  $0^\circ$  it appears that a significantly larger number of Gaussians are necessary in the fit.

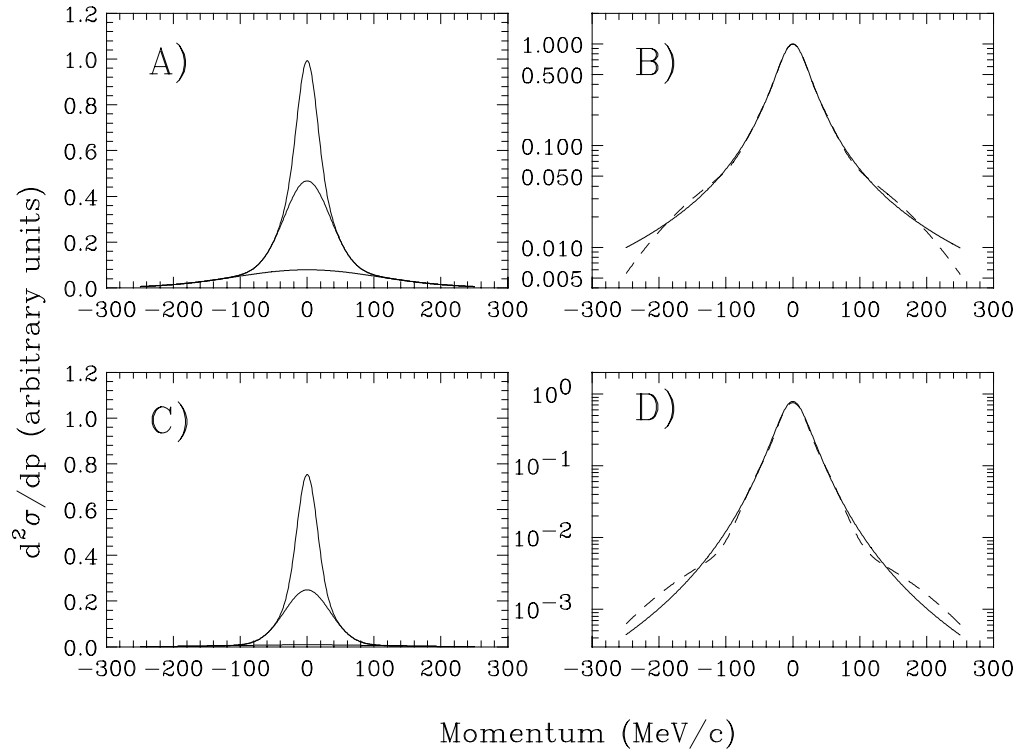


Figure E.4: The three components of the Gaussian fit to a Lorentzian are shown in A), and a comparison of the three Gaussians (dashes) with the Lorentzian (solid) is shown in B). The three Gaussian distribution, corrected for the incomplete acceptance using transmission efficiencies from figure 3, is shown in C). Note that the broad component in A) is almost eliminated after correction for the acceptance. A comparison of the analytical solution obtained from Equation E.10 (solid) and the three Gaussian estimate (dashes) is in D).

The results for a more realistic wavefunction are shown in Figure E.5. The  $p_{\parallel}$  distribution is that of a  $2s_{1/2}$  orbital bound by 500 keV in a Woods-Saxon potential [Esb94] (appropriate to describe the dominant configuration for the  $^{11}\text{Be}$  ground state). In this case the effects of the incomplete acceptance are smaller than for a Lorentzian wavefunction. The width (FWHM) of the  $p_{\parallel}$  distribution is reduced by 6% from 45.4 MeV/c to 42.5 MeV/c.

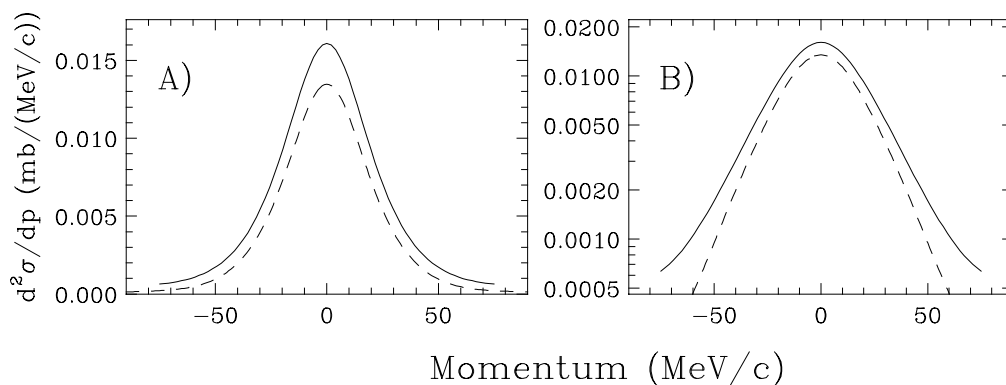


Figure E.5: The  $p_{\parallel}$  distribution for a  $1s_{1/2}$  orbital neutron bound by 500 keV in a Woods-Saxon well (solid), and the corresponding filtered  $p_{\parallel}$  distribution using the three Gaussian method to estimate the influence of the A1200 in medium acceptance mode (dashes) ( $\Delta\theta = \pm 20$  mrad and  $\Delta\phi = \pm 10$  mrad).

### E.3 Summary

An analytic result for the parallel momentum distribution expected when a Lorentzian momentum distribution is observed with a device having an incomplete angular acceptance is given. Coupling between the Cartesian components of the Lorentzian distribution causes the measured  $p_{\parallel}$  distribution to deviate significantly from that of a device that collects all breakup fragments.

The apparatus detecting the breakup fragments can influence the observed distri-

bution, since the width of the  ${}^9\text{Li}$   $p_{\parallel}$  distribution from  ${}^{11}\text{Li}$  breakup increases at large  $p_{\perp}$ . However, the increase in width is not as large as expected from a Lorentzian distribution.

Finally, an approximate method based on a superposition of Gaussian distributions is developed in order to make simple estimates of the influence of an incomplete acceptance on the  $p_{\parallel}$  distribution from a theoretical model when no straightforward analytical solution exists.



# Appendix F

## Coulomb Reacceleration on a Heavy Target

Coulomb reacceleration occurs when a breakup occurs near to a target nucleus. In this case, the potential energy that was stored in the Coulomb field of the target is divided between the breakup fragments. If the charge to mass ratio of the two fragments is significantly different, then the energy (per nucleon) is unevenly divided, and the mean energy of breakup fragments can reflect information revealing the breakup timescale. The Coulomb reacceleration of  ${}^9\text{Li}$  following the breakup of  ${}^{11}\text{Li}$  was explained by Bauer and Bertulani [Bau92] and is summarized here.

### F.1 Coulomb Reacceleration in ${}^{11}\text{Li}$ Breakup Fragments

By assuming straight line trajectories and neglecting the recoil of the target nucleus the solution of the reacceleration problem becomes simple. Relying on the conservation of momentum,

$$P_{11}(t) = P_9(t) + P_2(t) \tag{F.1}$$

and the conservation of energy,

$$E_{lab} - V[R(t)] - Q\Theta(t - t_{breakup}) = P_{11}^2(t)/(2m_{11}), \tag{F.2}$$

it is possible to determine the final energies of the breakup fragments when  $Q$ , the energy transfer to the  $^{11}\text{Li}$ , is at the breakup threshold value.  $R(t) \approx (b^2 + v_0^2 t^2)^{1/2}$ ,  $V[R(t)]$  is the potential energy stored in the Coulomb field, and  $\Theta(t - t_{breakup})$  is the step function.

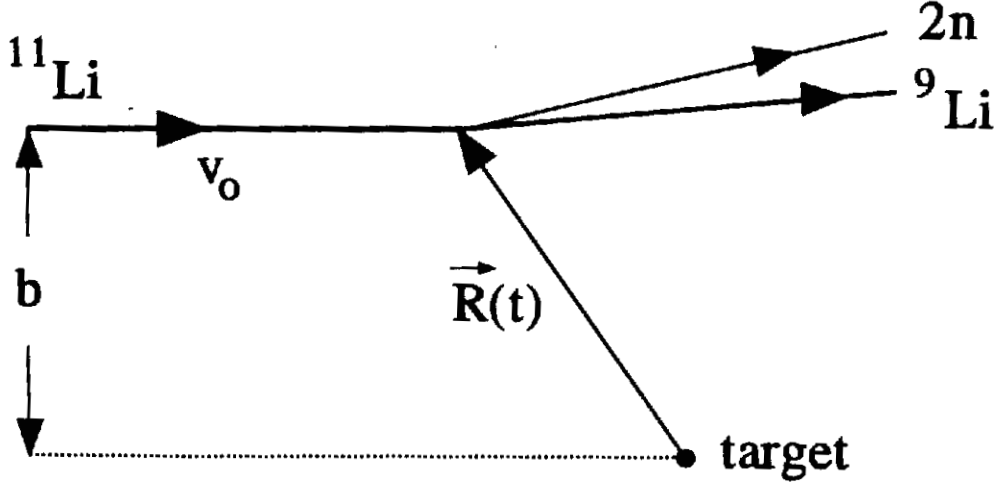


Figure F.1: [Bau92] A schematic representation of the breakup of  $^{11}\text{Li}$ .

At the instant of breakup the the  $^9\text{Li}$  core and the two neutrons continue with equal speeds. However, because the two neutrons have no nuclear charge, the  $^9\text{Li}$  core inherits all of the potential energy. As a result the  $^9\text{Li}$  energy is given by,

$$E_9 = \frac{9}{11}[E_{lab} - Q] + \frac{2}{11}V[R(t_{breakup})]. \quad (\text{F.3})$$

When The  $^9\text{Li}$  emerges far from the breakup site, the energy is shifted by,

$$\Delta E_9 = E_9 - \frac{9}{11}P_0^2/(2m_{11}) = -\frac{9}{11}Q + \frac{2}{11}V[R(t_{breakup})]. \quad (\text{F.4})$$

In a similar manner,

$$\Delta E_2 = -\frac{2}{11}Q - \frac{2}{11}V[R(t_{breakup})]. \quad (\text{F.5})$$

The term that reflects the post acceleration of the  $^9\text{Li}$  (neutrons) is the  $+(-) V[R(t_{breakup})]$  term.

## Appendix G

# Data Tables for $^{10}\text{Be}$ Fragment Momentum Distributions

Table G.1: The data for the  $^{10}\text{Be}$  fragment  $p_{\parallel}$  distribution on the Be target.

Momentum (MeV/c)	Counts	Uncertainty
3385.5	662.3	29.
3387.5	720.9	30.
3389.5	848.3	32.
3391.5	884.2	33.
3393.5	1016.4	35.
3395.5	1125.1	36.
3397.5	1181.0	37.
3399.5	1434.9	40.
3401.5	1439.5	40.
3403.5	1518.7	41.
3405.5	1580.5	42.
3407.5	1754.4	43.
3409.5	1845.9	44.
3411.5	1921.3	45.
3413.5	1905.5	45.
3415.5	1798.9	43.
3417.5	1932.9	45.
3419.5	1816.4	43.
3421.5	1795.8	43.
3423.5	1646.6	41.
3425.5	1563.6	40.
3427.5	1529.6	39.
3429.5	1333.9	36.
3431.5	1284.4	36.
3433.5	1096.6	33.
3435.5	1014.2	31.
3437.5	934.9	30.
3439.5	853.2	29.
3441.5	752.2	27.
3443.5	592.6	24.

Table G.2: The data for the  $^{10}\text{Be}$  fragment  $p_{\parallel}$  distribution on the Nb target.

Momentum (MeV/c)	Counts	Uncertainty
3383.5	251.	18.
3385.5	313.	20.
3387.5	318.	20.
3389.5	369.	21.
3391.5	426.	23.
3393.5	398.	22.
3395.5	479.	24.
3397.5	491.	24.
3399.5	549.	25.
3401.5	560.	25.
3403.5	591.	26.
3405.5	661.	27.
3407.5	629.	26.
3409.5	623.	26.
3411.5	658.	26.
3413.5	734.	28.
3415.5	790.	29.
3417.5	711.	27.
3419.5	680.	26.
3421.5	662.	26.
3423.5	650.	26.
3425.5	638.	25.
3427.5	575.	24.
3429.5	582.	24.
3431.5	497.	22.
3433.5	494.	22.
3435.5	381.	19.
3437.5	399.	20.
3439.5	357.	18.
3441.5	330.	18.
3443.5	263.	16.

Momentum	Counts	Uncertainty
3373.5	118.6	10.
3375.5	114.8	10.
3377.5	102.9	9.4
3379.5	122.7	10.
3381.5	137.4	10.
3383.5	155.0	11.
3385.5	189.5	12.
3387.5	206.3	13.
3389.5	201.5	12.
3391.5	231.7	13.
3393.5	252.8	14.
3395.5	281.7	14.
3397.5	315.3	15.
3399.5	320.7	15.
3401.5	360.2	16.
3403.5	371.7	16.
3405.5	408.8	18.
3407.5	400.0	19.
3409.5	449.7	20.
3411.5	446.3	19.
3413.5	480.4	20.
3415.5	427.1	18.
3417.5	424.8	22.
3419.5	452.1	23.
3421.5	466.2	24.
3423.5	434.7	22.
3425.5	487.9	23.
3427.5	460.0	23.
3429.5	471.1	23.
3431.5	400.9	21.
3433.5	330.4	18.
3435.5	315.6	18.
3437.5	303.5	18.

Table G.3: The data for the  $^{10}\text{Be}$  fragment  $p_{\parallel}$  distribution on the Ta target.

Momentum (MeV/c)	Counts	Uncertainty
3307.5	20.4	9.1
3309.5	27.3	10.
3311.5	40.7	12.
3313.5	31.9	10.
3315.5	13.5	6.7
3317.5	29.5	9.8
3319.5	19.0	7.7
3321.5	30.7	9.7
3323.5	26.8	8.9
3325.5	34.7	10.
3327.5	36.5	10.
3329.5	27.3	8.6
3331.5	26.7	8.4
3333.5	31.3	9.0
3335.5	43.4	10.
3337.5	35.0	9.3
3339.5	51.5	11.
3341.5	45.7	10.
3343.5	40.2	9.7
3345.5	39.6	9.6
3347.5	36.6	9.1
3349.5	38.4	9.3
3351.5	46.8	10.
3353.5	59.4	11.
3355.5	48.9	9.1
3357.5	57.9	7.8
3359.5	69.0	8.3
3361.5	58.2	7.6
3363.5	80.7	8.8
3365.5	70.6	8.1
3367.5	82.9	8.7
3369.5	76.8	8.3
3371.5	104.0	9.6

Momentum	Counts	Uncertainty
3439.5	261.8	16.
3441.5	244.9	15.
3443.5	216.9	14.
3445.5	172.3	13.
3447.5	158.7	12.
3449.5	137.7	11.
3451.5	119.5	10.
3453.5	101.2	10.
3455.5	88.1	9.1
3457.5	81.4	8.8
3459.5	77.6	8.9
3461.5	59.8	7.6
3463.5	58.3	7.6
3465.5	34.8	5.5
3467.5	30.3	5.3
3469.5	37.7	9.7
3471.5	37.5	9.6
3473.5	29.8	8.6
3475.5	12.3	5.5
3477.5	39.3	9.8
3479.5	2.4	2.4
3481.5	12.1	5.4
3483.5	19.4	6.8
3485.5	7.2	4.1
3487.5	12.0	5.4
3489.5	12.0	5.4
3491.5	14.4	5.9
3493.5	4.8	3.4
3495.5	2.4	2.4
3497.5	16.8	6.3
3499.5	14.4	5.9
3501.5	7.2	4.1
3503.5	4.8	3.4

Table G.4: The data for the  $^{10}\text{Be}$  fragment  $p_{\parallel}$  distribution on the U target.

Momentum (MeV/c)	Counts	Uncertainty
3393.5	184.4	15.
3395.5	171.6	14.
3397.5	220.4	16.
3399.5	224.7	16.
3401.5	244.0	17.
3403.5	256.8	17.
3405.5	293.2	18.
3407.5	319.0	19.
3409.5	337.6	19.
3411.5	392.0	21.
3413.5	370.5	20.
3415.5	435.0	21.
3417.5	455.4	22.
3419.5	488.6	23.
3421.5	471.0	22.
3423.5	451.8	21.
3425.5	446.0	21.
3427.5	485.5	22.
3429.5	461.4	21.
3431.5	426.3	21.
3433.5	494.8	22.
3435.5	449.3	21.
3437.5	383.1	19.
3439.5	358.2	19.
3441.5	361.0	19.
3443.5	327.7	18.
3445.5	294.8	17.
3447.5	235.0	15.
3449.5	229.7	15.
3451.5	172.4	13.

# Appendix H

## Data Tables for ${}^7\text{Be}$ Fragment Momentum Distributions

Momentum	Counts	Uncertainty
1956.5	300.	17.
1964.5	256.	16.
1972.5	207.	14.
1980.5	161.	12.
1988.5	129.	11.
1996.5	101.	10.
2004.5	82.	9.0
2012.5	66.	8.1
2020.5	61.	7.8
2028.5	37.	6.0
2036.5	43.	6.5
2044.5	31.	5.5
2052.5	41.	6.4
2060.5	23.	4.7
2068.5	20.	4.4
2076.5	15.	3.8
2084.5	12.	3.4
2092.5	7.	2.6

Table H.1: The data for the  ${}^7\text{Be}$  fragment momentum distribution on the Be target measured in Telescope 1.

Momentum (MeV/c)	Counts	Uncertainty
1700.5	9.	3.0
1708.5	9.	3.0
1716.5	8.	2.8
1724.5	10.	3.1
1732.5	16.	4.0
1740.5	6.	2.4
1748.5	13.	3.6
1756.5	13.	3.6
1764.5	16.	4.0
1772.5	13.	3.6
1780.5	20.	4.4
1788.5	27.	5.1
1796.5	33.	5.7
1804.5	30.	5.4
1812.5	37.	6.0
1820.5	28.	5.2
1828.5	49.	7.0
1836.5	58.	7.6
1844.5	64.	8.0
1852.5	94.	9.6
1860.5	100.	10.
1868.5	124.	11.
1876.5	187.	13.
1884.5	178.	13.
1892.5	261.	16.
1900.5	316.	17.
1908.5	397.	19.
1916.5	442.	21.
1924.5	397.	19.
1932.5	430.	20.
1940.5	435.	20.
1948.5	352.	18.

Momentum	Counts	Uncertainty
1860.5	30.	5.4
1868.5	26.	5.0
1876.5	27.	5.1
1884.5	40.	6.3
1892.5	44.	6.6
1900.5	46.	6.7
1908.5	45.	6.7
1916.5	33.	5.7
1924.5	44.	6.6
1932.5	46.	6.7
1940.5	33.	5.7
1948.5	38.	6.1
1956.5	26.	5.0
1964.5	18.	4.2
1972.5	20.	4.4
1980.5	21.	4.5
1988.5	24.	4.8
1996.5	16.	4.0
2004.5	11.	3.3
2012.5	6.	2.4
2020.5	10.	3.1
2028.5	5.	2.2
2036.5	7.	2.6
2044.5	4.	2.0
2052.5	6.	2.4
2060.5	4.	2.0
2068.5	1.	1.0
2076.5	0.	0.0
2084.5	0.	0.0
2092.5	1.	1.0
2100.5	1.	1.0
2108.5	0.	0.0

Table H.2: The data for the  ${}^7\text{Be}$  fragment momentum distribution on the Be target measured in Telescope 2.

Momentum (MeV/c)	Counts	Uncertainty
1604.5	3.	1.7
1612.5	5.	2.2
1620.5	4.	2.0
1628.5	3.	1.7
1636.5	4.	2.0
1644.5	3.	1.7
1652.5	5.	2.2
1660.5	4.	2.0
1668.5	7.	2.6
1676.5	3.	1.7
1684.5	13.	3.6
1692.5	10.	3.1
1700.5	8.	2.8
1708.5	7.	2.6
1716.5	10.	3.1
1724.5	10.	3.1
1732.5	9.	3.0
1740.5	11.	3.3
1748.5	10.	3.1
1756.5	12.	3.4
1764.5	11.	3.3
1772.5	14.	3.7
1780.5	15.	3.8
1788.5	13.	3.6
1796.5	13.	3.6
1804.5	13.	3.6
1812.5	22.	4.6
1820.5	18.	4.2
1828.5	16.	4.0
1836.5	18.	4.2
1844.5	26.	5.0
1852.5	23.	4.7

Table H.3: The data for the  ${}^7\text{Be}$   $p_x$  fragment momentum distribution on the Be target.

Momentum (MeV/c)	Counts	Uncertainty
-271.	19.1	3.9
-259.	17.5	3.8
-247.	12.5	3.2
-236.	17.5	3.8
-223.	22.5	4.3
-212.	30.8	5.0
-200.	34.1	5.3
-188.	36.6	5.5
-176.	41.6	5.8
-164.	57.5	6.9
-152.	50.8	6.5
-140.	69.1	7.5
-128.	74.1	7.8
-116.	90.0	8.6
-104.	104.1	9.3
-92.	110.8	9.6
-26.	573.	23.
-16.	640.	25.
-6.	674.	25.
4.	704.	26.
14.	648.	25.
24.	605.	24.
34.	498.	22.
43.	425.	20.
54.	306.	17.
64.	202.	14.
74.	182.	13.
84.	155.	12.
94.	103.	10.
104.	95.	9.7
114.	88.	9.3

Momentum	Counts	Uncertainty
1956.5	92.	9.5
1964.5	40.	6.3
1972.5	30.	5.4
1980.5	30.	5.4
1988.5	9.	3.0
1996.5	15.	3.8
2004.5	11.	3.3
2012.5	8.	2.8
2020.5	11.	3.3
2028.5	6.	2.4
2036.5	4.	2.0
2044.5	5.	2.2
2052.5	9.	3.0
2060.5	10.	3.1
2068.5	7.	2.6
2076.5	4.	2.0
2084.5	2.	1.4
2092.5	1.	1.0

Table H.4: The data for the  ${}^7\text{Be}$  fragment momentum distribution on the Nb target measured in Telescope 1.

Momentum (MeV/c)	Counts	Uncertainty
1700.5	3.	1.7
1708.5	2.	1.4
1716.5	4.	2.0
1724.5	2.	1.4
1732.5	7.	2.6
1740.5	3.	1.7
1748.5	4.	2.0
1756.5	10.	3.1
1764.5	7.	2.6
1772.5	7.	2.6
1780.5	6.	2.4
1788.5	7.	2.6
1796.5	5.	2.2
1804.5	11.	3.3
1812.5	14.	3.7
1820.5	18.	4.2
1828.5	15.	3.8
1836.5	12.	3.4
1844.5	17.	4.1
1852.5	31.	5.5
1860.5	44.	6.6
1868.5	45.	6.7
1876.5	69.	8.3
1884.5	81.	9.0
1892.5	110.	10.
1900.5	134.	11.
1908.5	164.	12.
1916.5	163.	12.
1924.5	147.	12.
1932.5	160.	12.
1940.5	149.	12.
1948.5	122.	11.

Momentum	Counts	Uncertainty
1860.5	23.	4.7
1868.5	39.	6.2
1876.5	38.	6.1
1884.5	49.	7.0
1892.5	47.	6.8
1900.5	47.	6.8
1908.5	48.	6.9
1916.5	37.	6.0
1924.5	42.	6.4
1932.5	29.	5.3
1940.5	29.	5.3
1948.5	21.	4.5
1956.5	20.	4.4
1964.5	10.	3.1
1972.5	11.	3.3
1980.5	6.	2.4
1988.5	7.	2.6
1996.5	5.	2.2
2004.5	2.	1.4
2012.5	3.	1.7
2020.5	0.	0.0
2028.5	0.	0.0
2036.5	0.	0.0
2044.5	1.	1.0
2052.5	3.	1.7
2060.5	0.	0.0
2068.5	1.	1.0
2076.5	0.	0.0
2084.5	0.	0.0
2092.5	0.	0.0
2100.5	0.	0.0
2108.5	0.	0.0

Table H.5: The data for the  ${}^7\text{Be}$  fragment momentum distribution on the Nb target measured in Telescope 2.

Momentum (MeV/c)	Counts	Uncertainty
1604.5	0.	0.0
1612.5	0.	0.0
1620.5	0.	0.0
1628.5	0.	0.0
1636.5	1.	1.0
1644.5	1.	1.0
1652.5	0.	0.0
1660.5	1.	1.0
1668.5	2.	1.4
1676.5	1.	1.0
1684.5	5.	2.2
1692.5	1.	1.0
1700.5	4.	2.0
1708.5	1.	1.0
1716.5	3.	1.7
1724.5	3.	1.7
1732.5	1.	1.0
1740.5	2.	1.4
1748.5	2.	1.4
1756.5	3.	1.7
1764.5	2.	1.4
1772.5	2.	1.4
1780.5	6.	2.4
1788.5	7.	2.6
1796.5	7.	2.6
1804.5	5.	2.2
1812.5	9.	3.0
1820.5	11.	3.3
1828.5	9.	3.0
1836.5	16.	4.0
1844.5	14.	3.7
1852.5	18.	4.2

Table H.6: The data for the  ${}^7\text{Be}$   $p_x$  fragment momentum distribution on the Nb target.

Momentum (MeV/c)	Counts	Uncertainty
-271.	5.8	2.2
-259.	4.1	1.8
-247.	9.1	2.7
-236.	11.6	3.1
-223.	15.8	3.6
-212.	12.5	3.2
-200.	23.3	4.4
-188.	22.5	4.3
-176.	24.1	4.4
-164.	37.5	5.5
-152.	42.5	5.9
-140.	43.3	6.0
-128.	62.5	7.2
-116.	68.3	7.5
-104.	70.8	7.6
-92.	78.3	8.0
-26.	165.	12.
-16.	169.	13.
-6.	179.	13.
4.	167.	12.
14.	166.	12.
24.	163.	12.
34.	138.	11.
43.	124.	11.
54.	123.	11.
64.	103.	10.
74.	99.	9.9
84.	85.	9.2
94.	81.	9.0
104.	89.	9.4
114.	55.	7.4

Momentum	Counts	Uncertainty
1956.5	50.	7.0
1964.5	25.	5.0
1972.5	14.	3.7
1980.5	4.	2.0
1988.5	8.	2.8
1996.5	7.	2.6
2004.5	3.	1.7
2012.5	3.	1.7
2020.5	4.	2.0
2028.5	8.	2.8
2036.5	5.	2.2
2044.5	5.	2.2
2052.5	7.	2.6
2060.5	7.	2.6
2068.5	3.	1.7
2076.5	2.	1.4
2084.5	1.	1.0
2092.5	2.	1.4

Table H.7: The data for the  ${}^7\text{Be}$  fragment momentum distribution on the Au target measured in Telescope 1.

Momentum (MeV/c)	Counts	Uncertainty
1700.5	3.	1.7
1708.5	2.	1.4
1716.5	0.	0.0
1724.5	4.	2.0
1732.5	2.	1.4
1740.5	3.	1.7
1748.5	3.	1.7
1756.5	1.	1.0
1764.5	4.	2.0
1772.5	4.	2.0
1780.5	5.	2.2
1788.5	4.	2.0
1796.5	12.	3.4
1804.5	5.	2.2
1812.5	5.	2.2
1820.5	12.	3.4
1828.5	10.	3.1
1836.5	5.	2.2
1844.5	9.	3.0
1852.5	9.	3.0
1860.5	8.	2.8
1868.5	18.	4.2
1876.5	28.	5.2
1884.5	41.	6.4
1892.5	78.	8.8
1900.5	101.	10.
1908.5	107.	10.
1916.5	122.	11.
1924.5	126.	11.
1932.5	110.	10.
1940.5	121.	11.
1948.5	96.	9.7

Momentum	Counts	Uncertainty
1860.5	11.	3.3
1868.5	24.	4.8
1876.5	33.	5.7
1884.5	49.	7.0
1892.5	55.	7.4
1900.5	58.	7.6
1908.5	60.	7.7
1916.5	65.	8.0
1924.5	56.	7.4
1932.5	63.	7.9
1940.5	39.	6.2
1948.5	41.	6.4
1956.5	28.	5.2
1964.5	21.	4.5
1972.5	8.	2.8
1980.5	4.	2.0
1988.5	0.	0.0
1996.5	3.	1.7
2004.5	1.	1.0
2012.5	1.	1.0
2020.5	0.	0.0
2028.5	2.	1.4
2036.5	1.	1.0
2044.5	0.	0.0
2052.5	0.	0.0
2060.5	0.	0.0
2068.5	0.	0.0
2076.5	0.	0.0
2084.5	0.	0.0
2092.5	0.	0.0

Table H.8: The data for the  ${}^7\text{Be}$  fragment momentum distribution on the Au target measured in Telescope 2.

Momentum (MeV/c)	Counts	Uncertainty
1604.5	0.	0.0
1612.5	2.	1.4
1620.5	1.	1.0
1628.5	0.	0.0
1636.5	0.	0.0
1644.5	2.	1.4
1652.5	0.	0.0
1660.5	4.	2.0
1668.5	2.	1.4
1676.5	1.	1.0
1684.5	2.	1.4
1692.5	1.	1.0
1700.5	1.	1.0
1708.5	4.	2.0
1716.5	0.	0.0
1724.5	0.	0.0
1732.5	2.	1.4
1740.5	1.	1.0
1748.5	1.	1.0
1756.5	2.	1.4
1764.5	2.	1.4
1772.5	1.	1.0
1780.5	3.	1.7
1788.5	3.	1.7
1796.5	4.	2.0
1804.5	4.	2.0
1812.5	6.	2.4
1820.5	5.	2.2
1828.5	7.	2.6
1836.5	4.	2.0
1844.5	10.	3.1
1852.5	18.	4.2

Table H.9: The data for the  ${}^7\text{Be}$   $p_x$  fragment momentum distribution on the Au target.

Momentum (MeV/c)	Counts	Uncertainty
-271.	19.1	3.9
-259.	15.8	3.6
-247.	15.8	3.6
-236.	19.1	3.9
-223.	19.1	3.9
-212.	17.5	3.8
-200.	39.1	5.7
-188.	32.5	5.2
-176.	28.3	4.8
-164.	50.0	6.4
-152.	46.6	6.2
-140.	46.6	6.2
-128.	64.1	7.3
-116.	50.8	6.5
-104.	61.6	7.1
-92.	55.0	6.7
-26.	141.	11.
-16.	99.	9.9
-6.	101.	10.
4.	101.	10.
14.	87.	9.3
24.	93.	9.6
34.	103.	10.
43.	69.	8.3
54.	75.	8.6
64.	64.	8.0
74.	74.	8.6
84.	77.	8.7
94.	49.	7.0
104.	67.	8.1
114.	50.	7.0

# Bibliography

- [Ann90] R. Anne, S.E. Arnell, R. Bimbot, H. Emling, D. Guillemaud-Mueller, P.G. Hansen, L. Johannsen, B. Jonson, M. Lewitowicz, S. Mattsson, A.C. Mueller, R. Neugart, G. Nyman, F. Pougheon, A. Richter, K. Riisager, M.G. Saint-Laurent, G. Schrieder, O. Sorlin, and K. Wilhelmsen, *Phys. Lett. B* **250**, 19 (1990).
- [Ann93] R. Anne, S.E. Arnell, R. Bimbot, S. Dogny, H. Emling, H. Esbensen, D. Guillemaud-Mueller, P.G. Hansen, P. Hornshøj, F. Humbert, B. Jonson, M. Keim, M. Lewitowicz, P. Møller, A.C. Mueller, R. Neugart, T. Nilsson, G. Nyman, F. Pougheon, K. Riisager, M.G. Saint-Laurent, G. Schrieder, O. Sorlin, O. Tengblad, K. Wilhelmsen Rolander and D. Wolski, *Phys. Lett. B* **304**, 55 (1993).
- [Ann94] R. Anne, R. Bimbot, S. Dogny, H. Emling, D. Guillemaud-Mueller, P.G. Hansen, P. Hornshøj, F. Humbert, B. Jonson, M. Keim, M. Lewitowicz, P. Møller, A.C. Mueller, R. Neugart, T. Nilsson, G. Nyman, F. Pougheon, K. Riisager, M.G. Saint-Laurent, G. Schrieder, O. Sorlin, O. Tengblad, and K. Wilhelmsen Rolander, *Nucl. Phys. A* **575**, 125 (1994).
- [Ajz90] F. Ajzenberg-Selove, *Nucl. Phys. A* **506**, 1 (1990).
- [Ban93] P. Banerjee and R. Shyam, *Phys. Lett. B* **318**, 268 (1993).
- [Bar93] F. Barranco, E. Vigezzi and R.A. Broglia, *Phys. Lett. B* **319**, 387 (1993).
- [Bar95] F. Barranco, E. Vigezzi and R.A. Broglia, Univ. of Milano preprint no. NTGMI-95-2.
- [Bau92] G. Baur, C.A. Bertulani and D.M. Kalassa, *Nucl. Phys. A* **550**, 527 (1992).
- [Ber88] C.A. Bertulani and G. Baur, *Phys. Rep.* **163**, 299 (1988).
- [Ber92] C.A. Bertulani and K.W. McVoy, *Phys. Rev. C* **46**, 2638 (1992).
- [Bla91] B. Blank, J.-J. Gaimard, H. Geissel, K.-H. Schmidt, H. Selzer, K. Sümmerer, D. Bazin, R. Del Moral, J.P. Dufour, A. Fleury, F. Humbert, H.-G. Clerc and M. Steiner, *Z. Phys. A* **340**, 41 (1991).

- [Bro95a] B.A. Brown private communication.
- [Bro95b] B.A. Brown, A. Csótó, and R. Sher, submitted to Nucl. Phys. A.
- [Cso93] A. Csótó, Phys. Lett. B **315**, 24 (1993).
- [Esb91] H. Esbensen, Phys. Rev. C **44**, 440 (1991).
- [Esb92] H. Esbensen and G.F. Bertsch, Nucl. Phys. A **542**, 310 (1992).
- [Esb94] H. Esbensen, private communication (1994).
- [Esb95] H. Esbensen, private communication (1995).
- [Fri83] W.A. Friedman, Phys. Rev. C **27**, 569 (1983).
- [Fuk91] M. Fukuda, T. Ichihara, N. Inabe, T. Kubo, H. Kumagai, T. Nakagawa, Y. Yano, I. Tanihata, M. Adachi, K. Asahi, M. Kouguchi, M. Ishihara, H. Sagawa and S. Shimoura, Phys. Lett. **268B**, 339 (1991).
- [Gla90] R. Glasow, D. Grzonka, R. Santo, H.G. Bohlen, W. von Oertzen, W. Weller, Y. Blumenfeld, J.C. Jacmart, N. Frascaria, J.C. Roynette and J.P. Garron, J. Phys. G **16**, 1089 (1990).
- [Gla55] R.J. Glauber, Phys. Rev. **99**, 1515 (1955).
- [Gol74] A.S. Goldhaber, Phys. Lett. **53B**, 306 (1974).
- [Han87] P.G. Hansen and B. Jonson, Europhys. Lett., **4**, 409 (1987).
- [Han93] P.G. Hansen, Nucl. Phys. **A553**, 89c (1993).
- [Han95] P.G. Hansen, to be published in the *Proceedings of the International Conference on Exotic Nuclei and Atomic Masses*, Arles, France (1995).
- [Iek93] K. Ieki, D. Sackett, A. Galonsky, C.A. Bertulani, J.J. Kruse, W.G. Lynch, D.J. Morrissey, N.A. Orr, H. Schultz, B.M. Sherrill, A. Sustich, J.A. Winger, F. Deák, Á. Horváth, Á. Kiss, Z. Seres, J.J. Kolata, R.E. Warner, and D.L. Humphrey, Phys. Rev. Lett. **70**, 730 (1993).
- [Jac75] J.D. Jackson, *Classical Electrodynamics* (John Wiley & Sons, New York, 1975), p. 719.
- [Kar75] Paul J. Karol, Phys. Rev. C **4**, 1203 (1975).
- [Kid88] J.M. Kidd, P.J. Lindstrom, H.J. Crawford, G. Woods, Phys. Rev. C **37**, 2613 (1988).
- [Kob88] T. Kobayashi, O. Yamakawa, K. Omata, K. Sugimoto, T. Shimoda, N. Takahashi and I. Tanihata, Phys. Rev. Lett. **60**, 2599 (1988).
- [Kob89] T. Kobayashi, *Proceedings of the 1<sup>st</sup> International Conference on Radioactive Nuclear Beams*, Berkely, California, Edited by W.D. Myers, J.M. Nitschke and E.B. Norman (World Scientific, Singapore, 1989), p. 524.

- [Kob92] T. Kobayashi, Nucl. Phys. **A538**, 343c (1992).
- [Kry93] R.A. Kryger, A. Azhari, A. Galonsky, J.H. Kelley, R. Pfaff, E. Ramakrishnan, D. Sackett, B.M. Sherrill, M. Thoennessen, J.A. Winger, and S. Yokoyama, Phys. Rev. C **47**, 2439 (1993).
- [Lan94] K. Langanke and T.D. Shoppa, Phys. Rev. C **49**, 1771 (1994).
- [Mat94] Integration from mathematica.
- [Mil83] D.J. Millener, J.W. Olness, E.K. Warburton, and S.S. Hanna, Phys. Rev. C **28**, 497 (1983).
- [Min92] T. Minamisono, T. Ohtsubo, I. Minami, S. Fukuda, A. Kitagawa, M. Fukuda, K. Matsuta, Y. Nojiri, S. Takeda, H. Sagawa and H. Kitagawa, Phys. Rev. Lett. **69**, 2058 (1992).
- [Mot94] T. Motobayashi, N. Iwasa, Y. Ando, M. Kurokawa, H. Murakami, J. Ruan (Gen), S. Shimoura, S. Shirato, N. Inabe, M. Ishihara, T. Kubo, Y. Watanabe, M. Gai, R.H. France III, K.I. Hahn, Z. Zhao, T. Nakamura, T. Teranashi, Y. Futami, K. Furutaka, and Th. Delbar, Phys. Rev. Lett. **73**, 2680 (1994).
- [Nak94] T. Nakamura, S. Shimoura, T. Kobayashi, T. Teranishi, K. Abe, N. Aoi, Y. Doki, M. Fujimaki, N. Ianabe, N. Iwasa, K. Katori, T. Kubo, H. Okuno, T. Suzuki, I. Tanihata, Y. Watanabe, A. Yoshida and M. Ishihara, Phys. Lett. B **331**, 296 (1994).
- [Orr92] N.A. Orr, N. Anantaraman, Sam M. Austin, C.A. Bertulani, K. Hanold, J.H. Kelley, D.J. Morrissey, B.M. Sherrill, G.A. Souliotis, M. Thoennessen, J.S. Winfield, and J.A. Winger, Phys. Rev. Lett. **69**, 2050 (1992).
- [Orr95] N.A. Orr, N. Anantaraman, Sam M. Austin, C.A. Bertulani, K. Hanold, J.H. Kelley, R.A. Kryger, D.J. Morrissey, B.M. Sherrill, G.A. Souliotis, M. Steiner, M. Thoennessen, J.S. Winfield, J.A. Winger, and B.M. Young, Phys. Rev. C **51**, 3116 (1995).
- [Pec95] I. Pecina, R. Anne, D. Bazin, C. Borcea, V. Borrel, F. Carstoiu, J.M. Corre, Z. Dlouhy, A. Fomitchev, D. Guillemaud-Mueller, H. Keller, A. Kordyasz, M. Lewitowicz, S. Lukyanov, A.C. Mueller, Yu. Penionzhkevich, P. Roussel-Chomaz, M.G. Saint-Laurent, N. Skobelev, O. Sorlin and O. Tarasov, Phys. Rev. C **52**, 191 (1995).
- [Rii92] K. Riisager, A.S. Jensen and P. Møller, Nucl. Phys. **A548**, 393 (1992).
- [Rii93a] K. Riisager, *Proceedings of the 3<sup>rd</sup> International Conference on Radioactive Nuclear Beams*, East Lansing, Michigan, Edited by D.J. Morrissey (Editions Frontieres, Gif-sur-Yvette Cedex France, 1993), p. 281. and private communication.
- [Rii93b] K. Riisager and A.S. Jensen, Phys. Lett. B **301**, 6 (1993).

- [Sac93] D. Sackett, K. Ieki, A. Galonsky, C.A. Bertulani, H. Esbensen, J.J. Kruse, W.G. Lynch, D.J. Morrissey, N.A. Orr, B.M. Sherrill, H. Schultz A. Sustich, J.A. Winger, F. Deák, Á. Horváth, Á. Kiss, Z. Seres, J.J. Kolata, R.E. Warner, and D.L. Humphrey, *Phys. Rev. C* **48**, 118 (1993).
- [Sag93] H. Sagawa, B.A. Brown and H. Esbensen, *Phys. Lett.* **B309**, 1 (1993).
- [Sag94] H. Sagawa and N. Takigawa, *Phys. Rev. C* **50**, 985 (1994).
- [Sch95] W. Schwab, H. Geissel, H. Lenske, K.-H. Behr, A. Brünle, K. Burkard, H. Irnich, T. Kobayashi, G. Kraus, A. Magel, G. Münzenberg, F. Nickel, K. Riisager, C. Scheidenberger, B.M. Sherrill, T. Suzuki, and B. Voss, *Z. Phys.* **A 350**, 283 (1995).
- [Ser47] R. Serber, *Phys. Rev.* **72**, 1008 (1947).
- [She92] B.M. Sherrill, D.J. Morrissey, J.A. Nolen Jr., N.A. Orr and J.A. Winger, *Nucl. Instrum. Meth.* **B70**, 298 (1992).
- [She94] B.M. Sherrill, privat comunication (1994).
- [She95] B.M. Sherrill, *Nucl. Phys. A* **583**, 725 (1995).
- [Sil88] J.D. Silk, H.D. Holmgren, D.L. Hendrie, T.J.M. Symons, G.D. Westfall, P.H. Stelson, S. Raman, R.L. Auble, J.R. Wu and K. Van Bibber, *Phys. Rev. C* **37**, 158 (1988).
- [Sou92] G.A. Soliotis, D.J. Morrissey, N.A. Orr, B.M. Sherrill, and J.A. Winger, *Phys. Rev. C* **46**, 1383 (1992).
- [Tan85a] I. Tanihata, H. Hamagaki, O. Hashimoto, S. Nagamiya, Y. Shida, N. Yoshikawa, O. Yamakawa, K. Sugimoto, T. Kobayashi, D.E. Greiner, N. Takahashi, and Y. Nojiri, *Phys. Lett.* **160B**, 380 (1985).
- [Tan85b] I. Tanihata, H. Hamagaki, O. Hashimoto, Y. Shida, N. Yoshikawa, K. Sugimoto, O. Yamakawa, T. Kobayashi, and N. Takahashi, *Phys. Rev. Lett.* **55**, 2676 (1985).
- [Tan88] I. Tanihata, T. Kobayashi, O. Yamakawa, S. Shimoroura, K. Ekuni, K. Sugimoto, N. Takahashi, T. Shimoda, and H. Sato, *Phys. Lett. B* **206**, 592 (1988).
- [Thi75] C. Thibault, R. Klapisch, C. Rigaud, A.M. Poskanzer, R. Prieels, L. Lessard, and W. Reisdorf, *Phys. Rev. C* **12**, 644 (1975).
- [Uts85] Utsunomiya, *Phys. Rev. C* **32**, 849 (1985).
- [Van79] K. Van Bibber, D.L. Hendrie, D.K. Scott, H.H. Weiman, L.S. Schroeder, J.V. Geaga, S.A. Cessin, R. Treuhaft, Y.J. Grossiord and J.O. Rasmussen, *Phys. Rev. Lett.* **43**, 840 (1979).

- [War95] R. E. Warner, J.H. Kelley, P. Zecher, F.D. Becchetti, J.A. Brown, C.L. Carpenter, A. Galonsky, J.J. Kruse, A. Muthukrishnan, A. Nadasen, R.M. Ronningen, P. Schwandt, B.M. Sherrill, J. Wang and J.S. Winfield, to be published in Phys. Rev. C, September (1995).
- [Win79] A. Winther and K. Alder, Nucl. Phys **A319**, 518 (1979).
- [You93] B.M. Young, W. Benenson, M. Fauerbach, J.H. Kelley, R. Pfaff, B.M. Sherrill, M. Steiner, J.S. Winfield, T. Kubo, M. Hellström, N.A. Orr, J. Stetson, J.A. Winger, and S.J. Yennello, Phys. Rev. Lett. **71**, 4124 (1993).
- [You94] B.M. Young, W. Benenson, J.H. Kelley, N.A. Orr, R. Pfaff, B.M. Sherrill, M. Steiner, M. Thoennessen, J.S. Winfield, J.A. Winger, S.J. Yennello, and A. Zeller, Phys. Rev. C **49**, 279 (1994).